Title
Development of High Spatiotemporal Resolution Imaging of Hyperpolarized C-13 Compounds using the Balanced Steady-State Free Precession Sequence

Author
Milshteyn, Eugene

Publication Date
2017

Peer reviewed|Thesis/dissertation

Development of High Spatiotemporal Resolution Imaging of Hyperpolarized C-13 Compounds using the Balanced Steady-State Free Precession Sequence

by

Eugene Milshteyn

DISSERTATION

Submitted in partial satisfaction of the requirements for the degree of

DOCTOR OF PHILOSOPHY

in

Bioengineering

in the

GRADUATE DIVISION

of the

UNIVERSITY OF CALIFORNIA, SAN FRANCISCO

AND

[redacted]

Dedicated to my parents,

Mark and Mila Milshteyn

Acknowledgements

First and foremost, I would like to express my gratitude to Dr. Dan Vigneron for providing me with the opportunity to join his lab for my graduate studies. I have learned so much from him about conducting scientific research and cultivating a collaborative lab atmosphere. His mentorship, support, enthusiasm, and encouragement have pushed me to become the scientist I am now. I am forever grateful for all his help and guidance throughout my graduate studies.

I would like to thank Dr. John Kurhanewicz for providing all his knowledge and support. As my graduate advisor and chair of my qualifying exam committee, Dr. Kurhanewicz was always able to keep me on track with regards to my research goals and class requirements. He was also always available to talk in depth about my projects and provide insight and new ideas, and helped make me a better researcher.

I would like to first thank Dr. Peder Larson for teaching me so much about MRI, both as part of his class and as part of my qualifying committee. I also want to acknowledge how much he has helped me with all aspects of my projects, including EPIC programming, data acquisition and analysis, and inspiring new ideas.

I would like to extend my appreciation to Drs. Jane Wang and Miki Lustig for also being on my qualifying committee and offering great advice on several aspects of my proposal that have immeasurably improved all my projects.

I would not have been successful in my experiments without the immense hardware support from engineers Lucas Carvajal and Mark van Criekinge. I am also grateful to Dr. Bob Bok's help with teaching me and aiding me in the animal handling aspects of my experiments. I would also like to thank Romelyn Delos Santos for teaching and assisting me with sample preparations.

Jenny Che, Ana Marie Deluca, Mary McPolin, Kim Okamoto, and Kim Semien were always kind enough to help with any administrative and scanner matters I ran into and for that I am grateful. I would also like to express my gratitude to SarahJane Taylor and Kristin Olson for all their help with navigating the administrative matters of the Bioengineering program.

All the current and past Surbeck Lab and BioE members - Dr. Michael Ohliger, Dr. Ilwoo Park, Dr. Peng Cao, Shuyu Tang, Andrew Leynes, Dave Korenchan, Dr. Renuka Sriram, and many others - have provided numerous thoughtful discussions that have aided me immensely in my projects and I am grateful.

Adam Elkhaled has been a great friend from the moment I joined the program. From working out at the gym, to watching movies and sports, to studying for classes, Adam made graduate school very entertaining.

Cornelius von Morze, Galen Reed, Jeremy Gordon, and Hong Shang were instrumental in the success of all my projects. Numerous times, they helped me run my

experiments, deal with EPIC programming, analyze and understand my data, and helped me come up with new ideas. More importantly, they were also great, supportive friends, and were always fun to hang out with.

All of the current - Zihan Zhu, Peter Shin, Hsin-Yu Chen, Brian Chung, Daniele Mammoli - and past - Christine Swisher, Irene Marco-Rius, Yesu Feng, Rie Hansen - members have been unbelievably helpful in all my studies and have been great collaborators and I am thankful to have you as friends and colleagues.

I would like to thank Megan Thompson for all her love and support throughout my studies. Witnessing her tireless work ethic always inspired me to work harder. Her words of encouragement after unsuccessful experiments, as well as her infectious excitement for my successes, helped me immensely throughout this long journey.

Finally, I could not have gotten through this journey without the unconditional love and support of my parents, Mark and Mila. From the good times to the tough times, I knew I could always ask them for advice, and their constant interest in my work and belief in me as a scientist always pushed me to be the best I could be. They have always sacrificed so much for me and I will be forever grateful.

Development of High Spatiotemporal Resolution Imaging of Hyperpolarized C-13 Compounds using the Balanced Steady-State Free Precession Sequence

by

Eugene Milshteyn

Abstract

Hyperpolarized ^{13}C magnetic resonance imaging has become a powerful tool for investigating metabolism and perfusion in vivo for a variety of diseases, such as cancer and diabetes. Recent phase II human studies in prostate, brain, and liver cancer have shown the ability to probe pyruvate metabolism in a rapid, noninvasive, and safe fashion. However, with the short lifetime of the hyperpolarized ^{13}C magnetization, rapid sequences need to be developed to efficiently use all the magnetization. The goal of my work presented here was to develop the balanced steady-state free precession (bSSFP) sequence for high spatiotemporal resolution imaging of both metabolically active compounds, such as pyruvate and lactate, and perfusion compounds, such as urea. Initial *in vivo* studies showed the capability of both 1 mm^2 in-plane T_2 mapping and 1.5 mm 3D isotropic imaging of multiple probes, including [1-^{13}C]pyruvate, [2-^{13}C]pyruvate, [1-^{13}C]lactate, and [^{13}C,$^{15}N_2$]urea. Differences in T_2 values as well as biodistribution and uptake of each compound were detected within healthy rat kidneys, liver, and heart, as well as tumors within tumor-bearing mice. To improve dynamic imaging at these high spatial resolutions, a local low rank plus sparse (LLR+S)

reconstruction was employed, which allowed for 3D dynamic imaging at 1.5 mm isotropic resolution, as well as sub-millimeter and 3D 1 mm isotropic T_2 mapping, with each image acquired in <1 s. The LLR+S reconstruction enforced both low rank and sparse constraints via iterative soft thresholding on singular values and sparse coefficients to reconstruct undersampled dynamic MRI. Additionally, the bSSFP approach was further developed for simultaneous acquisition of multiple hyperpolarized probes, such as [1-^{13}C]pyruvate and produced [1-^{13}C]lactate, as well as [2-^{13}C]pyruvate, [1-^{13}C]lactate, and [^{13}C,$^{15}N_2$]urea. This metabolite-specific imaging was accomplished via an optimization of the RF pulse design, width, and time-bandwidth, as well as repetition time, and incorporation of spectral suppression pulses for the case of [1-^{13}C]pyruvate/[1-^{13}C]lactate imaging. The techniques developed were designed to have significant biomedical and clinical benefits, and can potentially provide high spatiotemporal assessment of multiple anatomical structures and disease progression.

Table of Contents

List of Tables

List of Figures

Chapter 1: Introduction

The development of magnetic resonance imaging (MRI) over the last forty years has provided a powerful avenue for noninvasive imaging of anatomical structure and function. The wide array of information that can currently be obtained in routine clinical imaging, including high resolution functional brain imaging, angiography, spectroscopic imaging, as well as high resolution structural imaging of nearly every part of the anatomy, has allowed MRI to be efficiently applied to disease detection and intervention. Applications to oncology, neurology, orthopedics, among other branches of medicine, combined with its safety and flexibility, have made MRI a staple for medical diagnosis, treatment selection and therapy monitoring.

While conventional MRI is done using ^{1}H as the signal source, the development of dissolution dynamic nuclear polarization has brought hyperpolarized (HP) ^{13}C to the forefront of MRI development, and allowed real-time probing of several biochemical pathways, as well as perfusion imaging, in the absence of a background signal. Recent translation into humans via phase I and phase II first-in-man studies have indicated the potential for HP ^{13}C MRI to be a clinically valuable molecular imaging approach reporting on disease progression, with successful applications to prostate, liver, and brain cancer.

A major challenge in HP ^{13}C MRI is dealing with the nonrenewable polarization that decays according to the compound T_1, and is further decreased by both RF pulses and metabolism. This limited lifetime of the hyperpolarization is on the order of 1-2 minutes, indicating a need for fast imaging sequences that efficiently utilize the polarization. Furthermore, there exists an inherent tradeoff between spatial, temporal,

and spectral resolution that needs to be considered when designing specific acquisition strategies for HP ^{13}C MRI.

The work presented in this dissertation focuses on developing and adapting the balanced steady-state free precession sequence for high spatiotemporal resolution acquisitions of both metabolically active and perfusion probes via a combination of pulse sequence optimization, imaging acceleration, and reconstruction methods. Chapters 3-5 are the main bioengineering contributions, and are adaptations of either my published work, or manuscripts I am preparing for publication. Chapter 6 is from an abstract submitted to the Proceedings of the International Society for Magnetic Resonance in Medicine.

Chapter 3 focuses on the development of a specialized bSSFP sequence for high resolution *in vivo* T_2 mapping and single time-point 3D imaging of multiple HP compounds, along with the application of compressed sensing for high spatiotemporal dynamic imaging. Calculated T_2 maps of [1-^{13}C]pyruvate, [1-^{13}C]lactate, [2-^{13}C]pyruvate, and [^{13}C,$^{15}N_2$]urea in healthy rat kidneys and tumor-bearing mice enabled parameter optimization of the sequence for 1.5 - 2 mm 3D isotropic imaging which allowed the visualization of the renal pelvis, medulla, and cortex, along with heart and vasculature, and tumor.

Chapter 4 details my research developing and applying a local low rank plus sparse reconstruction algorithm for accelerated dynamic 2D and 3D bSSFP imaging. *In vivo* sub-millimeter 2D T_2 mapping and 1-2 mm 3D isotropic imaging was achieved with high temporal resolution.

The research in Chapter 5 focused on adapting the bSSFP sequence to high spatiotemporal resolution imaging of [1-^{13}C]pyruvate and produced [1-^{13}C]lactate at 3T. Spectral suppression of [1-^{13}C]alanine and [1-^{13}C]pyruvate-hydrate prior to imaging reduced the problem to a two-peak system, which allowed ~15 ms TR to be achieved. Dynamic metabolite specific images were acquired in healthy rats and tumor-bearing mice, along with a demonstration of quantification via k_{PL} and AUC ratio maps.

Chapter 6 details the development of metabolite-specific bSSFP imaging geared towards simultaneous acquisition of [2-^{13}C]pyruvate, [1-^{13}C]lactate, [^{13}C,$^{15}N_2$]urea. Using the wide spectral separation between these three resonances, high spatiotemporal imaging of all three compounds was performed through an optimized combination of RF pulse width and TR.

Chapter 7 summarizes my contributions to hyperpolarized ^{13}C MRI research and discusses future directions with the bSSFP sequence in both preclinical imaging and translation to human imaging.

Chapter 2: Background

2.1 Fundamentals of MRI

2.1.1 Nuclear Spin, Magnetic Moment, and Polarization

Nuclear spin is an intrinsic property that describes atomic nuclei with an odd number of protons and/or an odd number of neutrons and helps form the basis of NMR/MRI measurements. Common nuclei that fit this description and are NMR/MRI relevant include ^{1}H, ^{13}C, ^{31}P, ^{19}F, and ^{23}Na. The associated magnetic dipole moment of the nuclei, μ, depends on the spin angular momentum, S, and the gyromagnetic ratio, γ, in the following manner:

$$\mu = \gamma S \quad (2.1)$$

The bulk magnetization vector, $\vec{M}$, which describes the spins of interest on a macroscopic level, can represent the resulting sum of the individual magnetic moments.

At thermal equilibrium and in the absence of an external magnetic field ($\vec{B}_0$), the spins orient in random directions, thereby canceling each other and resulting in zero net magnetization, as is seen in Figure 2.1A. However, in the presence of an external magnetic field, the spins will align themselves along the applied field (conventionally named the z- or longitudinal axis), either in parallel or anti-parallel due to thermal energy. Since the resulting energy states are not equal, a net difference between the populations of parallel and anti-parallel spins arises, resulting in $\vec{M}$ as a nonzero magnetization vector, as is seen in Figure 2.1B.

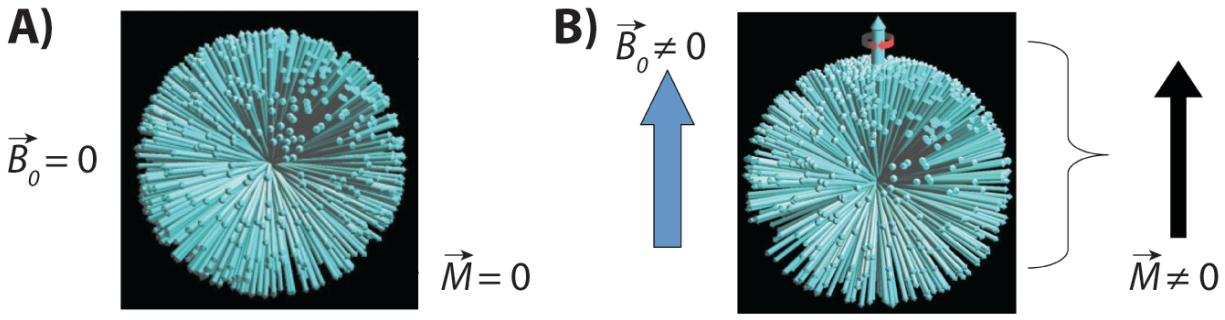

Figure 2.1: *(A) The absence of a magnetic field causes the set of spins to orient in random directions, resulting in zero net magnetization due to the spins canceling each other out. (B) However, in the presence of a magnetic field, the spins align themselves in the direction of the magnetic field, both in a parallel and anti-parallel fashion. Due to different resulting energy states, there will be a net difference between these two spin populations that results in an overall nonzero magnetization vector.*

The ratio of these two spin populations is governed by the Boltzmann distribution

$$\frac{N_-}{N_+} = e^{-\Delta E/kT} \quad (2.2)$$

where N_- and N_+ are the anti-parallel and parallel spin populations, respectively, k is the Boltzmann constant, T is the temperature in Kelvin, and ΔE is the energy difference between the spin populations,

$$\Delta E = \gamma \hbar B_0 \quad (2.3)$$

with ħ as Planck's constant and B_0 the external magnetic field. The polarization, P, is the defined as

$$P = \frac{N_+ - N_-}{N_+ + N_-} = \frac{e^{-\Delta E/kT} - 1}{e^{-\Delta E/kT} + 1} \quad (2.4)$$

and relates the fraction of spins that are aligned with $\vec{B}_0$. Given typical thermal conditions, such as 310 K and 3 Tesla, the polarization of ^{1}H is equal to 9.88×10^{-6}, meaning that only a few of the spins are parallel vs. anti-parallel for every million spins. Yet due to the high natural abundance of ^{1}H as well as the high concentration of water in the body, the signal-to-noise ratio is sufficient for conventional MRI. From an MRI

perspective, ^{1}H is the most commonly used nuclei due to its abundance in biologically relevant tissue. ^{13}C, on the other hand, has 4-fold lower polarization due to the 4-fold lower γ, and unlike ^{1}H has very low natural abundance and low concentration *in vivo*, making it an unsuitable nucleus for conventional MRI. However, with the development of dissolution dynamic nuclear polarization (discussed further in section 2.3.2), carbon-13 polarizations of 0.4 (40%) can be routinely achieved enabling high SNR, rapid ^{13}C MR imaging.

2.1.2 Bloch Equation, RF pulses, Excitation, and Relaxation

The Bloch equation is a fundamental equation in NMR/MRI describing the movement of the bulk magnetization vector $\vec{M}$ inside the external field, $\vec{B}_0$:

$$\frac{d\vec{M}}{dt} = \vec{M} \times \gamma \vec{B}_0 \quad (2.5)$$

The solution to equation 2.5 is that $\vec{M}$ precesses about $\vec{B}_0$ at an angular frequency, ω, described by:

$$\omega = \gamma \vec{B}_0 \quad (2.6)$$

where ω is commonly known as the Larmor frequency. A list of the five previously mentioned NMR/MRI active nuclei and their corresponding γ and ω values is provided in Table 2.1 for acquisition at a field strength of 3 Tesla.

Nuclei	γ (MHz/Tesla)	ω (MHz at 3 Tesla)
^{1}H	42.58	127.7
^{13}C	10.71	32.13
^{31}P	17.24	51.72
^{19}F	40.05	120.2
^{23}Na	11.26	33.78

Table 2.1: *Gyromagnetic ratio, γ, and Larmor frequency, ω for commonly used MR nuclei.*

In order to detect NMR signals, the magnetization needs to be tipped away from the z-axis into the x-y (transverse) plane. This is accomplished using radiofrequency (RF) pulses, which generate an oscillating magnetic field, $\vec{B}_1$, perpendicular to the z-axis, as is illustrated in Figure 2.2A. From a hardware perspective, transmit coils are required for transmission of the RF pulses, with the coils being tuned to the Larmor frequency of the nuclei of interest, allowing the resonance condition to be fulfilled. In that case the spins of interest absorb energy and are excited, causing them to be tipped away from their equilibrium position along the z-axis, and begin precession around the axis of the main magnetic field, $\vec{B}_0$, towards to the x-y plane. As the spins precess in the transverse plane, the electromotive force they generate are picked up by a receive coil that translates the NMR/MRI signal into an electric current in the coil wire, as illustrated in Figure 2.2B. The flip angle, Θ, by which the magnetization is tipped into the x-y plane, is given by

$$\Theta = \gamma B_1 t \quad (2.7)$$

where *t* is the duration of the pulse.

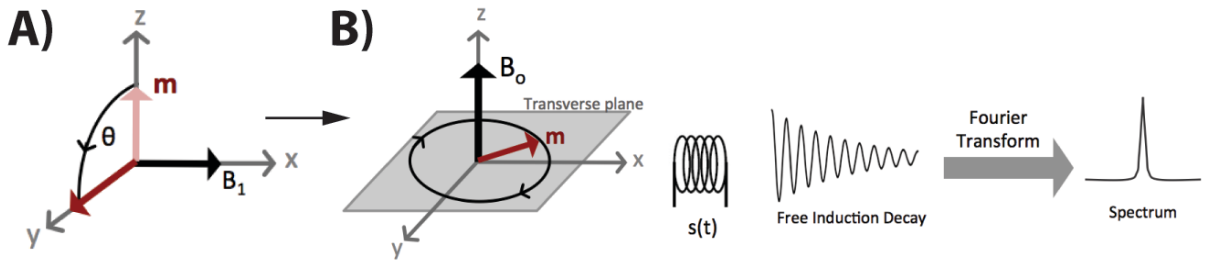

Figure 2.2: *(A) Depiction of the equilibrium magnetization tipped into the transverse plane by an angle Θ according to equation 2.7, after an RF pulse is played out. (B) The tipped magnetization precesses around the main magnetic field, which induces electromotive force that is picked up by a receive coil. That force can be translated into the NMR/MRI signal, s(t), which is in the form of a free induction decay, which can be Fourier transformed into the resulting spectrum (adapted from Swisher 2014* [1]*).*

Once the magnetization is tipped away from its equilibrium position, it undergoes relaxation back towards the longitudinal axis, which is described by two different relaxation time constants, T_1 and T_2. T_1, also known as the spin-lattice relaxation time, relates the relaxation properties governing the recovery of the longitudinal component of the magnetization, M_z, and can be modeled with the following equation:

$$\frac{dM_z}{dt} = -\frac{M_z - M_0}{T_1} \quad (2.8)$$

where M_0 is the equilibrium magnetization along the z-axis. T_2, also known as the spin-spin relaxation time, relates the relaxation properties governing the decay of the transverse component of the magnetization, M_{xy}, and can be modeled with the following equation:

$$\frac{dM_{xy}}{dt} = -\frac{-M_{xy}}{T_2} \quad (2.9).$$

Figure 2.3 shows representative curves of T_1 recovery and T_2 decay, which reflect the exponential return of the magnetization back to the equilibrium state.

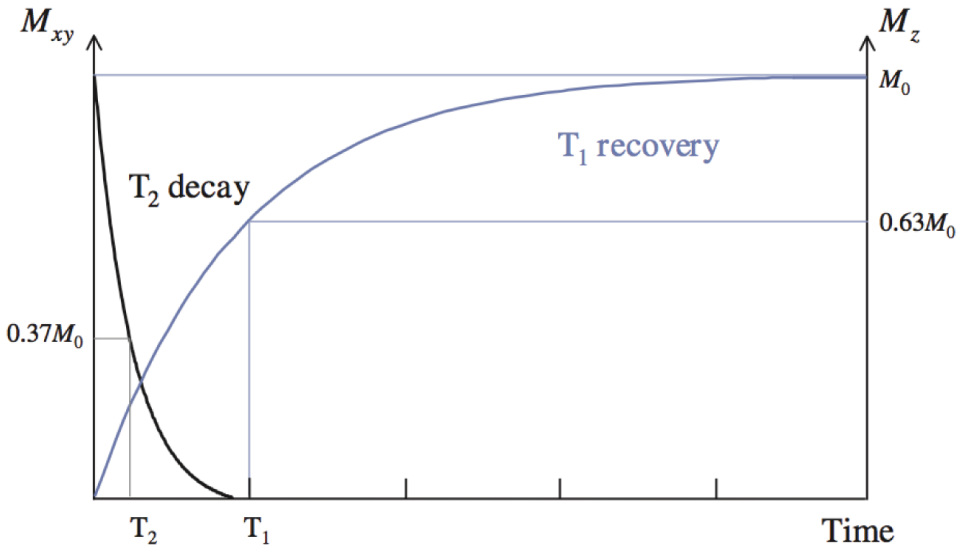

Figure 2.3: *Depiction of the magnetization decay and recovery as governed by the T_1 and T_2 relaxation times, respectively. Both curves shown here are exponential based due to the solutions of the differential equations, 2.8 and 2.9 (adapted from* [2]*).*

The combination of equations 2.5, 2.8, and 2.9 provides a more complete version of the Bloch Equation complete with relaxation of the longitudinal and transverse components:

$$\frac{d\vec{M}}{dt} = \vec{M} \times \gamma\vec{B} - \frac{M_x\hat{\imath}+M_y\hat{\jmath}}{T_2} - \frac{(M_z-M_0)\hat{k}}{T_1} \quad (2.10)$$

2.1.3 k-space and Spatial Localization

Image formation in MRI is done with spatial localization of the Larmor frequency within the volume of interest. With the aid of spatially varying magnetic fields, known as gradients, the external magnetic field, $\vec{B}_0$, is linearly varied in space, with the resulting magnetic field, $\vec{B}(r,t)$, as a function of space defined by the following equation:

$$\vec{B}(r,t) = \vec{B}_0 + \vec{G}(t)\cdot\vec{r} \quad (2.11)$$

with $\vec{G}(t) = G_x(t)\hat{\imath} + G_y(t)\hat{\jmath} + G_z(t)\hat{k}$. Consequently, the spatial set of Larmor frequencies is defined by

$$\vec{\omega}(r,t) = \gamma\vec{B}(r,t) \quad (2.12).$$

The signal received in MRI, $s(t)$, is the sum of the transverse magnetization within the volume of interest and can be defined by the following integral

$$s(t) = \int M(\vec{r},t)\, dV \quad (2.13)$$

where $M(\vec{r},t)$ is the solution to the complete Bloch equation described in equation 2.10 when considering only the behavior of the transverse magnetization.

$$M(\vec{r},t) = M_0(\vec{r})e^{-t/T_2(\vec{r})}e^{-i\omega_0 t}\exp\left(-i\gamma\int_0^t \vec{r}\cdot\vec{G}(\tau)\, d\tau\right) \quad (2.14)$$

Therefore, $s(t)$ can be rewritten as

$$s(t) = \int M_0(\vec{r})e^{-t/T_2(\vec{r})}e^{-i\omega_0 t}\exp\left(-i\gamma\int_0^t \vec{r}\cdot\vec{G}(\tau)\, d\tau\right) dV \quad (2.15)$$

Simplifying equation 2.15 further by demodulating the signal in frequency ω_0 and ignoring the T_2 relaxation term results in

$$s(t) = \int M_0(\vec{r})\exp\left(-i\gamma\int_0^t \vec{r}\cdot\vec{G}(\tau)\, d\tau\right) dV \quad (2.16)$$

$$s(t) = \int M_0(\vec{r})\exp\left(-i2\pi\vec{k}(t)\cdot\vec{r}\right) dV \quad (2.17)$$

$$\text{with } \vec{k}(t) = \frac{\gamma}{2\pi}\int_0^t \vec{G}(\tau)\, d\tau \quad (2.18).$$

Assuming a 2D imaging acquisition, we can write out equation 2.17 as such:

$$s(t) = \iint m(x,y)e^{-i2\pi[k_x(t)x+k_y(t)y]}\, dxdy \quad (2.19)$$

$$s(t) = \Im\{m(x,y)\} \quad (2.20)$$

where $\Im$ denotes the Fourier transform. Equations 2.18 and 2.20 show that the received MRI signal at a time *t* is the 2D Fourier transform (FT) of $m(x,y)$ at a spatial frequency given by equation 2.18. By extension, to obtain the image of interest, one has to sample through spatial frequency space, which is also known as k-space, and apply a 2D

Fourier transform of the resulting signal. To acquire all the spatial frequencies necessary to accurately represent the object of interest, k-space is traversed with time-varying gradients, where $G_x(t)$ and $G_y(t)$ are known as the readout gradient and phase encoding gradient, respectively. Figure 2.4A and 2.4B illustrate a 2D FT imaging sequence and the subsequent traversal through k-space, whereby $G_x(t)$ is used to encode along k_x, while $G_y(t)$ is used to move along k_y. These concepts and equations can be expanded for 3D imaging and Fourier transform as well by adding k_z and $G_z(t)$ terms.

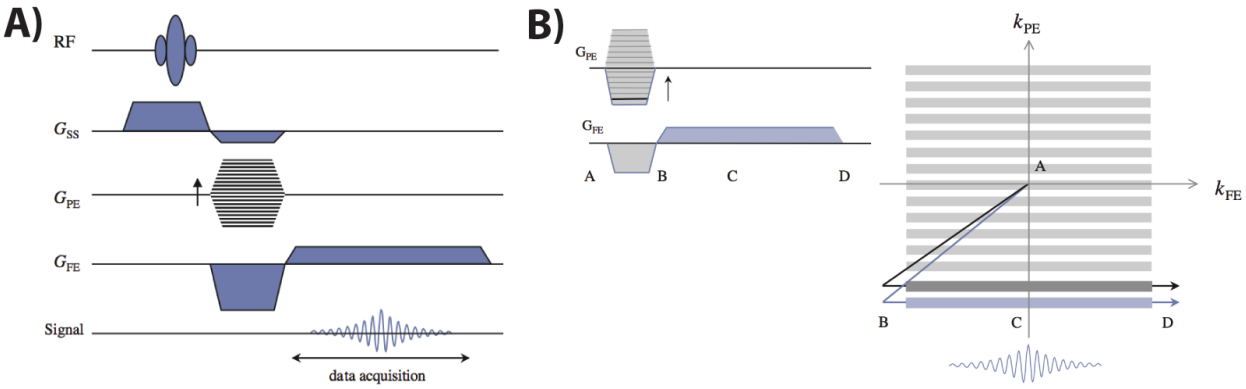

Figure 2.4: *(A) Depiction of a basic 2D FT or 2D gradient echo (GRE) imaging sequence. A slice selective RF pulse (RF and G_{ss} components) is first played out, followed by the two encoding gradients, the frequency encoding G_{FE} (or G_x) and the phase encoding G_{PE} (or G_y). The signal readout can also be seen, with the max signal in the middle of the positive readout gradient lobe. (B) Depiction of how 2D k-space is encoded in a raster fashion based on the readout and phase encoding gradients of the 2D GRE sequence. Point A is the starting point in the center of k-space, with points B-D showing different points during the encoding of a line of k-space (adapted from* [2]*).*

The relationship between field-of-view (FOV) and spatial resolution of the image (δ) with k-space is illustrated with Fourier theory, where

$$FOV = \frac{1}{\Delta k} \quad (2.21)$$

$$\delta = \frac{1}{k_{max}} = \frac{1}{n\Delta k} \quad (2.22)$$

with Δk being the sampling rate in k-space, k_{max} being the extent of k-space, and n being the number of samples. Therefore, to image large FOV objects, one would need to sample several lines of k-space to reduce Δk, and to achieve high spatial resolution images, one would need to sample further out in k-space. The choice of imaging large FOVs and at high spatial resolution needs to be balanced with increased scan times and lower signal-to-noise ratio (SNR); however, as the next section on imaging acceleration will describe, these limitations can be overcome with efficient sampling schemes and reconstruction methods.

2.1.4 Imaging Acceleration

As previously mentioned, the total scan time is related to the number of samples needed to sufficiently cover k-space for a desired FOV and spatial resolution. To improve the inherent trade-off between scan-time and resolution, significant research efforts have been devoted towards development of acceleration methods including compressed sensing, low-rank matrix completion, and parallel imaging for MRI.

Compressed sensing (CS) is the theory of recovering signals that do not meet the Shannon-Nyquist sampling theorem but have a sparse or compressible representation. While the theory was developed with regards to signal processing, it has been adapted for many applications, including MRI. The direct result of applying CS to MRI has been a significant reduction of scan times due undersampling of k-space without loss of image quality. To successfully acquire and reconstruct CS MRI data, four key requirements need to be satisfied [3–5]: first, the MRI data needs to be sparse in some transform domain, such as wavelets or total variation, i.e. where the data can be

represented with only a few sparse coefficients; second, there must be sufficient SNR; third, the undersampling scheme used to acquire k-space must create incoherent artifacts in the sparsfying transform domain (Figure 2.5A), which is usually achieved with pseudo-random k-space sampling patterns that fully sample the center of k-space; lastly, a nonlinear reconstruction that enforces both sparsity of the image representation and data consistency must be used to recover the missing k-space entries. CS has been successfully applied to both single time-point and dynamic imaging, with dynamic imaging being particularly promising due to possible sparser representations of the spatiotemporally correlated data [6,7]. Figure 2.5A illustrates the process of CS by recovering the desired image from undersampled (or partial) k-space using a non-linear approach with the wavelet transform as a sparsifying transform.

Low-rank matrix completion is an extension of CS to matrices, whereby undersampled matrices that are known to be low-rank or approximately low-rank can be fully recovered [8,9]. Low-rank datasets are analogous to sparse images in that they can be represented by a few singular values, similar to representation by a few sparse coefficients. The application of low-rank matrix completion in MRI has been focused on dynamic imaging to exploit spatiotemporal correlations via global low rank and local low rank [10–13], which is shown in Figure 2.5B, as well as in parallel imaging to exploit local k-space correlations [14,15].

Parallel imaging involves utilizing multiple receive elements in a multichannel coil to obtain spatial information about the object of interest and consequently reconstructing the object based on the sensitivity of each individual coil element, allowing for increased spatial coverage and improved SNR [16]. Figure 2.5C illustrates an 8-channel array for

brain imaging, with each individual coil being sensitive to the part of the brain that is nearest to the coil. By exploiting redundancies and local k-space correlations in multichannel data, k-space can be similarly undersampled as described previously, which results in considerable scan time reductions. Reconstructions of undersampled parallel imaging data can be divided into two general approaches: a sensitivity encoding (SENSE) approach [17], which is an image domain reconstruction that utilizes the sensitivity of each coil and uses a separate calibration scan for estimating the coil sensitivities; or generalized autocalibrating partially parallel acquisition (GRAPPA) [18], which is a k-space based method that uses an autocalibrating signal to estimate the weighting of each coil to recover missing k-space entries.

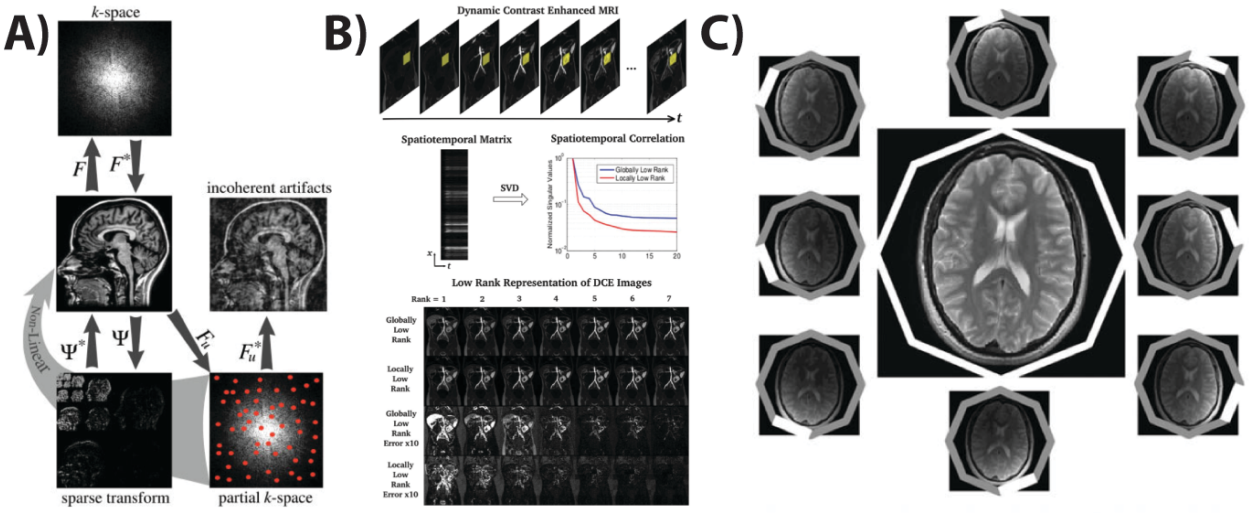

Figure 2.5*: (A) Illustration of the compressed sensing reconstruction framework. The recovery of the desired image (or signal) from the incoherent artifacts created by undersampling k-space is done via a non-linear iterative reconstruction, with a choice of sparsifying transform, such as the wavelet transform depicted here (adapted from* [3]*). (B) Illustration of the low rank matrix completion approach to dynamic contrast enhanced (DCE) imaging. Due to the strong spatiotemporal correlations in the DCE images, the dynamic set of images can be represented by only a few singular values (via local low rank and global low rank), indicating low rankness and consequently the ability to undersample and recover the desired set of images (adapted from* [10]*). (C) Depiction of the reception profile for each individual coil from an 8-channel array. Each coil has strongest signal from the part of the brain nearest to that coil, with the combination of all the coils providing a full image of the brain (adapted from* [16]*).*

Currently, there is significant development in the area of MRI imaging acceleration, including hardware development for parallel imaging, and new reconstruction techniques based on combinations of the above theories since many of the techniques are amenable to additional constraints that can improve the overall reconstruction. Examples include combining low-rank matrix completion with sparse reconstructions to increase compressibility of dynamic MRI and separate images into static background and dynamic signals, while also utilizing a multi-channel setup [19], combining parallel imaging and compressed sensing for accelerated perfusion imaging [7], and bridging the gap between GRAPPA and SENSE for parallel imaging [20].

2.2 Fundamentals of bSSFP imaging

2.2.1 Description of pulse sequence

The balanced steady-state free precession sequence (bSSFP) is a rapid gradient-echo based sequence that has balanced gradients from TR to TR. This zero net dephasing consequently allows magnetization to be recycled, leading to acquisitions that have the highest SNR per unit time [21]. A pictorial representation of the bSSFP

sequence for 3D dynamic volumetric imaging is presented in Figure 2.6. Conventional

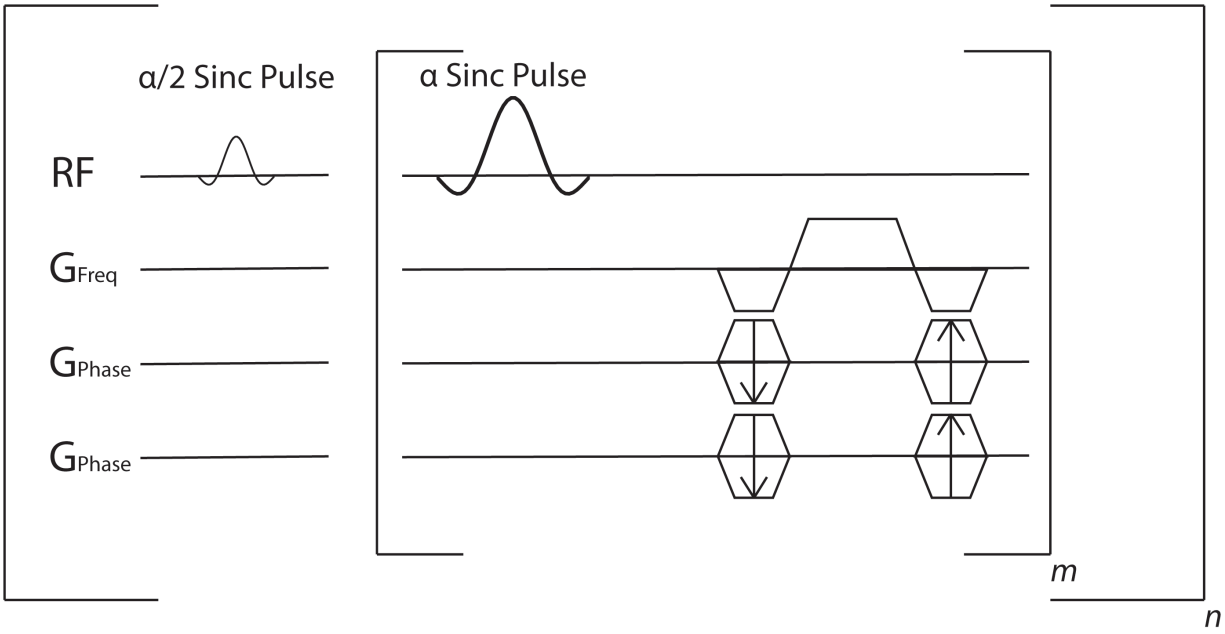

Figure 2.6: *Depiction of a 3D dynamic version of the bSSFP sequence, with an $\alpha/2$ preparation pulse prior to the image acquisition portion, which consists of alternating polarity α pulses and fully balanced gradients. Each volume has m phase encodes, and there are n total time-points.*

^{1}H bSSFP is typically used for morphological imaging [21,22], such as cardiac imaging and angiography, due to the mixed T_1 and T_2 contrast of the sequence, which is illustrated by the following steady-state magnetization equation:

$$M_{SS} = \frac{1}{2} M_0 \sqrt{\frac{T_2}{T_1}}. \quad (2.23).$$

Other than featuring fully balanced gradients, the bSSFP sequence features two other important necessary attributes: a catalyzation scheme, and alternating polarity pulses, which is shown in Figure 2.7A. As shown in Figure 2.6 conventional bSSFP imaging consists of an $\alpha/2$ preparation pulse prior to imaging that provides a smooth transition to the steady-state, as shown in Figure 2.7B, and removes potential signal fluctuations that may cause severe artifacts during k-space acquisition, as shown in

Figure 2.7C [21,23]. Other catalyzation schemes exist, such as a variable flip angle scheme, that allows for improved off-resonance response [24,25]. The alternating polarity pulses further help signal stabilization when the pulse rotation angles are imperfect and are commonly used in sequences with magnetization recycling [26].

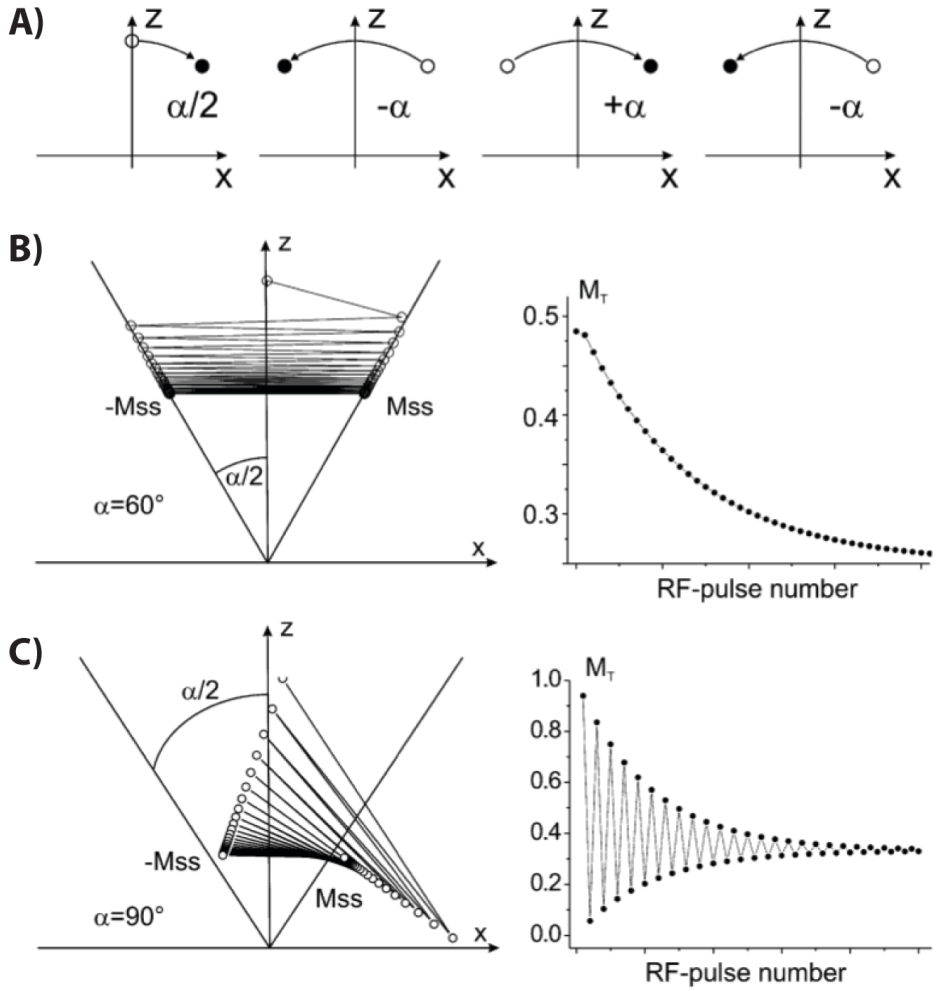

Figure 2.7: *(A) Depiction of the magnetization, represented as a single circle, after an $\alpha/2$ preparation pulse and subsequent alternating polarity α pulses. The magnetization essentially tips back and forth into the positive and negative x direction, always lying $\alpha/2$ away from the z-axis. (B) A view of how the magnetization approaches the steady-state in ^{1}H bSSFP imaging. The approach is smooth with the $\alpha/2$ preparation pulse, as seen on the graph on the right. (C) Conversely, in the absence of the $\alpha/2$ preparation pulse, the approach to the steady-state is not smooth, leading to signal fluctuations in k-space and severe image artifacts. (adapted from* [21]*)*

The fast imaging properties of bSSFP, with TRs in the range of 3-6 ms for ^{1}H, make it a very attractive sequence for hyperpolarized (HP) ^{13}C imaging due to the non-recoverable nature of hyperpolarized magnetization (which is discussed in more detail in section 2.3). With such short acquisition times and magnetization recycling, bSSFP provides very high spatial resolution images for HP ^{13}C imaging [23,27,28].

While imaging at the steady-state is certainly advantageous for ^{1}H, that is not the case for HP ^{13}C, making the sequence somewhat of a misnomer when applied to HP ^{13}C imaging. Since we want to take advantage of the hyperpolarized signal before it irreversibly decays to thermal equilibrium, we have to image during the transient phase of the bSSFP sequence. The description of the magnetization during the transient phase is quite straightforward since the balanced gradients mean the spins are not spatially dephased and can be represented by one magnetization vector [23]. To understand the signal decay during bSSFP imaging from pulse to pulse, we can use a transition matrix to follow the magnetization from one α pulse to the next, after the magnetization has been tipped by $\alpha/2$, as described above [29]. The transition matrix, T, showing relaxation and rotation is

$$T = E_{TR/2} R_z(\pi) R_x(\alpha) E_{TR/2} \quad (2.24)$$

where the x and z rotations can be represented by the following matrices

$$R_z(\alpha) = \begin{pmatrix} \cos\alpha & \sin\alpha & 0 \\ \sin\alpha & \cos\alpha & 0 \\ 0 & 0 & 1 \end{pmatrix} \quad (2.25)$$

$$R_x(\alpha) = \begin{pmatrix} 1 & 0 & 0 \\ 0 & \cos\alpha & \sin\alpha \\ 0 & -\sin\alpha & \cos\alpha \end{pmatrix} \quad (2.26)$$

and T_1 and T_2 decay can be represented by the following matrix

$$E(t) = \begin{pmatrix} e^{-t/T_2} & 0 & 0 \\ 0 & e^{-t/T_2} & 0 \\ 0 & 0 & e^{-t/T_1} \end{pmatrix}. \quad (2.27)$$

The signal decay equation for on-resonance bSSFP imaging of HP ^{13}C compounds is as follows:

$$M_{xy,n} = M_{z,0} \sin {}^{\alpha}/_{2} \left(E_1 * (\cos {}^{\alpha}/_{2})^2 + E_2 * (\sin {}^{\alpha}/_{2})^2\right)^n \quad (2.28)$$

where α is the flip angle, E_1 = exp($-TR/T_1$), E_2 = exp($-TR/T_2$), and n is the pulse number. (An alternative signal model has also been developed that is equivalent to the one above [23].) This equation shows that the bSSFP sequence has a mix of T_1 and T_2 contrast that can be tuned with the choice of α [21,30]. Typically, the choice of α comes down to the T_2 of the compounds as well as the desired spatiotemporal resolution, with control of SNR being the biggest consideration.

2.2.2 Off-resonance effects and artifacts

While the previous section described how to model the signal of on-resonance spins, conventional bSSFP imaging has to be applied with care regarding off-resonance spins and what kind of effect they have on image acquisition and reconstruction. For the bSSFP sequence, the off-resonance effects, which may be due to field inhomogeneity, susceptibility artifacts, and chemical shift, can be additionally modeled to get the signal response as a function of frequency. The dephasing of spins during TR due to the local precession frequency of the spins can lead to signal dropouts in the image, which are termed banding artifacts. This effect is shown in Figure 2A and 2B, with the locations of the signal dropouts occurring periodically at $1/TR$ ($\pm 1/2TR$ from center). The short TR's necessary for high SNR imaging with bSSFP also serve to help the off-resonance

response, with the shorter TRs allowing the sequence to be less sensitive to the off-resonance response.

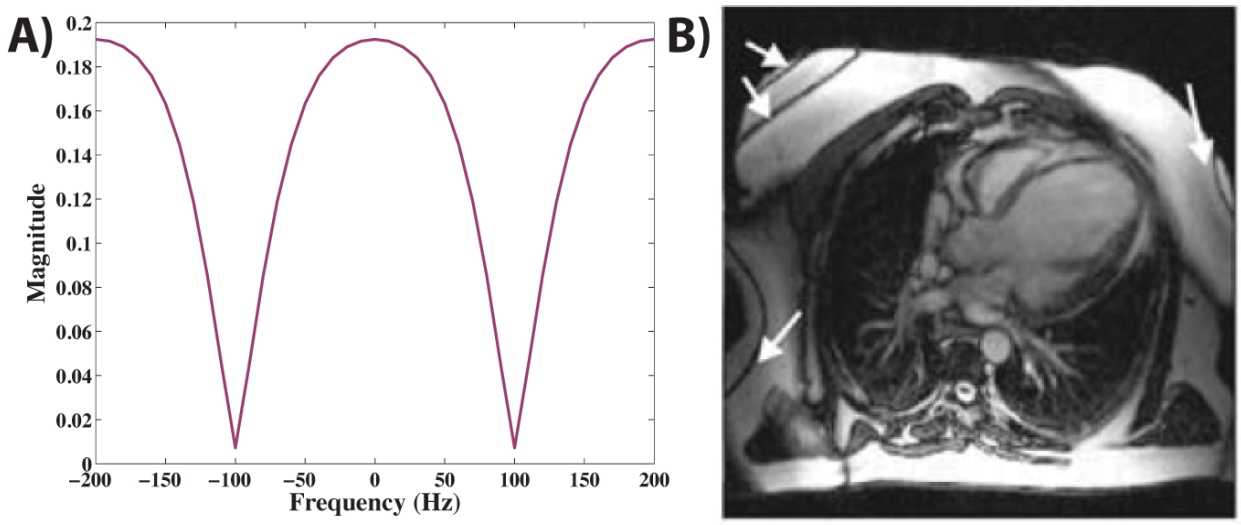

Figure 2.8: *(A) Simulation of magnitude vs. frequency for a bSSFP acquisition with a 5 ms TR. The bands at ±100 Hz or ±1/2TR show the signal dropout that corresponds to the well-known banding artifact. (B) Illustration of the banding artifact from a cardiac acquisition. The white arrows correspond to signal dropouts as seen in part A (adapted from* [21]*).*

Banding artifacts are an important component of spectrally selective bSSFP imaging because of the coupling of the spectral selectivity of the RF pulse and the frequency response of the bSSFP sequence. In general, the periodicity of the bSSFP frequency response has the following property: near on-resonance low and high flip angles excite magnetization in the expected manner, while at the aforementioned bands, the opposite behavior can be seen, with low flip angles producing considerable excitation and high flip angles having little effect. This effect has been termed “excitation banding artifact” and is important to consider when dealing with multiple resonances, such as HP [1-^{13}C]pyruvate metabolism [28]. Typically, simulations and phantom

studies should be done prior to imaging to calculate the optimal TR and pulse width and time-bandwidth that will avoid this artifact.

The bSSFP sequence is most advantageous when imaging a single resonance since the pulse width and TR and can be shortened as much as possible without having to worry about any off-resonance effects. However, as has been demonstrated previously and will be shown in chapters 5 and 6, the bSSFP sequence can be designed to image multiple resonances within one acquisition.

2.3 DNP hyperpolarization

2.3.1 Hyperpolarization

The equation for calculating polarization was previously given by equation 2.3 and can be rewritten in the following manner:

$$\mathrm{P} = \tanh\frac{-\gamma\hbar B_0}{2kT} \approx \frac{-\gamma\hbar B_0}{2kT} \quad (2.27)$$

with the approximation being valid for the regime of calculating thermal polarization, which is about 10^{-6} for a given nucleus. The polarization therefore depends on the gyromagnetic ratio, magnetic field strength, and temperature. Figure 2.9 illustrates the polarization vs. temperature for ^{1}H, ^{13}C, and e^{-}, with the e^{-} gyromagnetic ratio being ~1000 times greater than ^{1}H or ^{13}C. Due to this large difference in gyromagnetic ratio, the polarization of e^{-} is ~100 times the polarization of ^{13}C at 1 K, with the e^{-} having nearly full polarization.

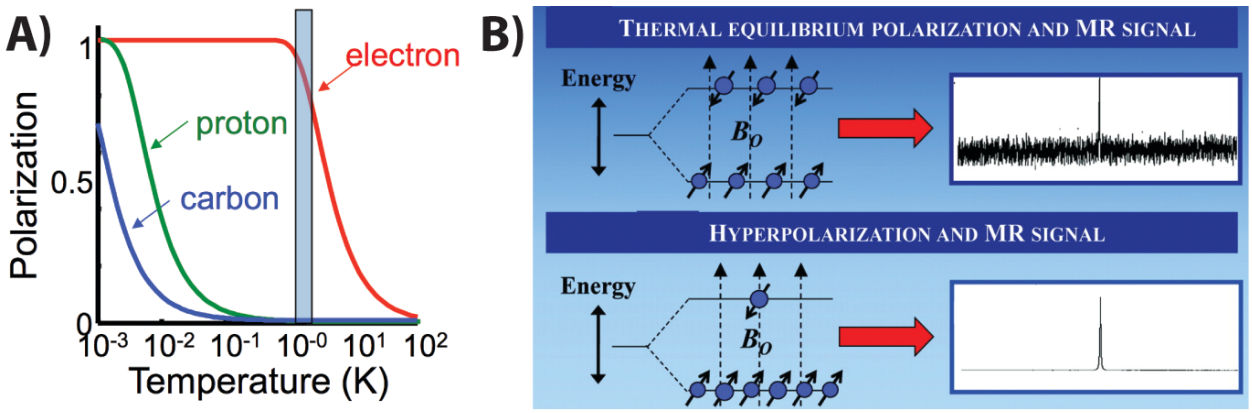

Figure 2.9: *(A) Plot of polarization vs. temperature for e^-, ^1H, and ^{13}C. The polarization of e^- at 1 K is ~1 due to the ~1000 times greater gyromagnetic ratio compared to ^1H and ^{13}C. As described later, the e^- polarization can be transferred to ^{13}C via dynamic nuclear polarization. (B) Comparison of the spin distribution at thermal polarization and hyperpolarization states. Hyperpolarization causes a considerable redistribution of spins to one energy state, increasing the SNR by >10,000-fold.*

The concept of hyperpolarization, in its most basic description, refers to increasing the polarization of the nucleus of interest by several orders of magnitude above thermal polarization, effectively creating a redistribution of the energy population levels, as shown in Figure 2.9B [31]. There are several methods that can drive nuclei into this nonequilibrium state, including optical pumping, parahydrogen-induced polarization (PHIP), and dynamic nuclear polarization [31]. The first two procedures will not be discussed further as the studies presented in subsequent chapters utilized dynamic nuclear polarization for HP ^{13}C imaging.

2.3.2 Dissolution dynamic nuclear polarization

Carbon is the element present in all organic molecules, and the combination of magnetic resonance imaging and carbon can potentially provide a noninvasive way to obtain considerable information on metabolism and other biochemical processes that otherwise are not be feasible with ^1H imaging. Unfortunately, 99% of carbon is ^{12}C and

not NMR active, with only 1% being NMR detectable ^{13}C. Coupled with the 4-fold lower gyromagnetic ratio compared to ^{1}H, the sensitivity of thermal ^{13}C MRI is too low for conventional *in vivo* scanning akin to ^{1}H MRI. Therefore, hyperpolarization is needed to increase the SNR and allow for rapid imaging of ^{13}C compounds.

Dynamic nuclear polarization (DNP), also known as the Overhauser effect, is the transfer of polarization from the e^- to the ^{13}C nuclei via irradiation at an appropriate frequency. There are two general processes that transfer the electron polarization to the ^{13}C nucleus in a sample: solid effect and thermal mixing. These two processes are direct effects, whereby the ^{13}C nuclei are physically located very close to an e^-, and the electron-nuclear spin interaction governs the whether the solid effect or thermal mixing causes the polarization transfer. Spin diffusion is an additional process that allows further away ^{13}C nuclei to be polarized as well. Figure 2.10 displays the distribution of spins and how they get polarized.

For *in vivo* HP ^{13}C imaging the samples typically consist of the following components: enriched ^{13}C compound, such as [1-^{13}C]pyruvate or [^{13}C]urea; an electron paramagnetic agent (EPA) that serves as the source of unpaired electrons; gadolinium or other lanthanides to shorten the e^- T_1 for increased polarization; and glycerol or other compounds to help glassing if necessary [32]. Typically, multiple iterations of a sample preparation are made and tested to obtain the optimized version that gives the best polarization. Consequently, the choice of EPA will affect what polarization transfer mechanism occurs (solid effect or thermal mixing), and what irradiation frequency is optimal.

As equation 2.27 shows, the external conditions necessary for significant polarization enhancement involves high magnetic fields and low temperature. Current cryogenic technology makes temperatures of <1 K achievable, and recent publications have shown that field strengths of ~5 Tesla provide optimal polarization. While DNP has been around since the 1950s with the Overhauser effect, Ardenkjaer-Larsen et al. only reported the technique of rapidly dissolving the sample into a dilute room temperature solution, while retaining the enhanced nuclear polarization, in 2003 [33]. This development opened the door for dissolution dynamic nuclear polarization (dDNP) to be applied to biomedical applications, including HP ^{13}C MRI. Currently, two commercial polarizers have been mainstays of HP ^{13}C imaging: the HyperSense (Oxford Instruments, UK), which is a single-sample polarizer based on the design used by Ardenkjaer-Larsen et al. [33] and has been utilized for *in vitro* and preclinical *in vivo* studies (Figure 2.10B); and the SpinLab (GE, Waukesha, WI), which is a multi-sample polarizer [34] that was built with human studies in mind, and has an additional quality control system that measures key parameters, including the polarization level, pH, concentration, temperature, and EPA concentration, which helps determine whether the solution is to be accepted or rejected for human injection (Figure 2.10C).

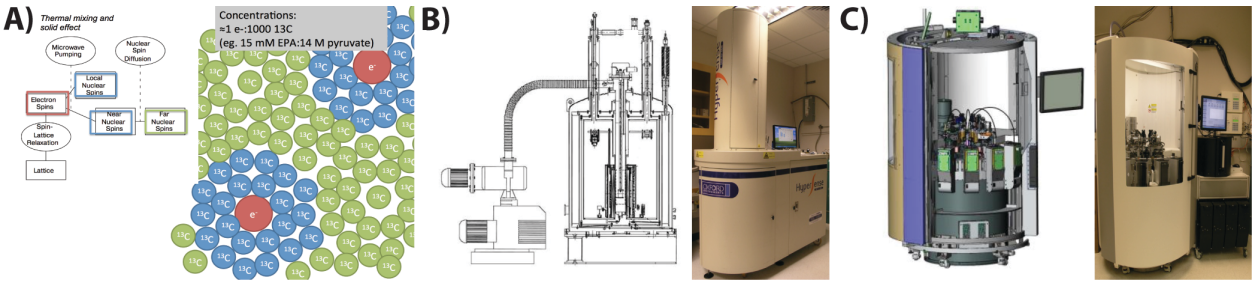

Figure 2.10: *(A) Illustration of the distribution of ^{13}C nuclei relative to the e^- in a given sample used in DNP. The processes that transfer the e^- polarization are outlined in blue and green for near and far ^{13}C nuclei, respectively. (B) Schematic of a preclinical polarizer and a picture of the commercial HyperSense. (C) Schematic of the SpinLab system and a picture of the 5 Tesla SpinLab at UCSF, with the attached QC system for human studies. (adapted from* [33] *and Chen 2017* [35]*)*

2.3.3 Application to cancer metabolism and microenvironments

The rapid development of dDNP over the last decade has led to several applications of HP ^{13}C MRI in multiple diseases and organs, with emphasis on metabolism and perfusion (section 2.3.4). [1-^{13}C]Pyruvate is the modt wodely used molecule in HP ^{13}C MRI due its advantageous chemical properties, including long T_1 and high polarization, and ability to probe several metabolic pathways, as shown in Figure 2.11A [32]. Consequently, pyruvate has been applied in several studies of cancer because of the ability to interrogate the Warburg effect (Figure 2.11B), which is a hallmark of cancer that states tumor cells have increased conversion to lactate compared to normal cells [36]. Monitoring pyruvate-to-lactate, pyruvate-to-alanine, and pyruvate-to-bicarbonate conversion has provided significant information on tumor aggressiveness and treatment response [37–41]. Several different preclinical models of cancer have been studied with HP [1-^{13}C]pyruvate, including transgenic adenocarcinoma of mouse prostate (TRAMP) [41,42], brain cancer [43], hepatocellular

carcinoma [44], and breast cancer [45]. Current research focuses on optimizing acquisition schemes for obtaining all the metabolite information, as well as modeling the kinetics of the metabolic conversion [46]. Other probes have also been developed that focused on other aspects of cancer biology, such as acidity of the tumor microenvironment ([^{13}C]bicarbonate [47]) and necrosis ([1,4-$^{13}C_2$]fumarate [48]), as well as metabolism specific to certain cancers ([2-^{13}C]pyruvate, [5-^{13}C]glutamine, [1-^{13}C]α-ketoglutarate, among others [49,50]).

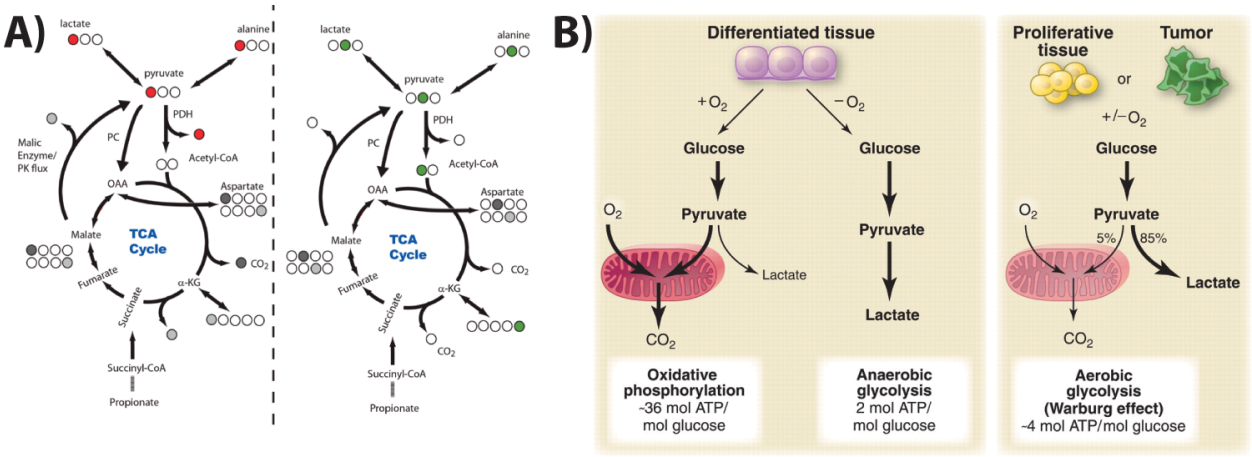

Figure 2.11: *(A) Depiction of the fate of the ^{13}C label of either [1-^{13}C]pyruvate (red) or [2-^{13}C]pyruvate (green). [1-^{13}C]Pyruvate is typically used to monitor the conversion to lactate, alanine, and bicarbonate, while [2-^{13}C]pyruvate is used for probing the TCA cycle (adapted from* [32]*). (B) Depiction of ATP production from oxidative phosphorylation and anaerobic glycolysis can be seen, with oxidative phosphorylation being much more efficient in the presence of oxygen. Healthy, differentiated cells (left) primarily use oxidative phosphorylation for ATP production, whereas tumor tissue (right) primarily undergoes the relatively inefficient anaerobic glycolysis in the absence or presence of oxygen, a process commonly known as the Warburg effect (adapted from* [36]*).*

2.3.4 Application to perfusion

Perfusion, and by extension permeability, have also been well studied with HP ^{13}C imaging, with regards to cancer and other diseases. Using HP ^{13}C tracers for perfusion offers advantages over ^{1}H MRI including a direct relationship between tracer

concentration and signal, as well as high contrast-to-noise due to lack of background signal from endogenous carbon [51]. The three most common tracers developed so far, which are shown in Figure 2.12A, are urea (both ^{14}N and ^{15}N labeled), HP001, and tert-butanol, with each compound having different chemical properties that affect their *in vivo* distribution based on lipid bilayer permeability and transport [52].

Urea has gained the most traction for looking at perfusion *in vivo*, owing to its long T_1, high polarization, and well-characterized safety profile since it's an endogenous metabolically-inactive compound [51,53]. Several preclinical studies have focused on using urea to monitor perfusion in cancerous tissue [41,51,54]. Figure 2.12B illustrates the changes in vasculature from normal tissue to tumor tissue, with tumor vasculature lacking organization as well as consistent vessel diameter, among other distortions from healthy vessels [55,56]. Additionally, correlations between the perfusion with pyruvate metabolism have been performed, as there exists a mismatch in metabolism and perfusion such that areas of high metabolism and low perfusion are associated with higher tumor aggressiveness and less response to therapy [41]. Other applications of urea have gone toward establishing it as a potential renal function biomarker, owing to the filtration characteristics of the kidney, coupled with T_2 variations in the renal cortex, medulla, and pelvis after ^{15}N labeling [27,53,57,58].

HP001 and tert-butanol are both exogenous compounds that exhibit certain advantageous properties over urea with regards to perfusion [52,54]. HP001 has a very long *in vivo* T_1 and the potential to better describe perfusion in the kidneys since it is not reabsorbed, unlike urea. Furthermore, with a chemical shift of 23 ppm, it resonates much farther away from various metabolically active probes, like [1-^{13}C]pyruvate (171

ppm), allowing more efficient acquisition schemes. Tert-butanol, compared to urea and HP001, is freely diffusible, and can provide perfusion information in nearly every organ, including the brain where it can cross the blood-brain barrier. Like HP001, tert-butanol also resonates far away (chemical shift of 70 ppm) from metabolically active probes.

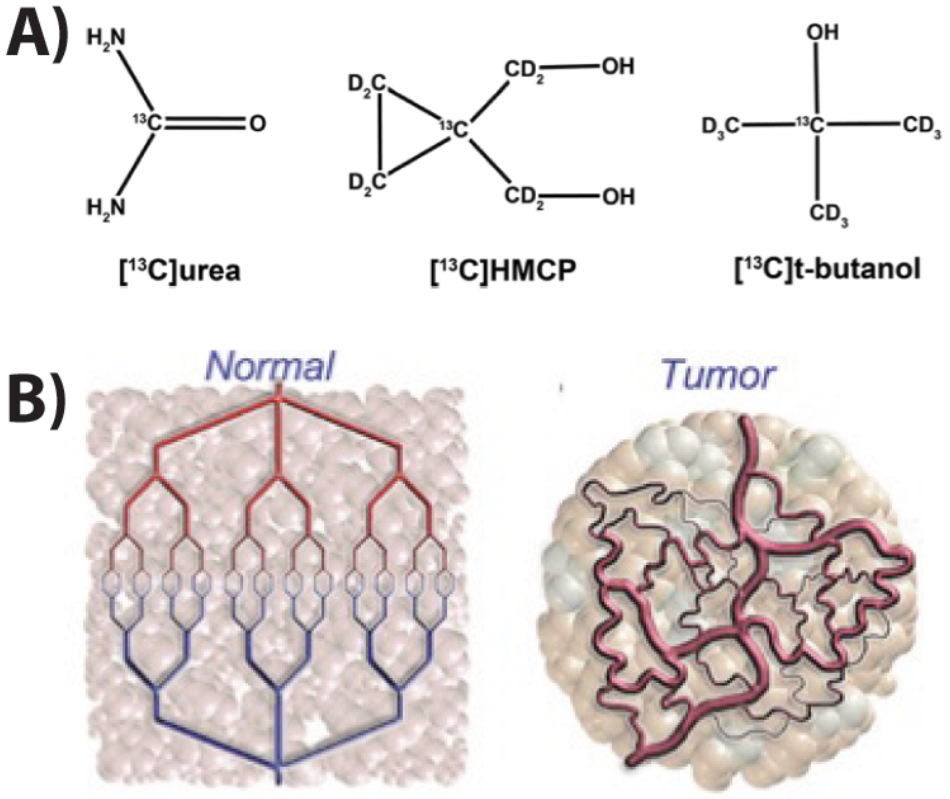

Figure 2.12: *(A) Illustration of the structures of the three most common HP ^{13}C probes currently studied for perfusion and permeability: urea, HP001, and tert-butanol (adapted from* [52]*). (B) Illustration of the vasculature differences between healthy and tumor tissue, with visible differences in organization and structure (adapted from* [55]*).*

More research is currently needed to assess the capability of each of these three probes for calculating perfusion and permeability. A recent study showed the potential of using all three in tandem and using their individual biological characteristics to more efficiently calculate those parameters. Furthermore, as these compounds are

metabolically inactive and are thus a single resonance, high spatiotemporal resolution is possible.

2.3.5 Clinical Translation

The initial Phase I first-in-human study of HP ^{13}C MRI was performed at UCSF in 2010-2012, focusing on [1-^{13}C]pyruvate injections in patients with prostate cancer [59]. This study was able to show the safety profile of injected [1-^{13}C]pyruvate, while also monitoring metabolism and correlating the results to both ^{1}H MRI and biopsy results. This study used relatively simple acquisitions, including 1D, 2D and 3D spectroscopy/spectroscopic imaging, as well as an “alpha” polarizer system (similar to HyperSense) placed in a clean room for sterility purposes.

The recent development of the SPINlab system has provided the capability of human injection in a relatively easier fashion compared to the Phase I study above. The use of closed sterile fluid paths and the addition of the QC system and 4 sample pods allow for rapid multiple injections in patients, without the need of a clean room. The SPINlab system also has a helium regeneration unit that eliminates the need for regular liquid helium refills. Furthermore, the current system operates at 5 Tesla and 0.8 K, allowing for a two-fold increase in ^{13}C polarization compared to the previous human studies.

Several recent studies have expanded on the initial Phase I first-in-human study for current Phase II human studies, including acquisitions in brain cancer, liver cancer, breast cancer, heart, and metastatic cancer, on top of continuing prostate cancer studies [60–64]. Additionally, recent developments in both sequence and coil

development have provided improved spatiotemporal resolution in these *in vivo* studies, including application of 3D compressed sensing MRSI and echo-planar imaging [5,65]. Future studies are planned to include multi-channel coils, which would provide better coverage and different avenues for acquisition and reconstruction.

Chapter 3: Development of High Resolution 3D Hyperpolarized Carbon-13 MR Molecular Imaging Techniques

3.1 Abstract

The goal of this project was to develop and apply techniques for T_2 mapping and 3D high resolution (1.5 mm isotropic; 0.003 cm^3) ^{13}C imaging of hyperpolarized (HP) probes [1-^{13}C]lactate, [1-^{13}C]pyruvate, [2-^{13}C]pyruvate, and [^{13}C,$^{15}N_2$]urea in vivo [66]. A specialized 2D bSSFP sequence was implemented on a clinical 3T scanner and used to obtain the first high resolution T_2 maps of these different hyperpolarized compounds in both rats and tumor-bearing mice. These maps were first used to optimize timings for highest SNR for single time-point 3D bSSFP acquisitions with a 1.5 mm isotropic spatial resolution of normal rats. This 3D acquisition approach was extended to serial dynamic imaging with 2-fold compressed sensing acceleration without changing spatial resolution. The T_2 mapping experiments yielded measurements of T_2 values of greater than 1 s for all compounds within rat kidneys/vasculature and TRAMP tumors, except for [2-^{13}C]pyruvate which was ~730 ms and ~320 ms, respectively. The high resolution 3D imaging enabled visualization the biodistribution of [1-^{13}C]lactate, [1-^{13}C]pyruvate, and [2-^{13}C]pyruvate within different kidney compartments as well as in the vasculature. While the mouse anatomy is smaller, the resolution was also sufficient to image the distribution of all compounds within kidney, vasculature, and tumor. The development of the specialized 3D sequence with compressed sensing provided improved structural and functional assessments at a high (0.003 cm^3) spatial and 2 s temporal resolution in

vivo utilizing HP ^{13}C substrates by exploiting their long T_2 values. This 1.5 mm isotropic resolution is comparable to ^{1}H imaging and application of this approach could be extended to future studies of uptake, metabolism, and perfusion in cancer and other disease models and may ultimately be of value for clinical imaging.

3.2 Introduction

Dissolution dynamic nuclear polarization (DNP) of carbon-13 enriched compounds with the aid of an electron paramagnetic agent and then rapidly dissolved, can increase the liquid state NMR signal-to-noise ratio (SNR) more than 10,000 fold [33]. MRI of hyperpolarized (HP) ^{13}C substrates is a powerful tool for detecting the metabolic and physiological changes that underlie disease processes in a noninvasive fashion [31,32,50,59,67]. However, the hyperpolarized signal is lost rapidly due to T_1 relaxation metabolic conversion, resulting in a limited temporal window for imaging. Furthermore, each applied radiofrequency pulse depletes the non-recoverable magnetization, creating design challenges for fast imaging approaches aimed at efficiently utilizing the hyperpolarized magnetization [33]. Therefore, specialized developments in MRI sequence design are required for hyperpolarized carbon-13 imaging. The implementation of different MRI data sampling strategies, including fast MRSI approaches such as echo-planar spectroscopic imaging with compressed sensing [5,68] and spiral MRSI [43], echo planar or spiral imaging with spectral-spatial excitation [65,69–72] and concentric rings trajectories [73], have all been applied in preclinical HP studies. While these sequences provided coverage and either sufficient spectral resolution (MRSI) or imaging of individual resonances (MRI), they were limited by

relatively low spatial resolution, which can potentially limit their application.

The balanced steady-state free precession (bSSFP) sequence has the advantage of offering higher signal-to-noise ratios per unit time than other sequences [21,22]. This has been extensively demonstrated in proton imaging [74–76], and has consequently been utilized in HP ^{13}C imaging [53,77–80] for metabolic and perfusion imaging. As described previously [23], bSSFP sequences use the hyperpolarized magnetization effectively, exploiting the long relaxation times associated with various hyperpolarized probes. T_2 mapping can provide a valuable tool to measure the T_2 relaxation times of these probes in vivo and has been successfully performed with the bSSFP sequence with hyperpolarized urea [53], thereby allowing proper optimization of subsequent imaging acquisitions for the specific T_2 values.

Hyperpolarized ^{13}C pyruvate MRI studies have demonstrated several potential applications including cancer [31], diabetes [81], and cardiac disease [72,82]. The hyperpolarized lactate-to-pyruvate ratio reflects changes in glycolysis related to the enzyme lactate dehydrogenase (LDH) that is up-regulated in human cancers including prostate [31,67,83,84]. Measurements of LDH kinetics by HP ^{13}C-pyruvate MR have shown significant differences between cancer and normal tissues and with therapeutic response in preclinical models [38,85–87]. The feasibility and safety of HP ^{13}C-pyruvate MRI was demonstrated in a Phase 1 clinical trial of 31 prostate cancer patients [59]. Also, recent studies incorporating new sequence development have shown the utility of this MR molecular imaging technique to probe not only metabolism, but also perfusion and vascular permeability [51,52,54,88]. Additionally, recent studies of tumor pathogenesis have focused on the heterogeneous nature of tumors, based on the

hypothesis that subpopulations of tumor cells may drive proliferation and aggressiveness of the disease, specifically as regards to the concepts of lactate shuttling and the “reverse Warburg effect,” suggesting the importance of lactate as a probe for metabolism [83]. The spatial heterogeneity of tumor metabolism and perfusion is not readily measured by current clinical methods, but may have considerable diagnostic and predictive value, such as in assessing aggressiveness and guiding biopsies [89,90]. HP [^{13}C]urea has been applied to image tumor perfusion [51], and can be readily combined with metabolic probes to simultaneously assess changes in both metabolism and perfusion [54] and has also been recently applied for cardiac perfusion imaging [88]. Urea is also important in renal function and renal urea handling can be measured using hyperpolarized MRI [52,53]. Hyperpolarized urea furthermore has an exceptional safety profile as a medical imaging contrast agent.

The goal of this study was to investigate a new approach for tissue characterization using high resolution HP MR imaging of [1-^{13}C]pyruvate, [2-^{13}C]pyruvate, [1-^{13}C]lactate, and [^{13}C,$^{15}N_2$]urea in vivo in both normal rats and tumor-bearing mice at 3 Tesla. T_2 mapping with a 2D bSSFP sequence allowed identification of the distribution of T_2 values of each compound in different biological compartments in vivo at a high in-plane resolution. A custom 3D bSSFP sequence was then applied for high resolution imaging of each compound, including both single time-point and serial dynamic images. This was performed with the incorporation of compressed sensing as well as using parameters derived from the T_2 mapping results. In this project, the biodistribution and temporal dynamics of the injected HP compounds was investigated

with 1.5 mm isotropic resolution within rat and mouse kidneys and vasculature as well as in tumors from transgenic mouse models of cancer.

3.3 Methods

3.3.1 Hyperpolarization

Neat [1-^{13}C]pyruvic acid (Sigma Aldrich, St. Louis, MO, USA) was mixed with 15 mM trityl radical (GE Healthcare, Waukesha, WI) and 1.5 mM Gd-DOTA (Guerbet, Roissy, France). Neat [2-^{13}C]pyruvic acid (Sigma Aldrich) was mixed with 15 mM trityl radical (GE Healthcare, Waukesha, WI) and 1.5 mM Gd-DOTA. Neat [1-^{13}C]lactic acid (Sigma Aldrich) was mixed with a small amount of distilled water for liquification and mixed with 15 mM trityl radical OX063 (Oxford Instruments, Abingdon, UK) and 1 mM Gd-DOTA. [^{13}C,$^{15}N_2$]Urea (Sigma Aldrich) was dissolved in glycerol and mixed with 15 mM trityl radical OX063 (Oxford Instruments, Abingdon, UK) and 1.5 mM Gd-DOTA. Each compound was individually polarized in either a HyperSense dissolution DNP system (Oxford Instruments, Abingdon, UK) operating at 1.35 K and 3.35 T (lactic acid [91] and urea [53]) for ~1hr or a SpinLab (GE Healthcare, Waukesha, WI), operating at 0.8K and 3.35T (pyruvic acids [34]) for ~2hrs to achieve polarizations of 20-25% (urea and lactate) to 30-35% (pyruvic acids). The dissolution media and resulting concentration for each compound was as follows: 4.5 mL of 80 mM NaOH/40 mM Tris buffer for [1-^{13}C]pyruvic acid resulting in 80 mM [1-^{13}C]pyruvate (hereafter referred to as C_1-pyruvate); 4.5 mL of 80 mM NaOH/40 mM Tris buffer for [2-^{13}C]pyruvic acid resulting in 80 mM [2-^{13}C]pyruvate (hereafter referred to as C_2-pyruvate); 4.5 mL of 160 mM NaOH/40 mM Tris buffer for [1-^{13}C]lactic acid resulting in 160 mM [1-^{13}C]lactate

(hereafter referred to as lactate); 5mL of 1x phosphate-buffered saline for [^{13}C,$^{15}N_2$]urea resulting in 110 mM [^{13}C,$^{15}N_2$]urea (hereafter referred to as urea).

3.3.2 Animal Handling

All animal studies were done under protocols approved by the University of California San Francisco Institutional Animal Care and Use Committee (IACUC). Six normal Sprague-Dawley rats (three for T_2 mapping, three for 3D imaging), six transgenic adenocarcinoma of mouse prostate (TRAMP) mice [42], and one oncogene-driven breast cancer mouse [92] were used in these studies. Both the rats and mice were anesthetized with isoflurane (1.5%) and placed in a supine position on a heated pad throughout the duration of the experiments. After polarization and dissolution, each of the compounds were injected into the animal via tail vein catheters: ~3 mL over 12 s for each rat and ~500 µL over 15 s for each mouse.

3.3.3 Image Acquisition and Reconstruction

All experiments were performed on a 3T GE MR750 clinical scanner (GE Healthcare, Waukesha, WI) with multinuclear capability. The studies were performed with dual-tuned $^{1}H/^{13}C$ transceiver birdcage radiofrequency coils that have either a diameter of 8 cm for rats or a diameter of 5 cm for mice [38].

All acquisitions were performed using a custom ^{13}C bSSFP sequence with either one phase encoding dimension (projection along the anterior-posterior direction) (T_2 Mapping) or two (3D imaging) phase encoding dimensions. In each acquisition, a flip angle of 180 degrees was used for optimized SNR, off-resonance insensitivity, and near

optimal k-space filtering effect [22]. $\alpha/2$ – TR/2 preparation pulses were used to reduce transient state signal oscillations [23]. A basic sinc RF pulse was used for both the 90° preparatory pulse and 180° pulses train with linear scaling (3.2 ms pulse duration, TBW = 4 for T_2 mapping and 1.6 ms pulse duration, TBW = 4 for 3D imaging). A 1mL enriched [^{13}C]urea vial phantom (6.0M) was used for frequency and power calibration. For anatomical localization, 3D bSSFP proton (16 x 8 x 4.8 cm, 256 x 128 x 80, 5.1 ms TR, 50° flip angle) images were obtained for rat studies, while T_2-weighted fast spin echo proton (6 x 6 x 8 cm, 256 x 192 x 40, 7.6 s TR) images were obtained for mouse studies. The acquisitions were started at 30 s after injection for T_2 mapping and 20 s for all 3D imaging.

The T_2 mapping for C_1-pyruvate and lactate in rat kidneys (Figure 3.1 and Figure 3.3), as well as pyruvate, lactate, and urea in mouse tumors (Figure 3.1 and Figure 3.4) were acquired similarly to prior studies for [^{13}C,$^{15}N_2$]urea [53]. Briefly, the parameters were 14 x 7 cm FOV, 140 x 70 matrix size yielding 1 mm in-plane resolution for the coronal acquisitions, 11 ms TR, 770 ms temporal resolution, 15.4 s total scan time for 20 dynamic images, each acquired in projection mode. The parameters for TRAMP T_2 mapping were 3 x 3 cm FOV, 30 x 30 matrix size yielding 1 mm in-plane resolution for the coronal acquisitions, 11 ms TR, 330 ms temporal resolution, 6.6 s total scan time for 20 dynamic images. C_2-pyruvate T_2 maps were acquired with a coarser resolution due to SNR considerations, specifically a 14 x 7 cm FOV, 56 x 28 matrix size yielding 2.5 mm in-plane resolution (rat) or 8 x 4 cm FOV, 36 x 18 matrix size yielding ~2 mm in-plane resolution (TRAMP mouse) for the coronal acquisitions, while keeping the other parameters the same. The T_2 maps were reconstructed using a nonnegative least

squares algorithm with Tikhonov regularization as described in [27]. Briefly, pseudo-spectra were generated with the algorithm based on an input of 128 logarithmically-spaced T_2 values and an exponential decay model, and the long (>2 s) and short (<2 s) T_2 components [53] and associated amplitudes were found based on the peaks in the pseudo-spectra. An SNR cutoff based on the first time point was used to determine which pixels would be fit for each of the compounds: 30 for lactate in rat kidney, 15 for C_1-pyruvate in rat kidney, 20 for C_2-pyruvate in rat kidney, and 15 for all compounds in mouse tumor. As an example of the T_2 mapping acquisition, Figure 3.1 depicts the full dynamic set of images for acquisition of lactate in a rat (A) and mouse tumor (B). Associated bilinear (semilog plot) and biexponential decay for a single pixel in rat kidney, and linear (semilog plot) and monoexponential decay for a single pixel in mouse tumor are also provided.

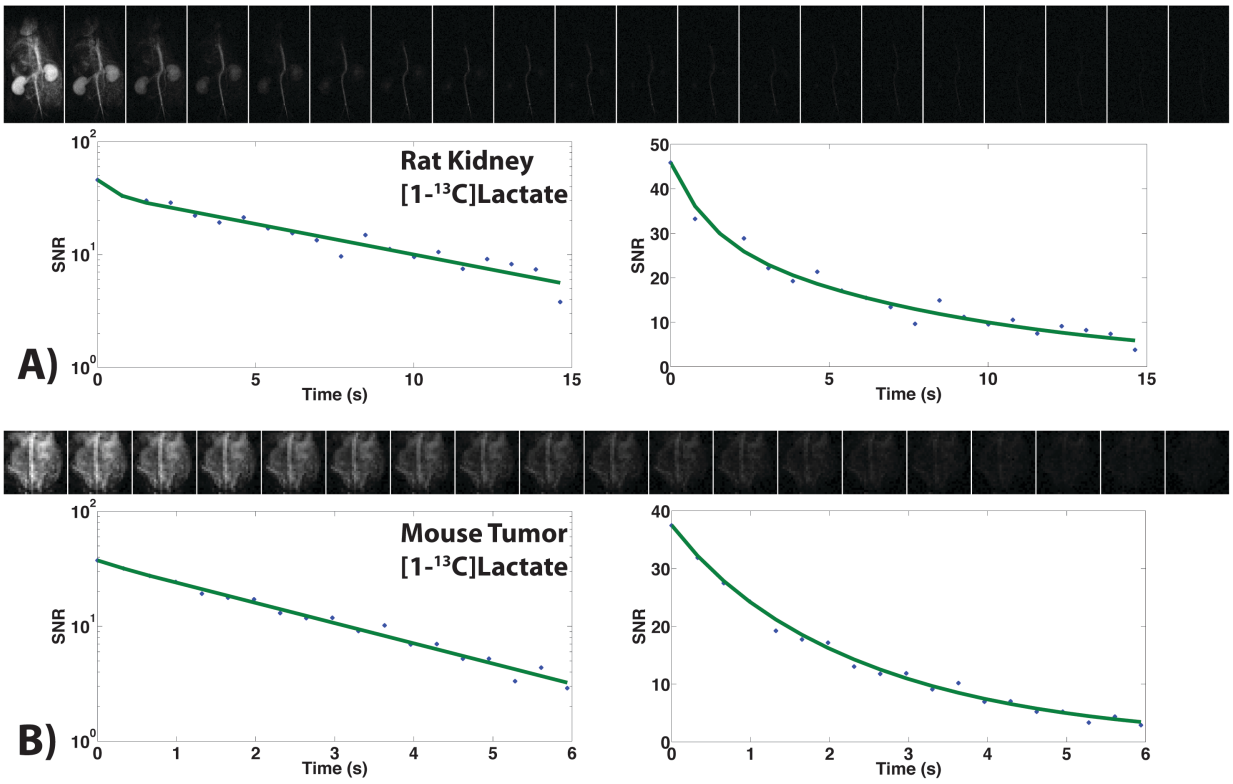

Figure 3.1: *Example of T_2 mapping acquisition and associated exponential decay with lactate.* ***A:*** *Full dynamic set of rat kidney images over the course of a T_2 mapping acquisition. A single pixel was chosen within the kidney that demonstrated a bilinear slope on the semilog plot on the left, which resulted in a biexponential decay, which can be seen in the plot on the right.* ***B:*** *Full dynamic set of mouse tumor images over the course of a T_2 mapping acquisition. A single pixel was chosen within the tumor that demonstrated a linear slope on the semilog plot on the left, which resulted in monoexponential decay, as shown in the plot on the right.*

Since the contribution of signal from metabolic products of lactate [91] and C_2-pyruvate [93] is negligible in comparison with the primary injected substrate, for the acquisitions as described, the measured T_2's should represent the true T_2's of these substrates. In the case of C_1-pyruvate, however, the measurements reflect an aggregate T_2 of C_1-pyruvate and its metabolic products lactate and alanine.

The 3D fully sampled rat acquisitions (Figure 3.5) had the following parameters: 12 x 6 x 2.4 cm^3 FOV extending throughout the heart and abdomen, 80 x 40 x 12 matrix size, yielding a 1.5 mm isotropic spatial resolution (0.003 cm^3), 8.5 ms/4.25 ms TR/TE

for a total scan time of ~4 s. A Cartesian raster encoding scheme was used, giving a ~2 s effective echo time. SNR was calculated in MATLAB by manually drawing ROIs in kidney and vasculature slices with the highest signal, as well as a region containing only noise. C_2-pyruvate 3D imaging in the rat was performed using partial Fourier encoding along one phase encoding dimension, acquiring only 5/6 of k-space, while keeping other parameters the same as previously mentioned. The data were reconstructed using a projection onto convex sets (POCS) reconstruction [94,95]. The 3D fully sampled mouse cancer model acquisitions (Figure 3.6) had the following parameters: 6.4 x 4.8 x 1.6 cm^3 FOV, 32 x 24x 8 matrix size, yielding a 2 mm isotropic spatial resolution (0.008 cm^3). An 8.5 ms TR for a total scan time of ~1.6 s was still used. The Cartesian raster encoding scheme gave a ~0.8 s effective echo time. The resulting carbon images were interpolated to 256 x 256 in-plane and either aligned with (rats) or overlaid onto (mice) proton images in multiple orientations using Osirix [96].

The TRAMP cancer model acquisition (Figure 3.7) was then modified to use compressed sensing for higher temporal resolution allowing for 3D high resolution dynamic imaging. A variable-density pattern, designed with a Monte-Carlo simulation [3] and shown in Figure 3.2A, was chosen to accelerate the acquisition two-fold with fully acquire k-space center, while maintaining the same 1.5 mm nominal spatial resolution. The parameters for each acquisition were 3 x 3 x 2.55 cm^3 FOV, 20 x 20 x 17 matrix size, 8.5 ms TR for a total acquisition time of ~1.4 s per dynamic time point. A 600 ms delay was used between successive time points, giving a total acquisition time of ~20 s for 10 dynamic 3D acquisitions. The resulting data was reconstructed using a ℓ_1-penalized nonlinear conjugate gradient algorithm with a Daubeches-4 wavelet transform

on each individual time point, similar to the reconstructions described in [3]. This algorithm was used to solve the following problem:

$$argmin_m \|F_u m - y\|_2 + \lambda \|\psi m\|_1 + \alpha TV_x(m) \qquad (3.1)$$

where *m* is the reconstructed MRI image, F_u is the undersampled Fourier Transform operator associated with the sampling pattern, y is the acquired data, ψ is the sparsifying transform, λ is the weight for ℓ_1-norm minimization, TV_x is the total variation (TV) penalty for the spatial dimensions, and α is the weight for the TV penalty. The λ and α parameters were chosen empirically to be 0.005 and 0.00005, respectively, via retrospective simulations of 50% undersampling of a previously acquired fully sampled dataset. Figure 3.2B depicts the results of the simulation with a comparison of a representative tumor slice. The reconstructed image matches the original image very closely based on the difference image, which was scaled up by a factor of 5 for visualization. The structural similarity index (SSIM) and normalized root mean squared error (NRMSE) were calculated to quantify these differences, which resulted in a SSIM value of 0.9255 and NRMSE of 7.00%, indicating the pattern design and undersampling factor were suitable for high resolution dynamic imaging.

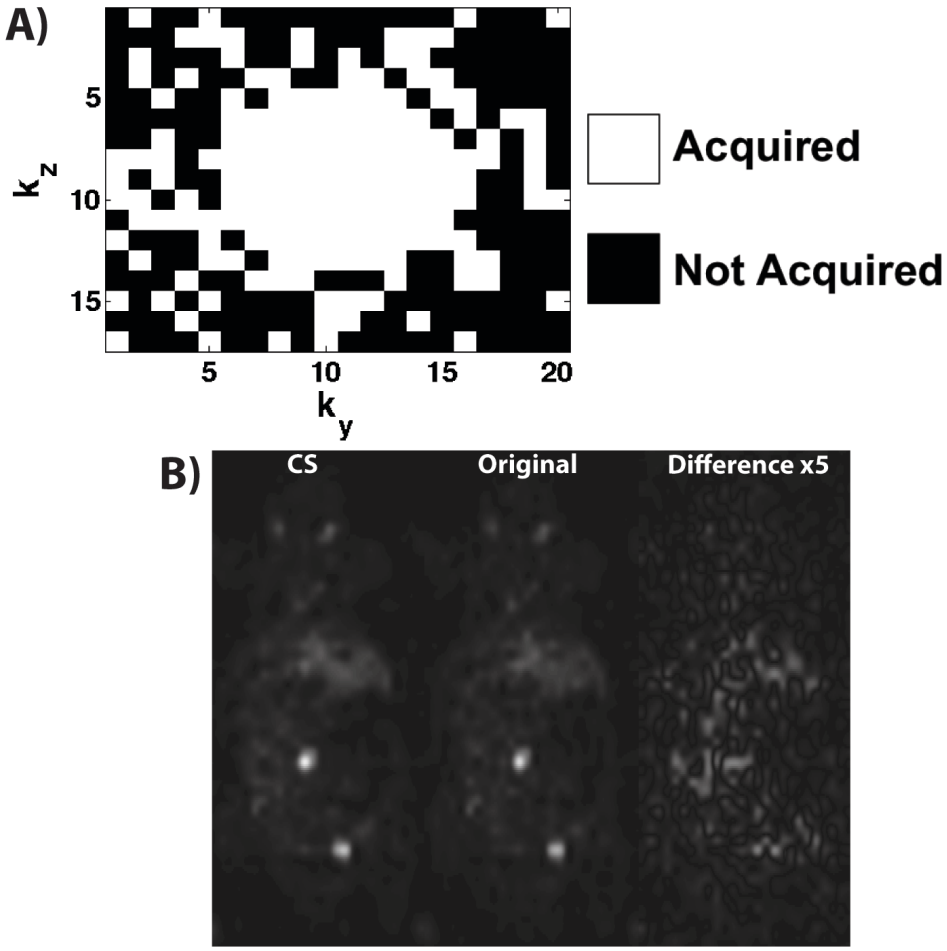

Figure 3.2: *Compressed sensing undersampling and retrospective simulations.* ***A:*** *A depiction of the variable-density pattern designed for dynamic imaging with compressed sensing. The pattern was designed using a Monte-Carlo simulation, as described previously in* [3]*, such that only 50% of the phase encodes were acquired, and the center of k-space was fully sampled.* ***B:*** *A single slice comparison from a full 3D retrospective simulation of lactate in a TRAMP mouse with 50% undersampling. The reconstructed image agrees well with the original image as shown in the 5-fold amplified difference image, as well as having a SSIM of 0.9255 and a RMSE of 7.00%. The images have been zero-filled from 26 x 20 (matrix size in pattern shown in part a) to 256 x 256 for display purposes.*

3.4 Results

3.4.1 T_2 Mapping

The mean T_2 distribution of lactate, C_1-pyruvate, and C_2-pyruvate can be seen in both Figure 3.3A and Table 3.1, where a decrease in T_2 was observed from the vasculature to the renal cortex. The longest mean T_2 values of lactate, at ~2.6 s, were

measured in the vasculature, with a decrease to ~1.95 s in the kidneys. Decreasing values were observed from the renal pelvis to the renal cortex. A similar trend was observed with C_1-pyruvate, albeit with about 30% lower values as compared to lactate, and C_2-pyruvate, with a mean T_2 value of ~0.75 s in both vasculature and kidney. Figure 3.3B and 3.3C show the long and short T_2 components, respectively, of each compound. The short T_2 component was evident in both vasculature and kidney among all compounds, while lactate showed considerable long components, especially in the vasculature. Previously acquired T_2 maps of urea show a similar distribution within the kidney [53], and the results presented here are relatively similar to the results of previous T_2 measurements of these ^{13}C compounds [44,97]. Though the lactate and C_1-pyruvate experiments yielded T_2 values of approximately half those of urea [53], these values were still long enough to be exploited effectively for high resolution imaging since the T_1 and T_2 were either longer or on the order of the effective echo time of the subsequent 3D experiments, allowing for acquisition of high k-space signal with rasterized phase encoding and insignificant T_2 blurring [23].

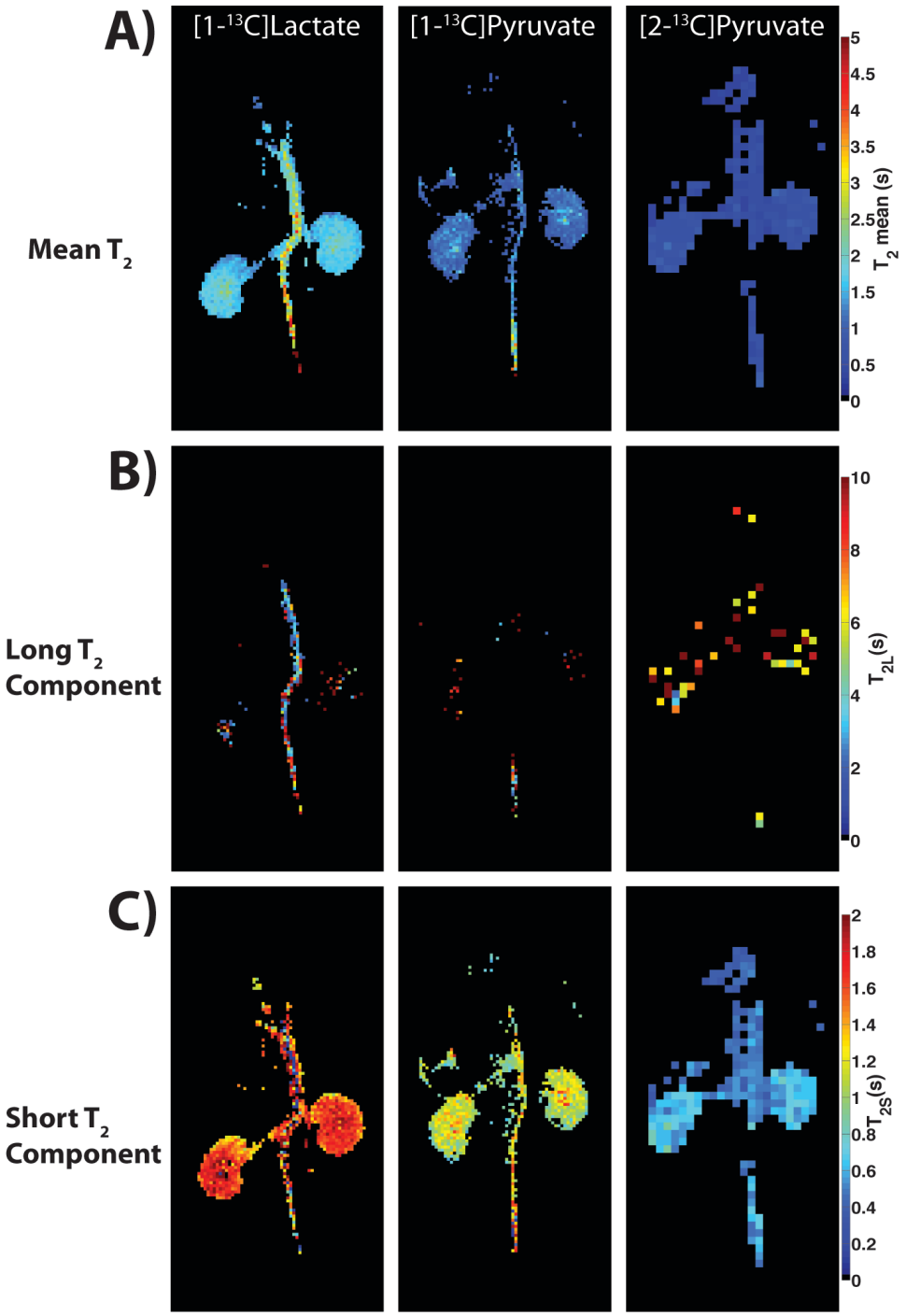

Figure 3.3: *T_2 mapping of normal rat kidneys and vasculature after injection of lactate, C_1-pyruvate, and C_2-pyruvate.* ***A:*** *The mean T_2 values (logarithmic mean of long and short components* [27]*) of each compound indicate lactate having the longest T_2 values among the three compounds with C_2-pyruvate having the lowest values. Each compound does exhibit the same trend of a T_2 decrease from the vasculature to the renal pelvis to the medulla, and ending with the cortex.* ***B:*** *The long (>2 s) T_2 components for each compound.* ***C:*** *The short (<2 s) T_2 components for each*

compound. The T_2 maps of C_1-pyruvate represent an aggregate T_2 of signals C_1-pyruvate and associated metabolic products. The images are displayed at 1 x 1 mm^2 for lactate and C_1-pyruvate, and 2.5 x 2.5 mm^2 for C_2-pyruvate.

	Lactate	C_1-Pyruvate	C_2-Pyruvate
Renal Pelvis	2.21±0.39 s	1.36±0.09 s	
Medulla	1.95±0.24 s	1.26±0.17 s	0.73±0.07 s
Renal Cortex	1.70±0.14 s	1.16±0.14 s	
Vasculature	2.58±0.33 s	1.38±0.08 s	0.75±0.19 s
R^2	0.938	0.943	0.877

Table 3.1: *Anatomical Distribution of Mean T_2 within Rat Kidney and Vasculature. The mean T_2 values (mean and standard deviation of all three rats) and associated standard deviations within different regions of the rat kidney and vasculature for all three compounds are presented here and demonstrate the longest T_2 values exist in the vasculature, while within the kidney there is a decrease from the renal pelvis to the medulla to the renal cortex, with all components long enough to exploit in 3D imaging. The resolution of the C_2-pyruvate T_2 mapping was not high enough to distinguish the different regions of the kidneys. Mean R^2 values of depicted pixels in Figure 3.3 are presented here, with black pixels excluded from calculation.*

Within the TRAMP tumor, the mean T_2 measurements (Figure 3.4) for lactate, C_1-pyruvate, and urea ranged from ~1.8-2.5 s, while C_2-pyruvate was ~0.3 s, similar to previous studies [44,97]. The tumors had some T_2 variability with the intra-tumor standard deviation equaling ~10-20% of the mean value due to the inherent spatial heterogeneity in these tumors. Similar to the T_2 mapping for rat kidneys and vasculature, the T_2 values were still long enough to be utilized for high spatial resolution imaging for both single time point and serial dynamic imaging with the bSSFP sequence. The effective echo times were also relatively short compared to T_1 and T_2 due to the fewer phase encodes acquired for single time point (smaller FOV compared to rat) and serial dynamic imaging (smaller FOV and undersampling).

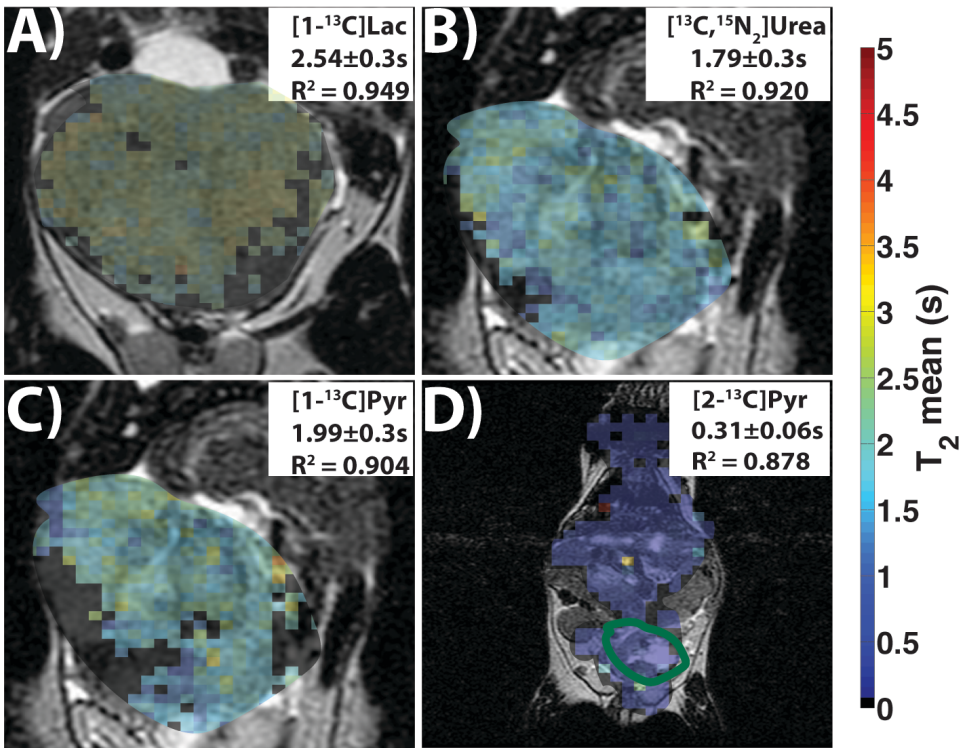

Figure 3.4: *Measured T_2 value maps from a transgenic prostate tumor overlaid on top of the ^1H image after injection of lactate (A), urea (B), C_1-pyruvate (C), and C_2-pyruvate (D). The tumor in panel D is outlined in green. Mean R^2 value of the depicted pixels is also displayed, with black pixels excluded from the calculation. The images are displayed at 1 x 1 mm^2 for urea, lactate and C_1-pyruvate, and 2 x 2 mm^2 for C_2-pyruvate.*

3.4.2 Fully Sampled 3D Rat and Mouse Cancer Model Imaging

Figure 3.5 shows the resulting 3D images in rats of lactate, C_1-pyruvate, and C_2-pyruvate. Uptake and biodistribution of these compounds can be seen within the kidney, with the image resolution being sufficient to visualize the renal pelvis and cortex of the kidney, as well as the connecting vasculature components. Figure 3.5A features all 12 slices corresponding to the 3D lactate acquisition, with the SNR being high enough to also visualize signal in the heart. Figure 3.5B features representative slices of lactate and C_1-pyruvate next to the corresponding ^1H image, as well as the reformatted axial slices, owing to the 3D isotropic nature of the acquisition. Figure 3.5C shows a

representative C_2-pyruvate slice overlaid onto the corresponding ^{1}H image. The SNR trend between these three compounds followed the mean T_2 trend discussed previously. However, the SNR of C_2-pyruvate was still high enough at 1.5 mm isotropic resolution to see uptake in the vasculature and kidneys. The resulting SNR within different parts of the rat kidney, as well as the vasculature, is presented in Table 3.2.

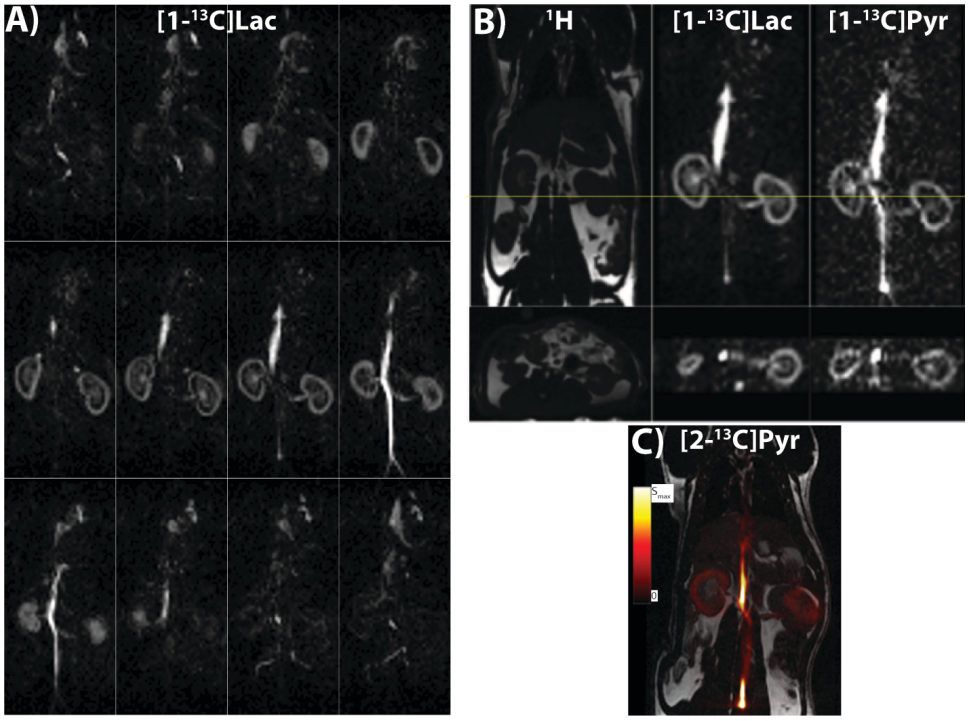

Figure 3.5: *High resolution 3D 1.5 mm isotropic imaging of lactate, C_1-pyruvate, and C_2-pyruvate.* ***A:*** *All 12 slices in a 3D lactate acquisition are shown here. Uptake of lactate can be seen within the kidneys, vasculature, and the heart.* ***B:*** *A representative coronal and axial slice (B) from the 3D lactate and C_1-pyruvate acquisitions are shown next to an anatomical ^{1}H image. The coronal and axial reformats (yellow line indicates axial slice position) show hyperintense signal from the vasculature and renal pelvis. The lactate acquisition exhibited higher SNR compared to the C_1-pyruvate.* ***C:*** *A representative coronal slice from a 3D C_2-pyruvate acquisition overlaid atop the anatomical ^{1}H image. The C_2-pyruvate acquisition had considerably less SNR compared to lactate or C_1-pyruvate, but uptake within the vasculature and kidneys is still visible. The images were zero-filled to 256 x 256 for display purposes.*

	Lactate	C_1-Pyruvate	C_2-Pyruvate
Renal Pelvis	56.7±9.1	31.3±15.9	
Medulla	28.8±6.1	15.7±6.1	10.2±5.2
Renal Cortex	53.1±14.4	25.4±8.3	
Vasculature	129±19.8	96.5±14.9	34.5±17.8

Table 3.2: *Anatomical Distribution of SNR within Rat Kidney and Vasculature. The mean SNR values and associated standard deviation within different regions of the rat kidney and vasculature for all three compounds are presented here. The highest SNR values were seen in the vasculature, while within the kidney there is a decrease from the renal pelvis to the renal cortex to the medulla. The SNR was high enough, however, to distinguish these regions for lactate and C_1-pyruvate, and visualize overall kidney biodistribution for C_2-pyruvate.*

Similarly, the 3D images of the TRAMP and breast cancer mice in Figure 3.6 overlaid on top of the ^{1}H images, show uptake of C_1-pyruvate within the kidneys and the tumor. While the mouse anatomy is smaller, the resolution here was also sufficient to image the distribution of C_1-pyruvate within vasculature, renal pelvis and cortex, and tumor. With the effective echo time being only ~2 s for rat acquisitions and ~1.4 s for mice acquisitions, the long T_2 values of these molecular probes enabled sufficient SNR with the bSSFP sequence to obtain 1.5 mm and 2 mm isotropic resolution, respectively, for the depiction of these anatomical structures.

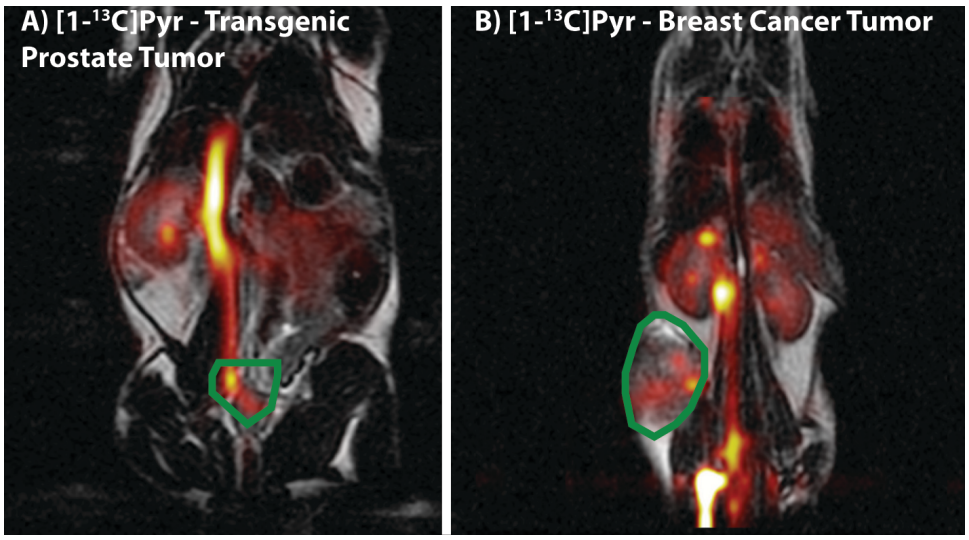

Figure 3.6: *3D images overlaid on ^{1}H anatomical images of C_1-pyruvate in transgenic prostate tumor (A) and breast cancer mouse (B). The blue ROIs indicate tumor region. Uptake of C_1-pyruvate can be seen in vasculature, kidneys, and tumor, with resolution high enough to see uptake in the renal cortex and renal pelvis, which is similar as rat kidney imaging. The images were zero-filled from 32 x 24 (2 x 2 mm^2 in-plane resolution) to 256 x 256 for display purposes.*

3.4.3 Compressed Sensing TRAMP Imaging

The 2x fold acceleration via compressed sensing was shown to successfully acquire dynamic data of hyperpolarized C_1- and C_2-pyruvate, lactate, and urea while improving the spatial resolution utilized in the previously shown fully sampled data by 25% in each spatial dimension. There was no observed SNR loss with the compressed sensing acquisition even with a higher spatial resolution as evidenced by 2x fold SNR difference between the first dynamic time point and the fully sampled acquisition (~40 vs. ~20) of C_1-pyruvate. The first five time-points of the 3D dynamic acquisition from a representative kidney and tumor slice are shown in Figure 3.7A-C, with C_2-pyruvate carbon images overlaid on top of ^{1}H images in 3.7D (tumor) and 3.7E (tumor). With the 1.5 mm isotropic resolution, uptake and distribution of all three compounds within kidneys, vasculature, and tumor was seen, similar to the fully sampled images above.

Furthermore, the differences in the dynamics of each compound correlated with the mean T_2 values mentioned previously, whereby C_2-pyruvate quickly decayed due to both relaxation and metabolism, while lactate and urea persisted longer, especially in the kidney, owing to the long T_2 values mentioned here and measured previously. While not shown here, injection of C_1-pyruvate instead of C_2-pyruvate yielded similar results as with C_2-pyruvate, albeit the dynamic signal lasted slightly longer due to the longer T_1 and mean T_2 value.

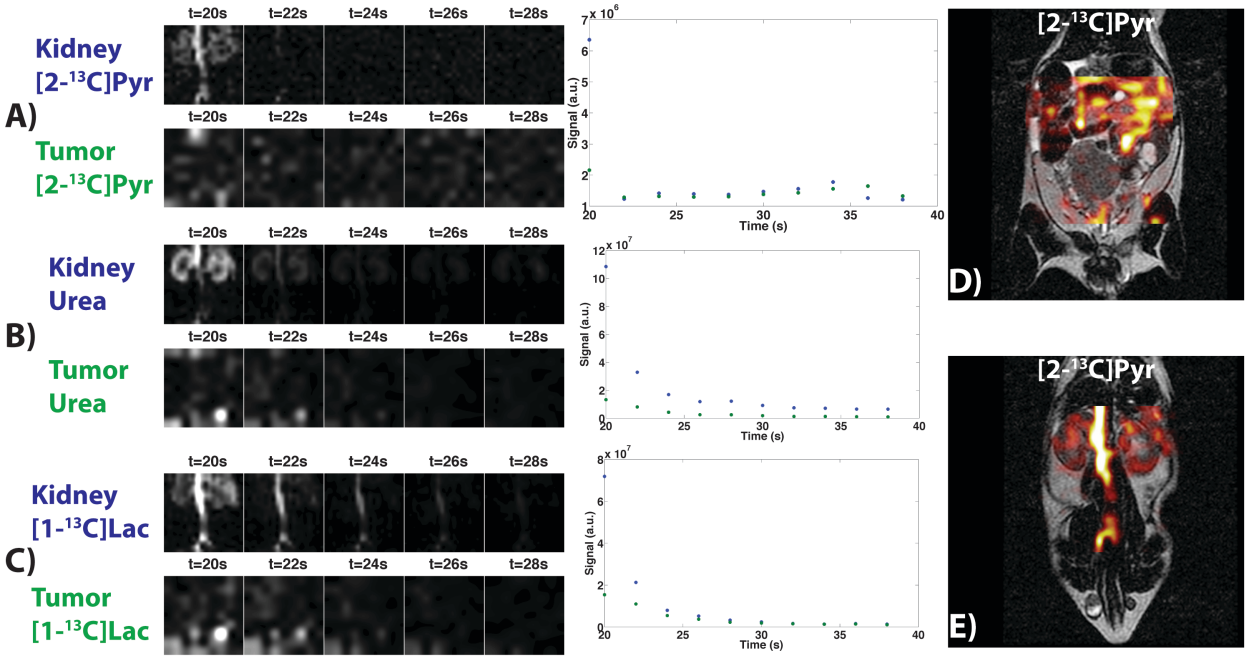

Figure 3.7: *Dynamic imaging of a transgenic prostate tumor with C_2-pyruvate, urea, and lactate.* ***A-C:*** *First five time-points of a representative kidney and tumor slice from the 3D dynamic imaging of C_2-pyruvate (A), urea (B) and lactate (C) are shown here, with associated decay curves for each slice.* ***D and E:*** *Carbon images within the tumor (and surrounding tissue) (D) and kidneys (E) overlaid on the anatomic ^{1}H image are also presented. The kidney slice has strong uptake of all three compounds, while the tumor shows varied uptake, with a clear distinction in decay curves between the healthy kidney tissue and diseased tumor tissue. The images were zero-filled to 256 x 256 for display purposes.*

3.5 Discussion

The results of this study demonstrated the feasibility and capability of 1.5 mm isotropic resolution hyperpolarized carbon-13 imaging on a 3T clinical scanner with the bSSFP sequence. Metabolically important compounds, such as pyruvate and lactate, as well as a perfusion agent, urea, were imaged at high enough spatial resolution to determine distribution, uptake, and structural morphology within specific anatomical features, such as different kidney compartments and inhomogeneity within tumors. 1 mm in-plane T_2 maps were also generated, showing the existence of long and short components for the different compounds, both corroborating previous studies on the in vivo carbon-13 T_2's, as well as providing a better anatomical distribution of the T_2's. The feasibility of using compressed sensing in conjunction with the bSSFP sequence was demonstrated for improved temporal resolution without sacrificing spatial resolution, which may be useful for translating this approach for clinical imaging, as larger volume coverage (larger matrix sizes) will necessitate increased sequence acceleration.

The T_2 values of pyruvate (C_1 and C_2) and lactate identified within rat kidneys and vasculature can be explained based on the relaxation mechanisms associated with ^{13}C labeled compounds such as chemical shift anisotropy and the dipolar relaxation [53,98,99]. The relative contribution of each of these pathways remains unknown in vivo, as is the net contribution from intra- and intermolecular relaxation pathways and relaxation from transport between differing microenvironments. Furthermore, T_1 and inflow can have an effect on T_2 calculation, as described previously [53].

With C_1-pyruvate and lactate exhibiting >~1 s short and long components, this may indicate relatively free rotation and diffusion within both vasculature and kidneys,

leading to shorter rotational correlation times and longer T_2 values. The presence of monocarboxylate transporters (MCTs) in red blood cells indicate each compound can be transported into and out of the cells [100–102] and would subsequently not be hindered in free movement about the vasculature or within different kidney compartments [103]. Furthermore, paramagnetic effects arising from certain oxidation states of hemoglobin may also have a significant relaxation effect on molecules that are transported into RBCs. The longer T_2 values within the renal pelvis compared to the renal cortex and medulla can potentially be attributed to the presence of glomerular filtrate, which is free from red blood cells [53], leading to a longer solution-like T_2. There is lower lactate dehydrogenase (LDH) activity in both renal pelvis and vasculature as well [104], leading to less metabolic conversion to shorter T_2 compounds, and a higher calculated T_2. This reasoning can also be applied to explain the differences in T_2 between each of the compounds, with lactate less readily back-converted to pyruvate via LDH and thus having the longest measured T_2, while conversely C_2-pyruvate is more readily converted to either C_2-lactate or other compounds in the citric acid cycle, which leads to a shorter measured T_2 due to the contributions of these shorter T_2 compounds, with C_1-pyruvate being somewhere in the middle. Furthermore, C_2-pyruvate has a much shorter initial relaxation time because of the dipolar relaxation term since a proton is one bond closer to the ^{13}C of the compound compared to C_1-pyruvate and lactate. This point was corroborated by performing a T_2 measurement on hyperpolarized aqueous C_1- and C_2-pyruvate via a CPMG sequence with a TR of 10 ms. The measured T_2 of C_2-pyruvate (21 ± 2.9 s) was ~84% of C_1-pyruvate (25 ± 0.7 s), indicating the effect of dipolar relaxation. The role of dipolar and chemical shift

anisotropy relaxation, as well as potential paramagnetic relaxation [99] in the vicinity of hemoglobin, needs to be studied further to get a full understanding of the in vivo T_2 distribution, specifically the relaxation properties of each compound, such as, for example, the enhanced role of the dipolar relaxation in the conversion of C_2-pyruvate to C_2-lactate, as well as the potential differences when the compounds are intracellular versus extracellular. Further progress in the development of long-lived hyperpolarized ^{13}C probes, such as the chemical design of the probes and extension of hyperpolarized lifetimes, can help identify the relaxation mechanisms governing a compound's in vivo T_1 and T_2 [105,106].

The 3D high resolution imaging of the rat kidney agreed with the T_2 mapping, with the highest SNR being within the vasculature and renal pelvis, and lactate having the highest SNR and C_2-pyruvate having the lowest. Additionally, SNR was sufficient at 1.5 mm isotropic resolution from the heart to visualize uptake of lactate and pyruvate. Within the kidney, the biodistribution of each compound correlated with previous metabolic studies, with an infusion of either pyruvate or lactate resulting in stronger signal from the cortex and renal pelvis compared to the medulla [103,107]. In normal kidney function, especially after infusion, both lactate and pyruvate are readily metabolized, with reduction of pyruvate to lactate and oxidation of lactate to pyruvate, as well as conversion of lactate to glucose via gluconeogenesis and conversion to amino acids. Lactate and pyruvate can also be reabsorbed by the proximal tubule. These processes occur primarily in the cortex, correlating with the uptake and biodistribution seen in the 3D imaging.

Compared to the rat kidneys, the T_2 distribution and subsequent 3D imaging of the TRAMP tumors was more varied in terms of uptake and biodistribution, a consequence of tumor heterogeneity [108]. The relaxation mechanisms previously discussed can also be applied within the tumor environment, including the role of metabolism, since LDH activity is relatively much higher within tumors compared to normal tissue, and vascularity, with the presence of leaky blood vessels allowing for relatively free rotation and shorter rotational correlation times [44,83]. Exchange between intracellular and extracellular pools within the tumor can cause T_2 shortening, potentially due to short T_2 components coming from the intracellular pool [109]. While C_2-pyruvate clearly had the shortest mean T_2 value, the other three compounds all had similar T_2 values, and all four compounds had moderate intratumoral standard deviations, potentially indicating some spatial heterogeneity within the TRAMP tumors, which was similarly seen with injected [1-^{13}C]pyruvate in an earlier study [110]. This can be attributed to the presence of microenvironments and several competing mechanisms that affect the infused compounds, such as MCT and LDH activity, lactate shuttling, reverse Warburg effect, and tumor hypoxia [90,111,112]. These effects also extend to the 3D dynamic imaging, whereby the spatial biodistribution of the compounds, and consequent signal decay, can be attributed to the different mechanisms governing metabolism and perfusion within the tumor.

The use of C_2-pyruvate in this study is potentially useful for looking at tumor metabolism with the bSSFP sequence without sacrificing the SNR and spatial resolution advantages. Previously, C_2-pyruvate has been extensively used to study the Krebs cycle, especially within the context of cardiac metabolism [43,113,114]. While the C_1-

pyruvate T_2 mapping and 3D imaging in this study include significant contributions from its metabolites lactate, alanine, and pyruvate-hydrate due to the close resonances of all these compounds at 3 Tesla (not an issue after injection of [1-^{13}C]lactate due to much smaller metabolic conversion [91]), the C_2 labeled versions of these metabolites arising from the metabolic conversion of C_2-pyruvate resonate 100+ ppm away from C_2-pyruvate [115]. Therefore, with the 1.6 ms sinc RF pulse (excitation bandwidth of 2500 Hz) used in this study, the signal arising from any C_2-metabolites are negligible compared to the C_2-pyruvate, and the resulting images (in the case of rat kidney) and signal decay (in the case of TRAMP tumors) reflect more accurately the effects on C_2-pyruvate in the specific microenvironment.

In general, single metabolite imaging of hyperpolarized ^{13}C compounds can provide a high resolution view of the biodistribution and uptake of said compounds in a very fast and efficient manner. When dealing with a single frequency system, as is the case for C_2-pyruvate, [^{13}C,$^{15}N_2$]urea, and C_1-lactate in this study, pulse design becomes much easier and much shorter TRs are achievable, allowing for high resolution imaging, as was demonstrated in this study. Urea, as a metabolically-inactive compound, can provide perfusion information and thus has a direct application as a single injected hyperpolarized compound. However, metabolically active compounds, such as C_2-pyruvate and C_1-lactate, can provide additional information due to their cellular uptake and metabolism. The utility in imaging these single metabolites after injection may be similar to the information obtained from positron emission tomography (PET) imaging, such as standard uptake values or fitting the dynamics to a pharmokinetic model. Compared to PET, hyperpolarized ^{13}C imaging can be much faster and without radiation

exposure, while still reporting on uptake of metabolically active compounds [31]. In addition, hyperpolarized ^{13}C has advantages over other perfusion MRI techniques, such as gadolinium-based approaches and arterial spin labeling, including signal to tracer concentration proportionality, high SNR and CNR, no gadolinium toxicity issues, and the capability of simultaneously injecting multiple probes [51,52,116].

Imaging of C_1-pyruvate and/or the resulting C_1 metabolites with the bSSFP sequence would necessitate either the use of suppression pulses, which can be challenging with such close resonances at 3 Tesla, or long excitation/refocusing pulses, which would offset some of the advantages of the bSSFP sequence. Recently, C_1-pyruvate and produced C_1-lactate were imaged on a 14T system using a specially designed multiband spectrally selective pulse and an appropriate choice of TR [28]. This approach could, in principle, be applied on a 3T clinical scanner, although trade-offs would need to be made between spatial and temporal resolution.

The ability to obtain 3D 1.5 mm isotropic images for ^{13}C can be very advantageous for assessment of disease within specific organs, especially at the clinically relevant field strength of 3 Tesla. Current acceptable parameters for proton imaging of prostate cancer features slice thicknesses of ~3 mm and in-plane resolution of ≤2 mm for various acquisitions, such as dynamic contrast enhanced MRI [117–119]. Furthermore, 3D isotropic imaging is most desirable due to the ability to limit patient scanning, while simultaneously acquiring all the desired information in all three planes [120]. Recently, work by Nielsen et al. [57] and Bertelsen et al. [121] demonstrated 1.25 mm isotropic resolution imaging of [^{13}C,$^{15}N_2$]urea with a 3D bSSFP sequence in rat kidneys on a 9.4T preclinical scanner with higher performance gradients enabling

shorter achievable TRs. This allowed high spatial resolutions to be achieved. By comparison, our initial rat kidney results featured slightly lower 1.5 mm isotropic resolution, but utilized clinical gradient strengths and shorter T_2 compounds. Nevertheless, both sets of results demonstrate the feasibility of obtaining approximately 1 mm isotropic resolution for hyperpolarized ^{13}C compounds, especially on 3T clinical scanners, as was recently demonstrated in [27]. Recent work on [^{13}C,$^{15}N_2$]urea imaging on pigs at 3T [58] shows feasibility of imaging larger animals, although at a considerably coarser spatial resolution.

The sequence presented here could potentially be further optimized for improved dynamic imaging by employing both newer undersampling reconstruction strategies, such as a wavelet along time or low rank plus sparse approach [5,19]. A variable flip angle scheme can be implemented for each desired metabolite using a non-convex optimization approach that would increase SNR, reduce image blurring, and improve off-resonance insensitivity for single time-point images, or maximize SNR for high resolution dynamic imaging [122]. The bSSFP sequence and these specific acquisition and reconstruction approaches can also be readily combined with parallel imaging [7,15], which may be required as the translation from preclinical to clinical imaging will require larger matrix sizes for the same desired isotropic resolution.

3.6 Conclusion

In this study we performed high resolution HP ^{13}C imaging using the bSSFP sequence. T_2 mapping was performed on rat kidneys and vasculature, as well as tumor-bearing mice, using [1-^{13}C]pyruvate, [1-^{13}C]lactate, [2-^{13}C]pyruvate, and [^{13}C,$^{15}N_2$]urea.

We tailored the bSSFP acquisition to the measured T_2's to obtain 1.5 mm isotropic single time-point images of biodistribution within rat kidneys and vasculature in only ~4 s. Using 2-fold compressed sensing acceleration, we extended the high resolution single-time-point imaging framework to dynamic imaging without having to sacrifice spatial resolution, enabling us to obtain biodistribution data at 1.5 mm isotropic resolution every 2 s. The HP ^{13}C methods presented here can be utilized for high resolution dynamic imaging of metabolism, biodistribution, and perfusion.

Chapter 4: Using a Local Low Rank plus Sparse Reconstruction to Accelerate Dynamic Hyperpolarized ^{13}C Imaging using the bSSFP Sequence

4.1 Abstract

Acceleration of dynamic 2D (T_2 Mapping) and 3D hyperpolarized ^{13}C MRI acquisitions using the balanced steady-state free precession sequence was achieved with a specialized reconstruction method, based on the combination of low rank plus sparse and local low rank reconstructions. Methods were validated using both retrospectively and prospectively undersampled in vivo data from normal rats and tumor-bearing mice. Four-fold acceleration of 1-2 mm isotropic 3D dynamic acquisitions with 2-5 s temporal resolution and two-fold acceleration of 0.25-1 mm^2 2D dynamic acquisitions was achieved. This enabled visualization of the biodistribution of [2-^{13}C]pyruvate, [1-^{13}C]lactate, [^{13}C,$^{15}N_2$]urea, and HP001 within heart, kidneys, vasculature, and tumor, as well as calculation of high resolution T_2 maps.

4.2 Introduction

The advent of dissolution dynamic nuclear polarization (dDNP) of ^{13}C substrates [33], in conjunction with magnetic resonance imaging (MRI), has provided a new approach for studying the metabolic and physiological changes associated with various diseases, including cancer and diabetes, among several other examples [31,50,67,81,121,123]. Recent successful phase I and phase II clinical trials have

demonstrated how dynamic imaging of ^{13}C substrates can provide several quantifiable biomarkers of disease [59–64]. A key tradeoff in the design of dynamic hyperpolarized ^{13}C (HP ^{13}C) imaging strategies is the balance between spatial and temporal resolution due to the limited lifetime of the hyperpolarized magnetization, which is consistently depleted due to T_1 and T_2 decay, metabolism, and application of RF pulses. This tradeoff can lead to poor image quality (i.e. with large partial volume effects) and associated difficulties in model fitting of the dynamics. Balanced steady-state free precession (bSSFP) supports high resolution acquisition by exploiting the long T_2's of ^{13}C substrates, but may be especially affected by early depletion of the HP magnetization due to the high number of RF pulses required to achieve high resolution volume imaging [28,66]. While bSSFP does provide the highest SNR per unit time [21] and has been used for 2D HP ^{13}C T_2 mapping and 3D single time-point acquisitions [27,53,66], it has not been applied to 3D dynamic HP ^{13}C acquisitions because of the aforementioned tradeoff in spatial and temporal resolution.

Compressed sensing has been increasingly applied for accelerating MRI by exploiting data sparsity in an appropriate domain [3,4,6,124,125]. Alternatively, global low rank and local low rank matrix completion has also been utilized in reconstruction of undersampled dynamic MRI data by exploiting the spatiotemporal correlations that exist within different tissues [10–12,126]. Both approaches have been well documented in proton imaging and have been extended to hyperpolarized ^{13}C imaging to improve both spatial and temporal resolution [5,127–129]. Recently, Otazo et al. [19] showed the advantage of combining these methods into a low rank plus sparse (L+S) reconstruction in order to increase imaging speed in dynamic proton imaging since the L+S model

offered higher compressibility compared to either method alone. Perfusion imaging in particular features local low rank properties that lead to improved reconstructions, since neighboring tissues have similar spatiotemporal dynamics, and these properties have been successfully exploited in initial proton perfusion imaging studies [13,130]. Likewise, combining the L+S model and the local low rank method into a local low rank plus sparse (LLR+S) model also has the potential to improve reconstruction of dynamic imaging of the biodistribution of HP ^{13}C probes (i.e. for HP ^{13}C perfusion imaging).

The goal of this study was to accelerate both 2D and 3D T_2 mapping and 3D dynamic high resolution imaging with the bSSFP sequence using a LLR+S algorithm. In-plane resolutions of <1 mm were achieved for 2D T_2 mapping of multiple HP ^{13}C compounds, with 3D 1 mm isotropic T_2 map demonstrated as well. Furthermore, 3D 1.5-2 mm isotropic imaging with 2-5 s temporal resolution was achieved in both healthy rats and tumor-bearing mice. Biodistribution of [2-^{13}C]pyruvate, [1-^{13}C]lactate, and [^{13}C,$^{15}N_2$]urea was visualized within kidneys, vasculature, heart, and tumor.

4.3 Theory

Otazo et al. [19] provided a formal treatment on the L+S decomposition and how it can be applied to ^{1}H acquisitions. Dynamic ^{1}H MRI can be separated into a low rank component representing the static background and a sparse component representing the rapid changing dynamics. HP ^{13}C MRI, however, lacks a background signal due to the low signal of any natural abundance ^{13}C, and all signal inherently rapidly decays away towards thermal equilibrium. Therefore, HP ^{13}C acquisitions cannot truly be represented by a separation of a static background and rapidly changing dynamics

since there is no incoherence between the low rank and sparse components. However, as previously mentioned, if only L+S is of interest, as is the case here, then this algorithm still outperforms a low rank or sparse only reconstruction.

The LLR+S matrix decomposition can be formulated as [19]:

$$\min_{L,S} \frac{1}{2}\|E(L+S)-d\|_2^2 + \lambda_L \sum_{i=1}^{N_b}\|B_i L\|_* + \lambda_S \|TS\|_1 \qquad (4.1)$$

where L and S are the outputted decomposed low rank and sparse matrices, respectively, E is the encoding operator that performs a spatial partial FT for each time-point, d is the undersampled k-t data, B_i is an operator that selects an image block ***b*** and transforms it into a spatiotemporal matrix (assuming the spatiotemporal image data can be divided into N_b image blocks), T is the sparsifying transform for S, and λ_L and λ_S act as tuning parameters controlling the contribution of the L_1-norm and nuclear norm terms.

The optimization problem in equation 1 was solved using iterative soft thresholding as described in Otazo et al. [19], with slight modifications to account for the local low rank approach. Briefly, for each iteration k, given the matrix M = L+S, a soft thresholding operator, defined as

$$\Lambda_\lambda(x) = \frac{x}{|x|}\max(|x| - \lambda, 0), \qquad (4.2)$$

was applied to the singular values of $M_{k-1} - S_{k-1}$ and the sparse transform coefficients of $M_{k-1} - L_{k-1}$ to calculate L_k and S_k, respectively, leading to a calculation of a new M_k by enforcing data consistency. The algorithm iterated until the relative change in the solution was less than a certain tolerance limit, which depended on the specific acquisition employed. The first ten iterations were performed using the singular value decomposition (SVD) of the full spatiotemporal matrix (Global Low Rank or GLR), while

subsequent iterations utilize the SVD of the individual image blocks (local low rank or LLR). Furthermore, a cooling method was used to converge as described previously [11]. The size of the image blocks (bsize) was defined for each dataset based on the acquired matrix size. Table 4.1 summarizes the proposed LLR+S algorithm using pseudo-code.

Inputs: y: undersampled k-t data
E: partial spatial Fourier transform operator based on undersampling mask
T: sparsifying transform
λ_L: singular value threshold
λ_S: sparsity threshold
b: image block in Ω for local low rank soft thresholding
Tol: relative change of solution

Outputs: L,S: solutions to Equation 1; low rank and sparse components of reconstructed data

Algorithm: $M_0 = E^* y,\ S_0 = 0$ %Initialize data
do {
% Singular Value Soft Thresholding
$L_k = \cup_{b\in\Omega} SVT_{\lambda_L}(C_b(M_{k-1} - S_{k-1}))$
% Soft Thresholding in T domain
$S_k = T^{-1}(\Lambda_{\lambda_S}(T(M_{k-1} - L_{k-1})))$
% Data consistency: subtract residual
$M_k = L_k + S_k - E^*(E(L_k + S_k) - y)$
$err = \frac{\|L_k+S_k-(L_{k-1}+S_{k-1})\|_2}{\|L_{k-1}+S_{k-1}\|_2}$
} while err>Tol

Soft Thresholding Operator: $\Lambda_\lambda(x) = \frac{x}{|x|}\max(|x| - \lambda, 0)$
Singular Value Thresholding (SVT) Operator: $SVT_\lambda(M) = U\Lambda_\lambda(\Sigma)V, where\ [U,\Sigma,V] = SVD(M)$

Table 4.1: *Pseudo-code for LLR+S reconstruction algorithm.*

4.4 Methods

4.4.1 Animal Handling

All animal studies were done under protocols approved by the University of California San Francisco Institutional Animal Care and Use Committee (IACUC). Normal Sprague-Dawley rats and transgenic adenocarcinoma of mouse prostate (TRAMP) mice [42] were used in these studies. Isoflurane (1.5%) was used to anesthetize the animals, which were then placed in a supine position on a heated pad throughout the duration of the experiments. After polarization and dissolution, each of the compounds were injected into the animal via tail vein catheters: ~3 mL over 12 s for each rat and ~500 μL over 15 s for the mouse.

4.4.2 Hardware and Hyperpolarization

All experiments were performed on a 3T GE MR750 clinical scanner (GE Healthcare, Waukesha, WI) with multinuclear capability. Dual-tuned $^{1}H/^{13}C$ transceiver volume radiofrequency coils were used that had either an inner diameter of 8 cm for rats or an inner diameter of 5 cm for mice.

Stock solutions of all compounds used in this study ([2-^{13}C]pyruvate, [1-^{13}C]lactate, [^{13}C,$^{15}N_2$]urea, HP001) were prepared as described previously [54,66]. Each compound was individually polarized in a HyperSense dissolution DNP instrument (Oxford Instruments) operating at 1.35 K and 3.35 T to achieve polarizations of ~15-20% for each compound. The compounds were then dissolved in appropriate media: 4.5 mL of 80 mM NaOH/40 mM Tris buffer for [2-^{13}C]pyruvic acid resulting in 80 mM [2-^{13}C]pyruvate (hereafter referred to as C_2-pyruvate); 4.5 mL of 160 mM NaOH/40 mM

Tris buffer for [1-^{13}C]lactic acid resulting in 160 mM [1-^{13}C]lactate (hereafter referred to as lactate); 5mL of 1x phosphate-buffered saline for [^{13}C,$^{15}N_2$]urea resulting in 110 mM [^{13}C,$^{15}N_2$]urea (hereafter referred to as urea); and 5mL of 1x phosphate-buffered saline for HP001 resulting in 100 mM HP001.

4.4.3 bSSFP Sequence

All acquisitions used a custom bSSFP sequence with either one (2D, T_2 mapping) or two (3D) phase encoding dimensions for dynamic high resolution imaging. A prior publication provides a general description of the T_2 mapping sequence [66]. For each time-point in the 3D acquisition, α/2-TR/2 preparation pulses were played for signal stabilization, and α-TR-α/2-TR/2 flip back pulses were played at the end of imaging for storing the remaining magnetization on the longitudinal axis.

A basic 1.6 ms TBW 4 Sinc RF pulse was used for all acquisitions. Frequency and power calibration was performed on a 1 mL enriched [^{13}C]urea vial phantom (6.0M), which was placed on top of the animal. For anatomical reference, 3D bSSFP proton images (16 × 8 × 4.8 cm, 256 × 128 × 80, 5.1 ms TR, 50° flip angle) were acquired.

4.4.4 Retrospective Simulations

Three previously acquired datasets were used for retrospective simulations of the 3D dynamic acquisition (hereafter designated as 3D Dataset 1, 2 and 3, respectively, and shown in Figure 4.1A, 4.1B, and 4.1C, respectively). Specifically, these consisted of: 1) A 3D bSSFP acquired urea dataset in rat kidneys that was transformed into a 4D dataset by applying signal dynamics based on previously published HP ^{13}C studies, 2)

An EPI acquired [1-^{13}C]pyruvate dataset in rat kidneys, and 3) An EPI acquired [1-^{13}C]pyruvate dataset in TRAMP tumor. Since the LLR+S reconstruction was performed for each frequency encode after an FFT along the frequency encode direction (described further in section 4.4.6), one representative slice of each 3D dataset (either containing kidneys or tumor) was used for retrospective simulations. Similarly, two previously acquired T_2 mapping datasets, urea [53] and lactate [66], were used for retrospective undersampling and reconstruction with the LLR+S model (hereafter designated as T_2 Mapping Dataset 1 and 2, respectively, and can be seen in Figure 4.1D and 4.1E, respectively). Each subsequent retrospective simulation was assessed using the structural similarity index (SSIM) [131] and normalized root mean squared error (nRMSE), which was calculated according to the following formula [127]:

$$nRMSE = \frac{\sqrt{\frac{1}{n}\sum_{i=1}^{n}(x_{recon,i}-x_{original,i})^2}}{\sqrt{\frac{1}{n}\sum_{i=1}^{n}(x_{original,i})^2}} \qquad (4.3)$$

where x_{recon} is the reconstructed dataset and $x_{original}$ is the fully sampled original dataset (ground truth).

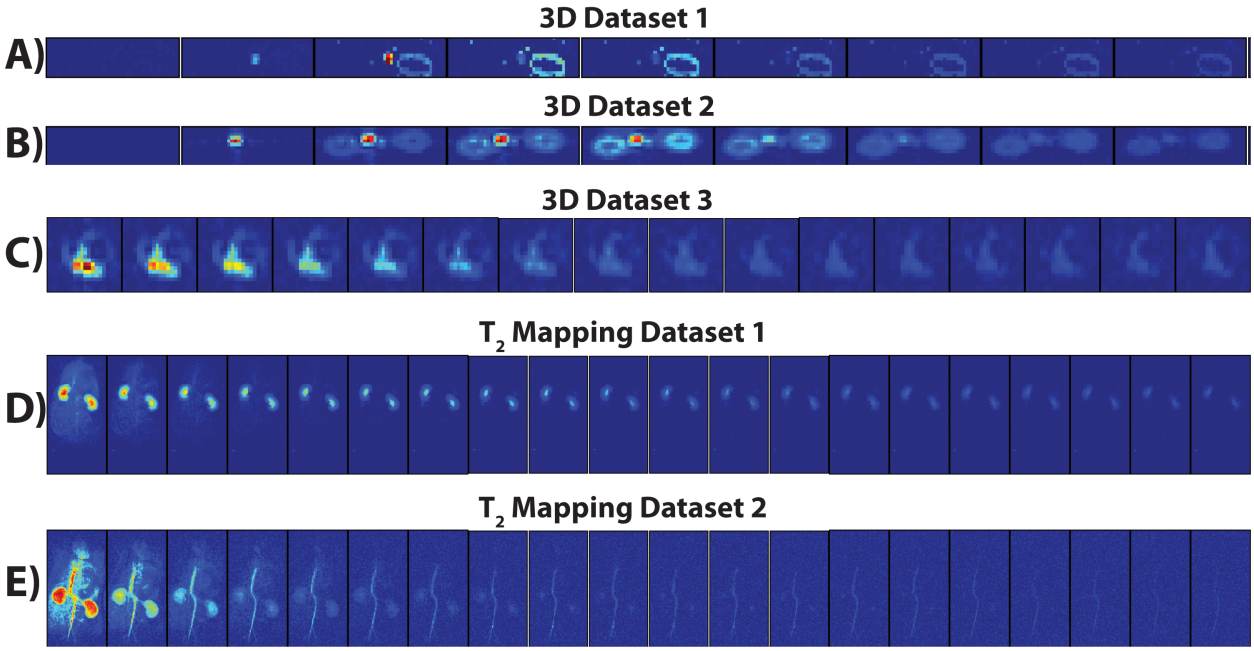

Figure 4.1: *Dynamic representation of the retrospective datasets used in this study: (A) 3D Dataset 1, (B) 3D Dataset 2, (C) 3D Dataset 3, (D) T_2 Mapping Dataset 1, (E) T_2 Mapping Dataset 2.*

The variable-density undersampling patterns in this study were designed with a Monte Carlo simulation [3], with a high density in the k-space center. To maximize incoherent aliasing along the spatiotemporal dimensions, a different pattern was designed for each time-point. An example pattern depicting 75% undersampling of k_y-k_z-t space, which was used in the 3D dynamic imaging, is shown in Figure 4.2A and an example pattern depicting 50% undersampling of k_y-t space, which was used in T_2 mapping, is shown in Figure 4.2B.

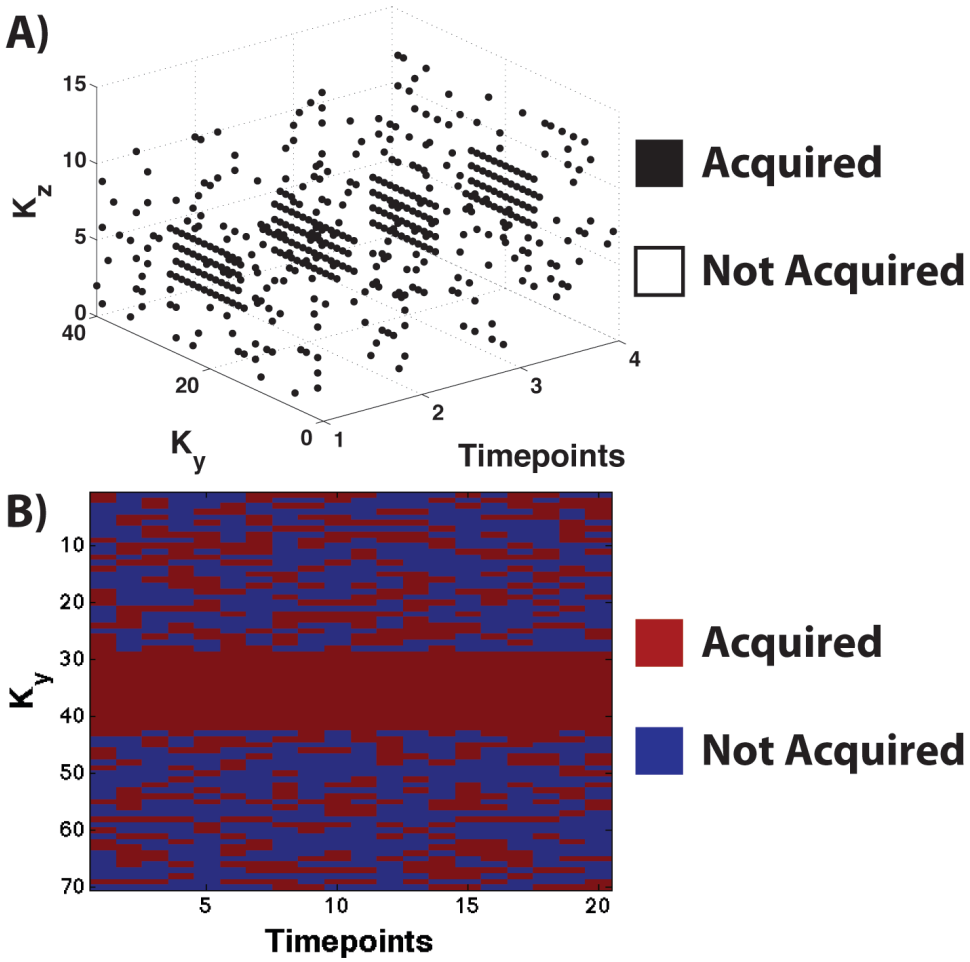

Figure 4.2: *Depiction of undersampling patterns used for the (a) 3D dynamic and (b) 2D dynamic acquisitions. The 3D dynamic acquisitions were undersampled in k_y—k_z-t space with different variable-density patterns with fully sampled k-space centers, with 4 time-points shown above. The 2D dynamic acquisitions were similarly undersampled, but in k_y-t space. Each acquired point within the patterns represents a frequency encoded line of k-space.*

Initial retrospective simulations focused on testing the proper sparse transform and block sizes needed for reconstruction [124], and the compressibility of each 3D dataset [19]. To test the proper sparse transform (wavelet along time (Wavelet), principle component analysis (PCA), temporal FFT (TempFFT), and total variation (TV)), each sparsifying transform was applied to each dataset, and only the top 10% of the resulting coefficients were retained to reconstruct the ground truth. In addition to

validating the sparsifying transform, the appropriate block size for the LLR+S reconstruction was tested based on the different matrix sizes used for T_2 mapping and 3D dynamic imaging. For each dataset, different block sizes were applied as part of the LLR+S reconstruction using a 75% undersampling pattern, with the resulting reconstructions again compared to the ground truth using nRMSE and SSIM. Compressibility of each dataset was tested using five different models: global low rank (GLR) only, local low rank (LLR) only, global low rank plus sparse (L+S), sparse only, and local low rank plus sparse (LLR+S). The data compression was performed based on the method described in Otazo et al. for the low-rank, sparse, and low rank plus sparse models. The LLR and LLR+S models here were tested using the method for the low rank and low rank plus sparse models, respectively. After determining the appropriate sparse transform and block size, for all 3D datasets, undersampling patterns ranging from 10-90% were designed and used in retrospective simulations to measure at what point the reconstruction begins to breakdown, in a similar fashion as described previously [127].

For the T_2 mapping datasets, only compressibility was retrospectively simulated as part of these initial studies. PCA was used as the sparsifying transform based on previous accelerated T_2 mapping acquisitions [124], and 50% undersampling was employed to verify that the undersampled data can be properly reconstructed and the subsequently calculated T_2 maps matched up with the ground truth. The block sizes were set to 5 x 5 based on the results of the retrospective simulations.

4.4.5 In Vivo Hyperpolarized Studies

The prospective 3D dynamic imaging was acquired in three normal Sprague-Dawley rats and one TRAMP mouse for C_2-pyruvate, lactate and urea. The rat acquisition with urea had the following parameters: 12 x 6 x 1.8 cm^3 FOV covering the kidneys, 80 x 40 x 12 matrix size for 1.5 mm isotropic resolution, TR/TE of 7.5 ms/3.75 ms, α = 30° flip angle, 60% undersampling, 13 time-points, 5 s temporal resolution, and the scan starting at the beginning of injection. The rat acquisition with C_2-pyruvate had the following parameters: 12 x 6 x 1.8 cm^3 FOV covering the kidneys, 60 x 30 x 9 matrix size for 2 mm isotropic resolution, TR/TE of 7.5 ms/3.75 ms, α = 30° flip angle, 60% undersampling, 13 time-points, 5 s temporal resolution, and the scan starting at the beginning of injection. The rat acquisition with urea had the following parameters: 12 x 6 x 1.8 cm^3 FOV covering the kidneys, 80 x 40 x 12 matrix size for 1.5 mm isotropic resolution, TR/TE of 6.4 ms/3.2 ms, variable flip angle, 75% undersampling, 13 time-points, 3 s temporal resolution, and the scan starting 15 s after the beginning of injection. The mouse acquisition for all three compounds had the following parameters: 6 x 3 x 3 cm^3 FOV covering the tumor, 40 x 20 x 20 matrix size for 1.5 mm isotropic resolution, TR/TE of 6.4 ms/3.2 ms, variable flip angle, 75% undersampling, 16 time-points, 2 s temporal resolution, and the scan starting 15 s after the beginning of injection.

The prospective T_2 mapping was acquired in three normal Sprague-Dawley rats for all compounds. C_2-pyruvate, lactate, and HP001 acquisitions had the following parameters: 14 x 7 cm^2 coronal FOV covering heart and abdomen, 140 x 70 matrix size for 1 mm^2 in-plane resolution, TR/TE of 8.5 ms/4.25 ms, α = 180° flip angle, 50%

undersampling, 20 time-points, and the scan starting 30 s after the beginning of injection. Urea acquisitions had the following parameters: 14 x 7 cm^2 coronal FOV heart and abdomen, 280 x 140 matrix size for 0.25 mm^2 in-plane resolution, TR/TE of 12.5 ms/6.25 ms, α = 180° flip angle, 50% undersampling, 20 time-points, and the scan starting 30 s after the beginning of injection. Fully sampled acquisitions of HP001 and urea were acquired at the same time as the undersampled acquisitions for comparison and had the following parameters: 14 x 7 cm^2 coronal FOV heart and abdomen, 140 x 70 matrix size for 1 mm^2 in-plane resolution, TR/TE of 8.5 ms/4.25 ms, α = 180° flip angle, 20 time-points, and the scan starting 30 s after the beginning of injection. Initial 3D T_2 mapping of urea acquisitions had the following parameters: 12 x 6 x 1.8 cm^3 FOV covering the kidneys, 1-2.5 mm isotropic resolution, TR/TE of 6.4 ms/3.2 ms, α = 180° flip angle, 75% undersampling, 20 time-points, and the scan starting 30 s after the beginning of injection.

4.4.6 Image Reconstruction

Reconstruction of all datasets used the same sparse transform and block sizes for the LLR+S retrospective reconstructions. For the 3D dynamic and 3D T_2 mapping acquisitions, the data was Fourier transformed along the readout dimension to x-ky-kz-t and the LLR+S algorithm was subsequently applied to each x location separately, while for 2D T_2 mapping the algorithm was applied to kx-ky-t. The total reconstruction time on a Linux Workstation with a 3.07 GHz quad-core Intel Xeon CPU was approximately 10 minutes for 3D dynamic acquisitions and approximately 2 minutes for 2D T_2 mapping acquisitions.

4.5 Results

4.5.1 LLR+S Reconstruction of Retrospective Simulations

4.5.1.1 temporal sparsity and bsize

Table 4.2 shows the nRMSE of the four different temporal sparse transforms for all three retrospective 3D datasets after transformation and retention of the top 10% of coefficients. PCA outperformed the other three for all datasets and was used in subsequent simulations and reconstructions, with the wavelet transform having the second lowest nRMSE for all the datasets.

Table 4.3 shows the nRMSE for the different block sizes that were tested for each retrospective 3D dataset. The block sizes that resulted in the lowest nRMSE were about ~1/5-1/4 the size of the matrix for the phase encode direction and were used in subsequent retrospective simulations: [8,3] for the 40 x 12 matrix sizes used in 3D Datasets 1 and 2; [5,5] for the 20 x 20 matrix sizes used in 3D Dataset 3.

3D Dataset 1				
	TempFFT	Wavelet	TV	PCA
nRMSE	0.3638	0.2968	0.4983	0.2712
SSIM	0.7053	0.7486	0.6484	0.7586
3D Dataset 2				
	TempFFT	Wavelet	TV	PCA
nRMSE	0.1944	0.1562	0.3016	0.092
SSIM	0.6772	0.6618	0.6138	0.8941
3D Dataset 3				
	TempFFT	Wavelet	TV	PCA
nRMSE	0.1497	0.1777	0.3614	0.0631
SSIM	0.7581	0.7177	0.5875	0.88

Table 4.2: *Comparison of the different sparsifying transforms on all three 3D retrospective datasets. Comparison to the ground truth was done after retaining only the top 10% of sparsifying coefficients.*

3D Dataset 1						
bsize	4,2	5,3	6,3	8,3	10,3	20,6
nRMSE	0.1177	0.0995	0.1129	0.0908	0.1095	0.2702
SSIM	0.9329	0.9475	0.9368	0.9543	0.9455	0.8788
3D Dataset 2						
bsize	4,2	5,3	6,3	8,3	10,3	20,6
nRMSE	0.1502	0.1392	0.1429	0.1344	0.1385	0.2161
SSIM	0.9126	0.9187	0.9176	0.9239	0.9215	0.9047
3D Dataset 3						
bsize	2,2	4,4	5,5	10,10		
nRMSE	0.1327	0.0913	0.0848	0.1301		
SSIM	0.954	0.9631	0.9643	0.9482		

Table 4.3: *Comparison of different block sizes (bsize) used in the LLR+S reconstruction for all three 3D datasets.*

4.5.1.2 Comparison of Reconstruction Algorithms

The top row of Figure 4.3 depicts the nRMSE vs. compression ratio for the retrospective 3D datasets with the five different types of reconstruction algorithms. The LLR+S method showed the lowest nRMSE across multiple compression ratios for all the retrospective 3D datasets, indicating the highest percent undersampling can be achieved when using that algorithm. The bottom row of Figure 4.3 depicts the nRMSE vs. percent undersampling for the retrospective 3D datasets. Based on the results for all the datasets, >75% undersampling was deemed the point where the reconstruction began to fail as the nRMSE began rising rapidly past that point, indicating severe distortion from the ground truth after reconstruction. Figure 4.4 shows an example result from a reconstruction of 3D dataset 1 with 75% undersampling, where one slice of the

reconstruction is shown compared to the ground truth slice and zero-filled slice, along with the SSIM map between the ground truth and reconstruction, and representative dynamic curves from the vasculature and kidneys. The SSIM map and dynamic curves, along with visual inspection of the slices show that the reconstruction successfully eliminated undersampling artifacts and recovered the original signal.

Figure 4.5A shows the resulting T_2 maps after retrospective 50% undersampling and reconstruction of T_2 Mapping Dataset 1. The LLR+S reconstruction matched up well with the ground truth qualitatively, as well as based on the ratio between the two maps being equal ~1 and the representative signal decay curves in Figure 4.5B. Figure 4.5C shows similar results to Figure 4.3A-C, whereby the LLR+S method showed the lowest nRMSE across multiple compression ratios for the T_2 Mapping Dataset 1, indicating the highest percent undersampling can be achieved when using that algorithm.

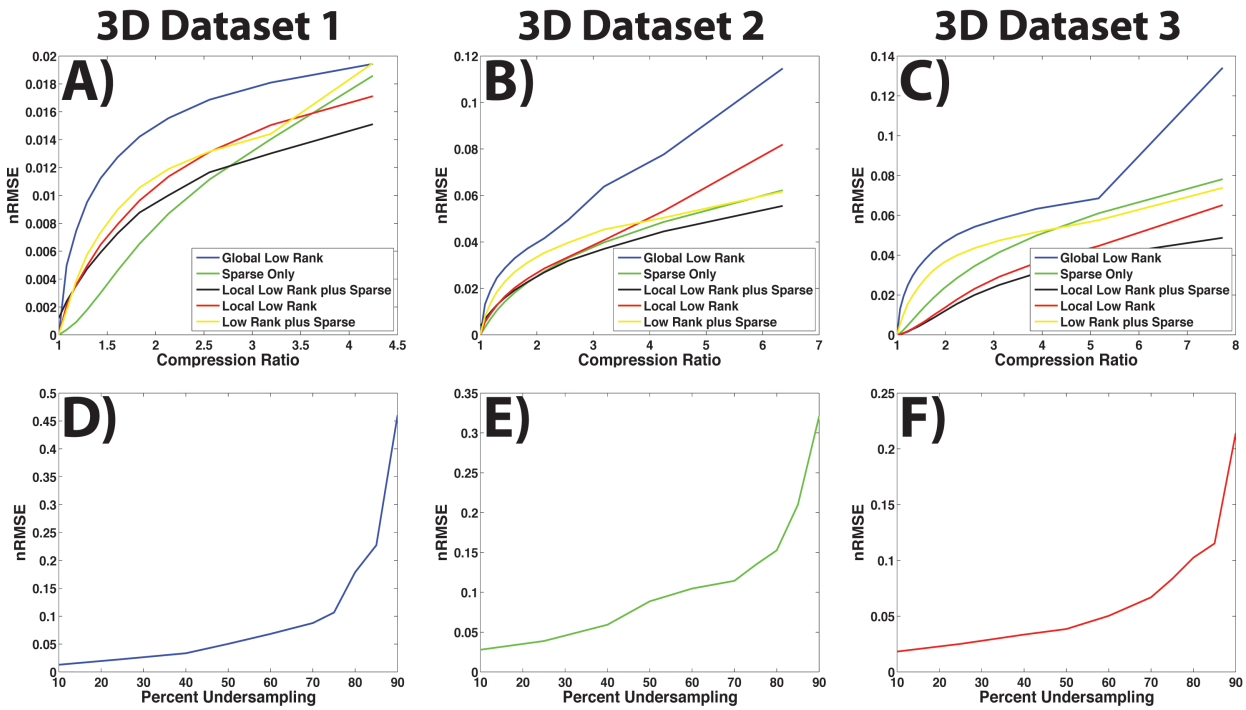

Figure 4.3: *Different undersampling factors were used to test the capability of the LLR+S reconstruction for all three retrospective 3D datasets. Parts A-C depict the nRMSE vs. compression ratio for the three retrospective 3D datasets, respectively, with the five different types of reconstruction algorithms. For all three datasets, the LLR+S method showed the lowest nRMSE across multiple compression ratios, indicating the highest percent undersampling can be achieved when using that algorithm. Parts D-F depict the nRMSE vs. percent undersampling for all three retrospective 3D datasets, respectively, with >~75% undersampling being the point where the reconstruction begins to considerably breakdown.*

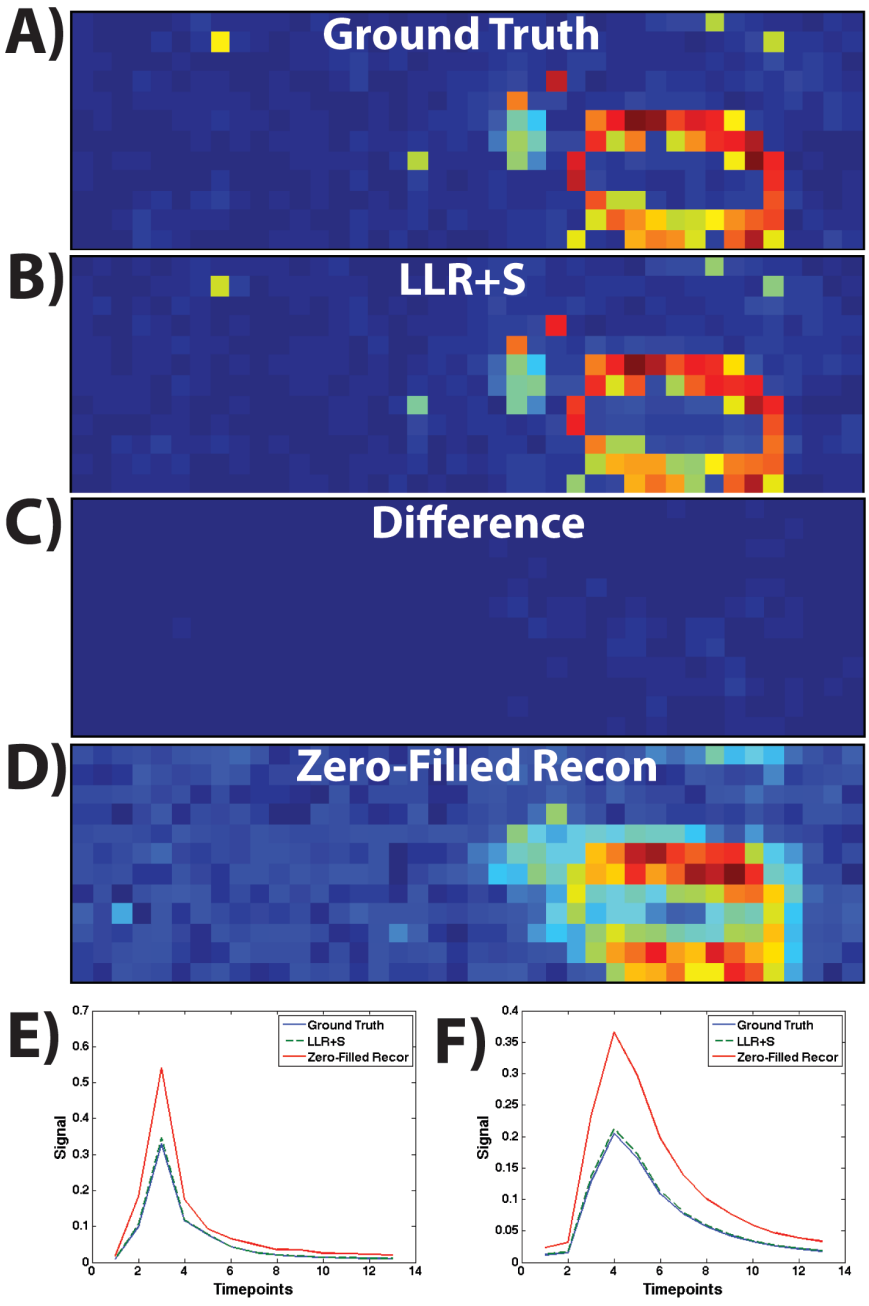

Figure 4.4: *An example reconstruction of 3D dataset 1 (B) with 75% undersampling can be seen here compared to the ground truth (A), along with the difference image (C), zero-filled reconstruction (D), and comparison of dynamic curves between the ground truth, LLR+S reconstruction, and the zero-filled reconstruction for the vasculature (E) and kidney (F). The LLR+S reconstruction matches up closely with the ground truth based on the difference image, qualitative observation and the dynamic curves, while the zero-filled reconstruction has severe aliasing. All images were scaled from 0 to 1.*

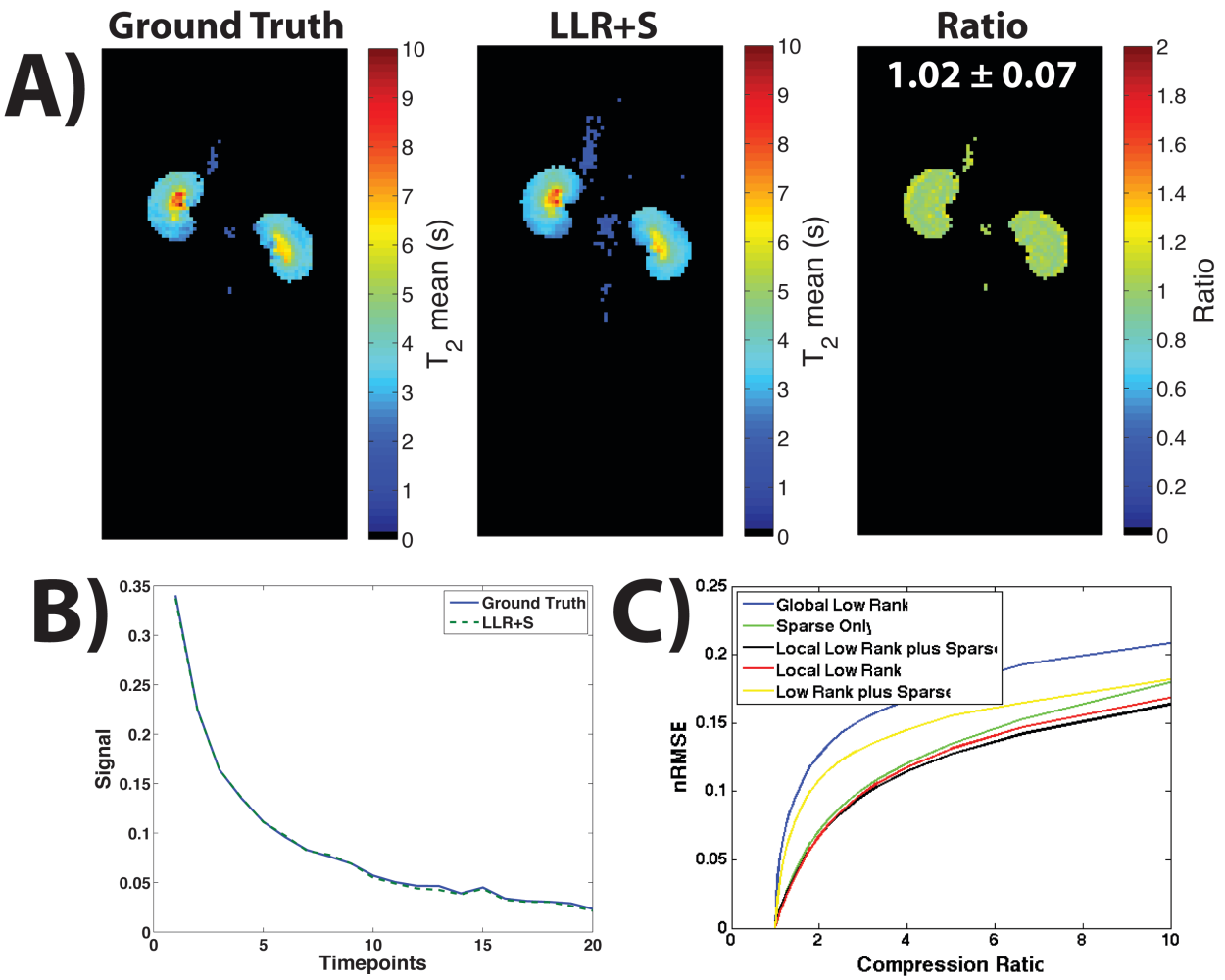

Figure 4.5: *The LLR+S reconstruction was tested on retrospective T_2 Mapping Dataset 1. The LLR+S reconstruction matches up with the fully sampled ground truth as evidenced by the ratio map being equal ~1 (A). Furthermore, representative decay curves (B) from the ground truth and LLR+S match up very well. Part C shows the nRMSE vs. compression ratio for T_2 Mapping Dataset 1, with the LLR+S reconstruction showing better compressibility compared to other reconstruction algorithms.*

4.5.2 LLR+S Reconstruction of Prospective 3D Dynamic Acquisitions

Figure 4.6 shows the reconstructions of the prospective *in vivo* urea (A), lactate (B), and C_2-pyruvate (C) datasets acquired in rats. Each part shows a 3D view of one time-point, all time-points of a representative kidney slice (outlined in black), representative vascular and kidney dynamic curves, and a carbon overlay on the ^1H anatomical image. The LLR+S algorithm successfully reconstructed both 60% and 75%

undersampled datasets, with the dynamic curves matching up with expected *in vivo* dynamics for all three compounds in healthy rat kidneys and vasculature. The SNR was high enough for 3D visualization for around 30 s after the start of the scan (2^{nd}-7^{th} time-point) for the urea and C_2-pyruvate acquisitions, and considerably longer in the lactate acquisition with the use of a variable flip angle scheme and later scan start time.

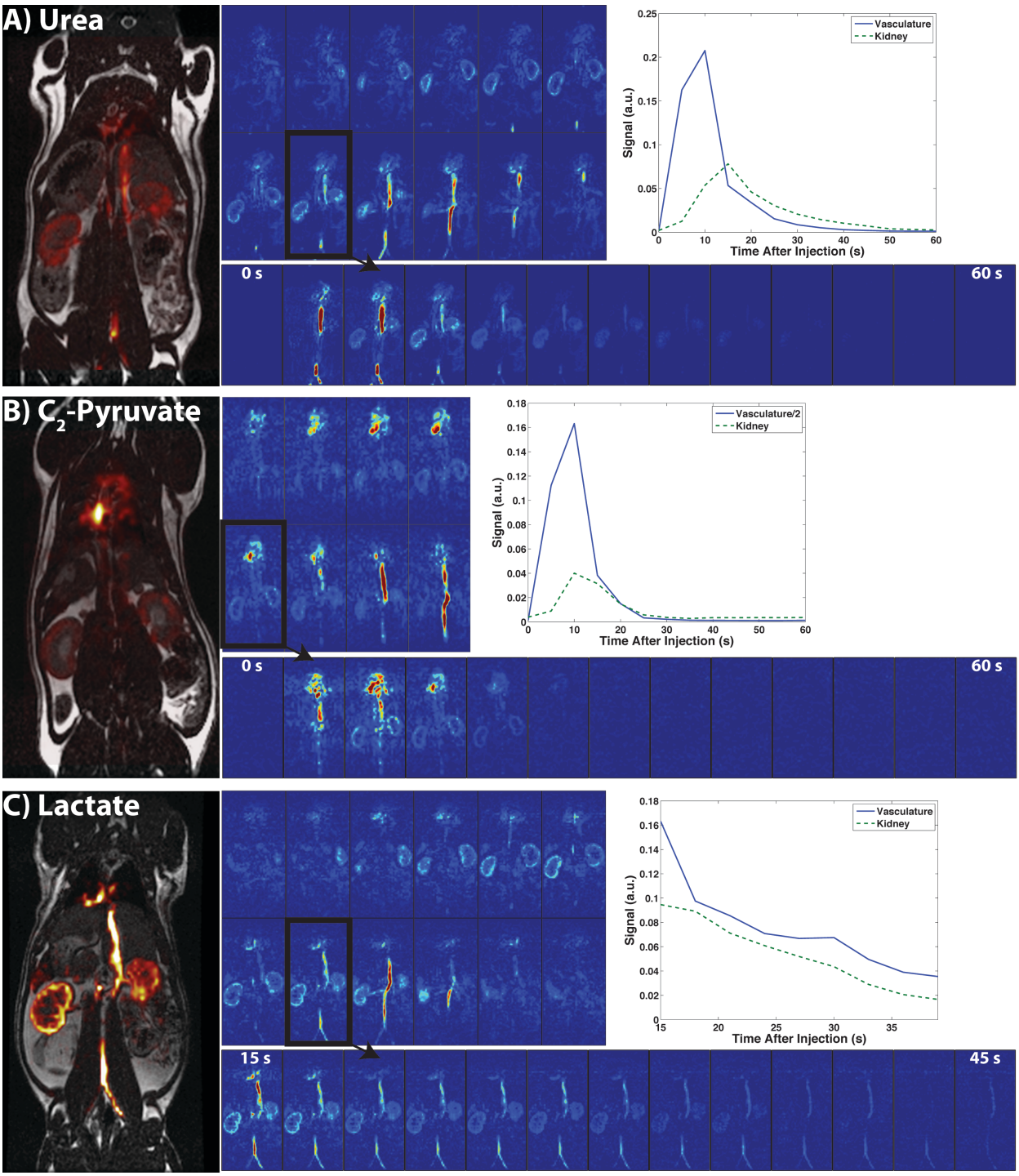

Figure 4.6: *Depiction of the urea (A), C_2-pyruvate (B), and lactate (C) uptake and biodistribution of the 3D dynamic acquisition in one Sprague-Dawley rat. The full 3D view of each compound at 15 s and in one slice (outlined in black) dynamically from 0-60 s (15-54 s in lactate) indicates uptake in vasculature, kidneys, and heart. The dynamics in the vasculature and the kidneys can also be seen on the top right of each part, along with carbon overlays of the outlined slice on top of anatomical ^{1}H images on the left.*

Figure 4.7 shows the reconstructions of the prospective *in vivo* urea (A), lactate (B), and C_2-pyruvate (C) datasets acquired in a tumor-bearing mouse. As with Figure 4.6, each part shows a 3D view of one time-point, all time-points of a representative tumor slice (outlined in black), and a carbon overlay on the ^{1}H anatomical image. The LLR+S algorithm successfully reconstructed the 75% undersampled datasets and the dynamic curves matched up with expected *in vivo* dynamics for all three compounds in a TRAMP tumor. The SNR was high enough for 3D visualization for several time-points for all three compounds, even at 1.5 mm isotropic resolution.

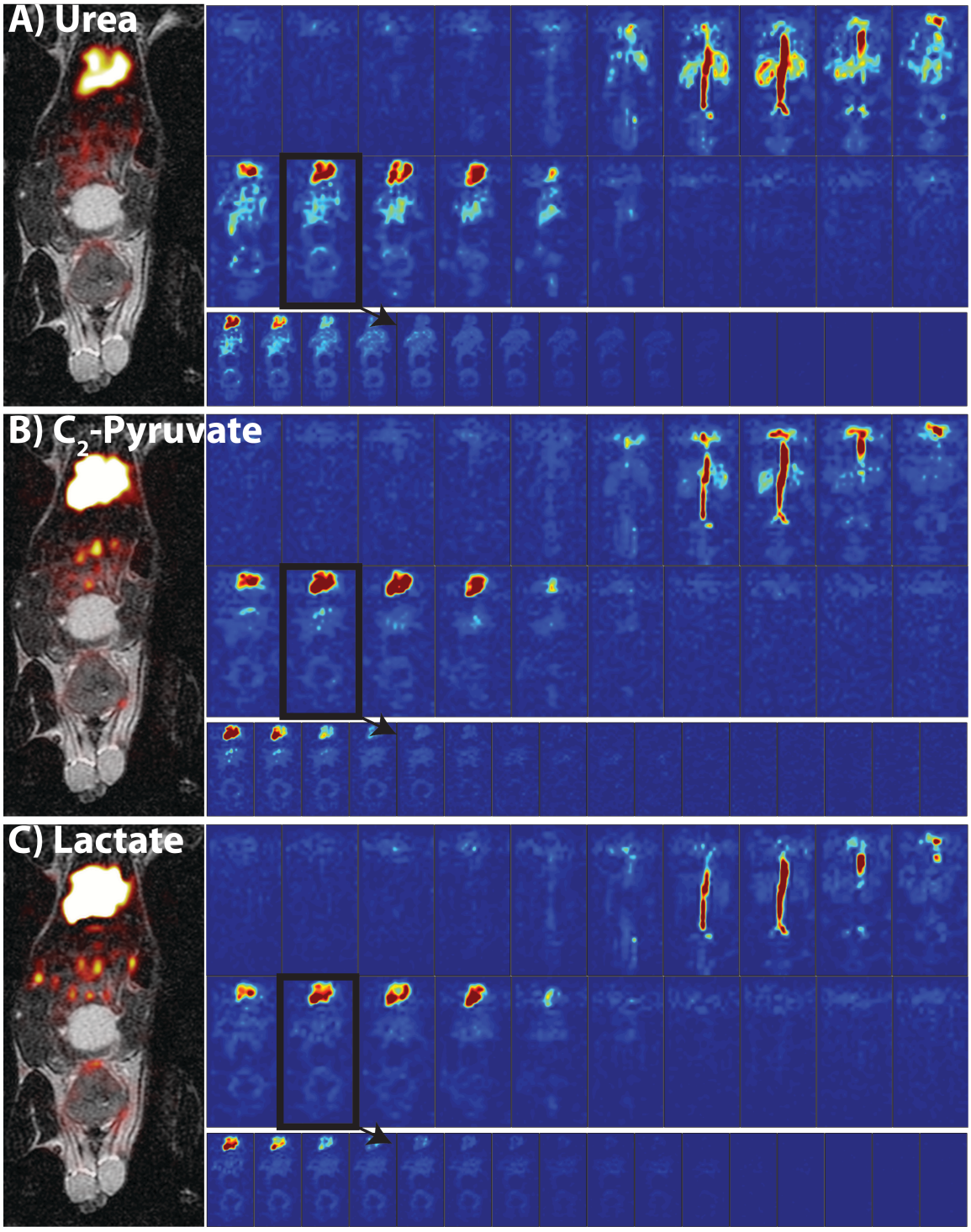

Figure 4.7: *Depiction of the urea (A), C_2-pyruvate (B), and lactate (C) uptake and biodistribution of the 3D dynamic acquisition in a tumor-bearing mouse. The full 3D view of each compound at 15 s and in one slice (outlined in black) dynamically from 15-45 s indicates uptake in vasculature, tumor periphery, kidneys, and heart. The carbon overlays of the outlined slice on top of anatomical ^{1}H images on the left.*

4.5.3 LLR+S Reconstruction of Prospective T_2 Maps

The prospective LLR+S reconstructed 2D T_2 mapping acquisitions of HP001 and urea matched up well with the fully sampled acquisitions, as evidenced by the ratio maps of the fully sampled and accelerated acquisitions for urea (Figure 4.8A and 4.8B) and HP001 (Figure 4.8C), which had an average value of 0.89 ± 0.21 and 0.95 ± 0.23 in the kidneys and vasculature, respectively. The urea acquisition demonstrated the capability of sub-millimeter in-plane resolution acquisitions for HP probes with sufficient acceleration. The average value in the kidneys for C_2-pyruvate (Figure 4.9B), 0.786 ± 0.13, agreed well with previously acquired, lower resolution T_2 maps [66]. The LLR+S reconstruction allowed ~6-fold improvement in resolution even with C_2-pyruvate having a relatively short *in vivo* average T_2. Additionally, both lactate (~2.43s in kidneys) (Figure 4.9A) and 3D urea T_2 maps (~4.84s in kidneys) (Figure 4.9C and 4.9D) matched up well with literature values [53,66], with the 3D urea T_2 map demonstrating the capability of 1 mm isotropic dynamic imaging with HP probes.

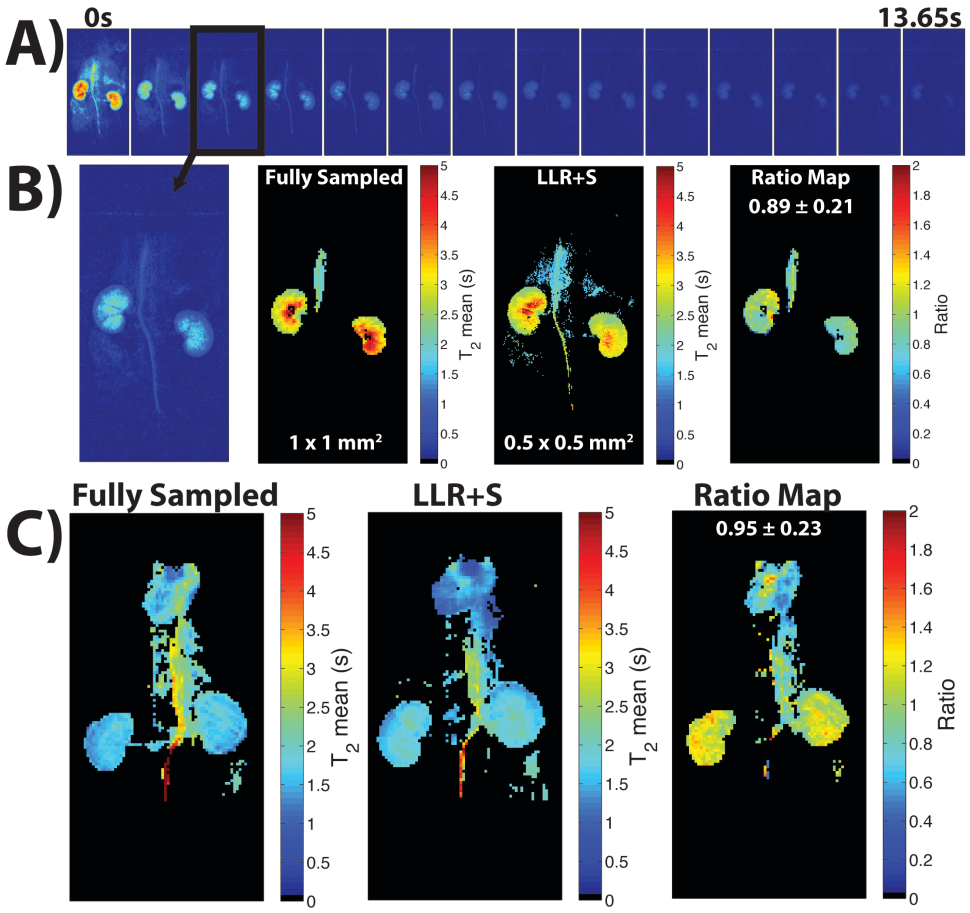

Figure 4.8: *2-fold accelerated acquisitions of 0.5 x 0.5 mm^2 urea and 1 x 1 mm^2 HP001 T_2 mapping are presented here. Part A shows the slices of the urea acquisition, with the signal lasting longest in the kidneys due to the long T_2s. Part B shows a zoomed-in version of the outlined slice in part A, which shows the resolution being high enough to accurately visualize the different kidney compartments. Additionally, comparison of the LLR+S reconstructed T_2 map to the fully sampled 1 x 1 mm^2 T_2 map revealed a good agreement in calculated T_2 values. The ratio map had an average of 0.89 ± 0.21 (mean ± intra-image standard deviation) within the kidneys and vasculature. Part C shows the results of the HP001 T_2 mapping. Similar to the urea results, comparison to the fully sampled 1 x 1 mm^2 acquisition revealed a good agreement in calculated T_2 values. The ratio map had an average of 0.95 ± 0.23 (mean ± intra-image standard deviation) within the kidneys and vasculature.*

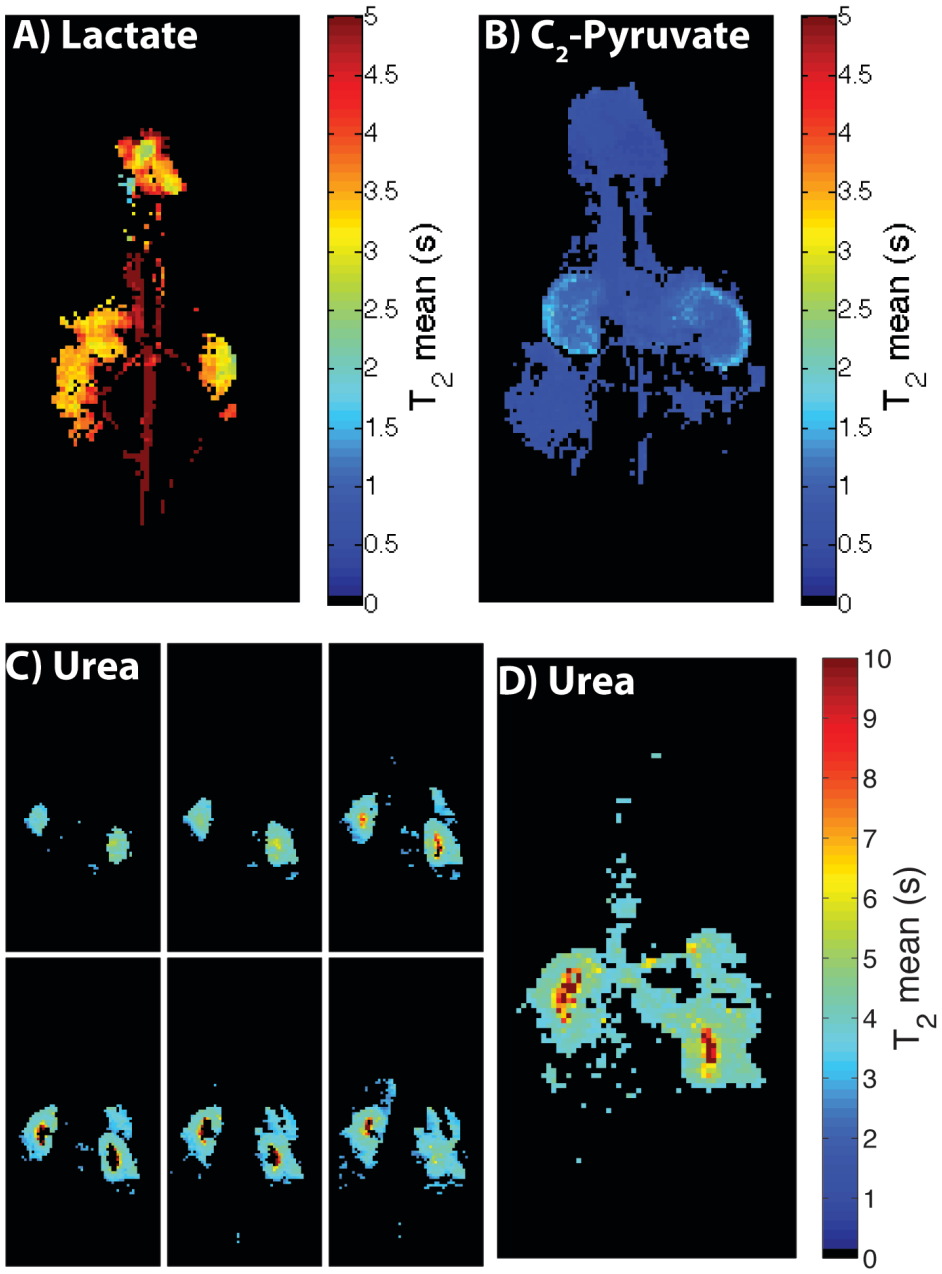

Figure 4.9: *High resolution T_2 maps for other substrates, such as lactate (A) and C_2-pyruvate (B), are shown here. The accelerated acquisitions had high enough spatial resolution to visualize the substrate in kidney, heart, and vasculature, with the mean T_2 values matching up well with previously acquired T_2 maps. The slice by slice T_2 map (C) and maximum intensity projection representation (D) from the urea 3D 1 mm isotropic T_2 mapping acquisition show clear delineation of renal cortex, medulla, pelvis, and vasculature, with the T_2 distribution matching up with literature values. Only 6 representative slices (out of 18) are shown in part C, while the maximum intensity projection in part D is from all slices.*

4.6 Discussion

With the current desire for high spatiotemporal coverage of hyperpolarized ^{13}C compounds, especially with recent successful clinical human studies that require large FOVs, the need for accelerated acquisitions with sub-Nyquist sampling strategies and accompanying reconstructions is evident. Low rank plus sparse and local low rank reconstruction strategies have been previously employed in undersampled dynamic ^{1}H acquisitions. We demonstrated the development and application of the local low rank plus sparse algorithm for reconstruction of undersampled 3D dynamic and 2D/3D T_2 mapping hyperpolarized ^{13}C acquisitions with the bSSFP sequence. The algorithm allowed for up to ~75% undersampling depending on the particular acquisition, with the acceleration factor providing considerably faster effective echo times for high SNR acquisitions. We were able to achieve previously unseen 2D sub-millimeter and 1-1.5 mm 3D isotropic spatial resolutions with considerable temporal resolutions and temporal windows.

Due to the nonrecoverable nature of the hyperpolarized magnetization, the number of phase encoding steps done in HP ^{13}C imaging acquisitions is considerably smaller than ^{1}H imaging acquisitions, which limits the amount of undersampling possible. The bSSFP sequence is an attractive choice for acceleration since the spatial resolution and matrix sizes approach that of 2D high resolution ^{1}H imaging. Additionally, translating this sequence into the clinic will require much larger matrix sizes to achieve sub-cm spatial resolution due to the larger FOVs, which may allow for higher acceleration factors beyond what has been shown in this study. Based on previous ^{1}H studies with local low rank and low rank plus sparse reconstructions, the algorithm

presented here can be easily combined with parallel imaging and other types of imaging sequences, including echo-planar, spiral, and radial imaging [10,11,15,19]. Other types of reconstructions can be further evaluated and compared to the LLR+S algorithm, including multi-scale low rank [132] and model-based/dictionary learning [133]. Furthermore, the results presented here depict the LLR+S reconstruction working for different approaches for dynamic acquisitions, which can be optimized in general depending on the type of biological information desired. For example, the 3D dynamic urea and C_2-pyruvate sequences began at the start of injection and were acquired for 60 s, and represent acquisitions looking at potentially perfusion, biodistribution, and uptake of the injected substrate. The 3D dynamic lactate sequence began after the end of injection and was only acquired for 39 s, but provided higher SNR due to both a shorter acquisition window and the use of a variable flip angle scheme.

Future work will focus on optimizing the acquisitions present here with improved flip angle schemes to maximize SNR over the entire temporal window, and incorporate spectrally selective pulses for accelerated metabolic imaging of [1-^{13}C]pyruvate. In addition, further evaluation is needed on what information may be obtained from the individual L and S components that result from running the algorithm. As discussed previously in Otazo et al. [19], the L+S sum represents the image reconstruction and the individual background and dynamic components are less important.. In the case of hyperpolarized ^{13}C imaging, since the signal is always decaying away back to equilibrium due to various processes, there is no explicit separation of slowly-varying background and dynamic components as can be found in cardiac perfusion, for example. While it is beyond the scope of this study, it is possible that the individual L

and S components in hyperpolarized ^{13}C imaging depict different levels of decaying signal, as in the L component shows regions of slower decay, and the S component shows regions of fast decay. However, this theory would need to be investigated further. Based on the simulations above, the sum of L and S outperformed other compressed sensing reconstructions, and was consequently the focus of this study.

4.7 Conclusion

In this study, we developed and tested a local low rank plus sparse reconstruction algorithm to accelerate hyperpolarized ^{13}C imaging with the balanced steady-state free precession sequence. We were able to acquire high spatiotemporal 3D images in healthy rat kidneys and tumor-bearing mice, as well as high spatial resolution 2D and 3D T_2 maps of multiple hyperpolarized substrates. Future work will focus on adapting the reconstruction algorithm for parallel imaging and translation into clinical studies.

Chapter 5: High Spatiotemporal Resolution bSSFP Imaging of Hyperpolarized [1-^{13}C]Pyruvate and Lactate using Spectral Suppression of Alanine and Pyruvate-Hydrate

5.1 Abstract

The bSSFP acquisition enables high spatiotemporal resolution for hyperpolarized ^{13}C MRI at 3T, but is limited by spectral contamination from adjacent resonances. The purpose of this study was to develop a framework for in vivo dynamic high resolution imaging of hyperpolarized [1-^{13}C]pyruvate and [1-^{13}C]lactate generated in vivo at 3T by simplifying the spectrum through the use of selective suppression pulses. Spectral suppression pulses were incorporated into the bSSFP sequence for suppression of [1-^{13}C]alanine and [1-^{13}C]pyruvate-hydrate signals, leaving only the pyruvate and lactate resonances. Subsequently, the bSSFP pulse width, time-bandwidth, and repetition time were optimized for imaging these dual resonances. The spectral suppression reduced both the alanine and pyruvate-hydrate signals by 85.5 ± 4.9% and had no significant effect on quantitation of pyruvate to lactate conversion (liver: P = 0.400, kidney: P = 0.499). High resolution (2 x 2 mm^2 and 3 x 3 mm^2) sub-second 2D coronal projections and 3D 2.5 mm isotropic images were obtained in rats and tumor-bearing mice with 1.8-5 s temporal resolution, allowing for calculation of lactate-to-pyruvate ratios and k_{PL}. The developed framework presented here shows the capability for dynamic high resolution volumetric hyperpolarized bSSFP imaging of pyruvate-to-lactate conversion on a clinical MR scanner.

5.2 Introduction

New developments in hyperpolarized (HP) ^{13}C MRI via dissolution dynamic nuclear polarization have facilitated real-time detection of [1-^{13}C]pyruvate biodistribution and metabolism in various diseases, including cancer and diabetes [31,33,81,121]. The conversion of pyruvate to lactate as a potential biomarker in disease prognosis and aggressiveness has been studied extensively, including in a recent successful phase I clinical trial focused on prostate cancer patients, and in recent ongoing phase II clinical trials focused on prostate cancer, brain cancer, and liver metastases [59–63]. Because the hyperpolarized magnetization is nonrecoverable and constantly depleted due to the effects of RF excitation and metabolism, multiple rapid imaging strategies have been investigated, including MR spectroscopic imaging (MRSI), spiral, and echo planar imaging (EPI) [5,41,65,71,73,134]. Each of these sequences provides adequate spectral resolution, but has limitations in additionally achieving both high spatial and temporal resolution with sufficient SNR.

Recent publications have focused on optimizing high spatiotemporal resolution imaging for HP ^{13}C MRI with the balanced steady-state free precession (bSSFP) sequence since it offers the highest SNR per unit time [28,66,135]. The advantage of the bSSFP sequence is readily apparent when imaging single non-metabolized compounds, such as urea, or multiple non-metabolized compounds with large chemical shift differences [51,52,135]. Because of the SNR efficiency, 1.5 mm 3D Isotropic (0.0034 cm^3) HP ^{13}C imaging is currently possible with the bSSFP sequence at 3T [66], which is a higher spatial resolution compared to current EPI [136,137], MRSI [41], and spiral imaging [138,139] acquisitions. However, due to the difficulty in dealing with off-

resonance with this sequence (i.e. banding artifacts), imaging of HP [1-^{13}C]pyruvate and the resulting metabolites is much more challenging because of the small chemical shift between the metabolites and the need for high spectral selectivity. While various options are available, such as a multi-echo or low bandwidth approach among others [79,140], these options are sub-optimal for high spatiotemporal resolution imaging and potentially involve complex reconstructions, as detailed previously [28].

A recent publication presented a method for acquiring HP [1-^{13}C]pyruvate, [1-^{13}C]lactate, and [^{13}C,$^{15}N_2$]urea simultaneously with the bSSFP sequence at 14T by optimizing the RF pulse and TR for spectral selectivity and cycling through the three transmit frequencies for dynamic imaging [28]. This approach exploits the large frequency separation at 14T, as well as the use of higher strength gradients available on a preclinical system, which enables short RF pulses and short TRs. Translation of this approach to clinically relevant field strengths is considerably more challenging due to the ~5x closer frequency separation (i.e. compared to 3T). The RF pulse widths necessary for spectral selectivity are closer to ~20 ms, leading to long TRs and a frequency response unsuitable for bSSFP imaging due to B_0 inhomogeneity and consequent banding artifacts.

The goal of this study was to develop a new method for fast, high resolution imaging of [1-^{13}C]pyruvate and its metabolic product [1-^{13}C]lactate at 3T with the bSSFP sequence. Spectral suppression pulses centered on [1-^{13}C]alanine and [1-^{13}C]pyruvate-hydrate were played prior to imaging to reduce the problem to a two-peak system. The combination of these spectral suppression pulses and a carefully chosen RF pulse width and time-bandwidth (TBW) allowed for a TR of ~15 ms. This method was tested

on phantoms and applied in healthy rat kidneys and tumor-bearing mice with 2D coronal projections and 3D imaging at <5 s temporal resolution.

5.3 Methods

5.3.1 Sample preparation

[1-^{13}C]pyruvate was prepared as described previously [66]. ~24 uL of sample was polarized in a HyperSense system (Oxford Instruments, Abingdon, UK) operating at 3.35 T and 1.35 K for ~1 hour, and subsequently dissolved in ~4.5 mL of NaOH/Tris buffer, resulting in a 80 mM [1-^{13}C]pyruvate solution at physiologic pH and temperature.

5.3.2 Animal preparation and hardware

All animal studies were done under protocols approved by the University of California San Francisco Institutional Animal Care and Use Committee (IACUC). Healthy Sprague-Dawley rats and tumor-bearing mice (transgenic adenocarcinoma of mouse prostate or TRAMP [42]) were used during the course of these experiments. The rats and mice were anesthetized using isoflurane (1.5%, gas flow rate 1 L/min) and inserted with lateral tail vein catheters.

All experiments were performed on a 3 Tesla clinical MRI scanner (GE Healthcare, Waukesha, WI) using custom dual-tuned ^{13}C/^{1}H quadrature transceiver radiofrequency (RF) coils (8 cm diameter for rats and 5 cm diameter for mice). All animals were placed in a supine position on a heated pad within the coil for the duration of the experiments. A 1 mL enriched [^{13}C]urea vial phantom (6.0 M) was placed on top of the animal near the abdominal region and used for frequency and power calibration.

5.3.3 MR Experiments

A 20 ms Shinnar-Le Roux (SLR) designed spectral suppression pulse (Fig. 5.1A) with an excitation bandwidth of 150 Hz (Fig. 5.1B) was used during the course of these studies [141]. The suppression capability of the pulse was first tested with a slab-selective magnetic resonance spectroscopy (MRS) sequence using a thermal ^{13}C phantom that consisted of four different sized chambers containing 1 M sodium lactate (185 ppm), 2 M sodium formate (a doublet at 166 and 173 ppm), 1 M sodium bicarbonate (163 ppm), and 1 M alanine (178 ppm). The MRS parameters were: one 50 mm axial slab covering the phantom, RF compensated progressive flip angle scheme, adiabatic double-spin echo [142], 120 ms TE, 25 kHz spectral width, 2048 spectral points, 3 s temporal resolution, 10 time-points, with one suppression pulse played out prior to each time-point, with the suppression pulse waveform ending 1 ms before slab excitation. The suppression pulse center frequency was centered on lactate and moved downfield in 10 Hz increments up to 180 Hz.

Subsequently, the pulse was also tested in vivo in rats with the slab-selective MRS sequence, with each animal undergoing one scan with spectral suppression and one scan without spectral suppression. The in vivo parameters were: two 12 mm axial slabs, one localized on liver and one on kidney, RF compensated progressive flip angle scheme, double-spin echo, 120 ms TE, 25 kHz spectral width, 2048 spectral points, 3 s temporal resolution, 10 time-points, with one suppression pulse (centered ~158 Hz upfield of lactate, between the alanine and pyruvate-hydrate resonances) played out prior to each time-point, ending 1 ms before slab excitation. All scans started at 20 s

after beginning of injection and 3 mL of 80 mM [1-^{13}C]pyruvate was injected over 12 s via tail vein catheters in six different rats.

Unless otherwise noted all subsequent acquisitions used a custom ^{13}C bSSFP sequence, with α/2–TR/2 preparation pulses and α-TR/2-α/2 flip back pulses storing remaining magnetization on the longitudinal axis [66]. Figure 5.1A shows the entire 3D version of the sequence (without the flip back pulses), with the spectral suppression pulses and associated crusher gradients. The RF pulse width and TR/TE necessary for bSSFP imaging were simulated and chosen to selectively excite either pyruvate or lactate, whereby a 6.8 ms sinc pulse (TBW = 2) led to a TR/TE of 15.3/7.65 ms. The selectivity was tested using both a thermal [^{13}C]urea phantom and hyperpolarized [^{13}C,$^{15}N_2$]urea phantom. The phantom experiments were acquired by alternating between on-resonance and 390 Hz off-resonance.

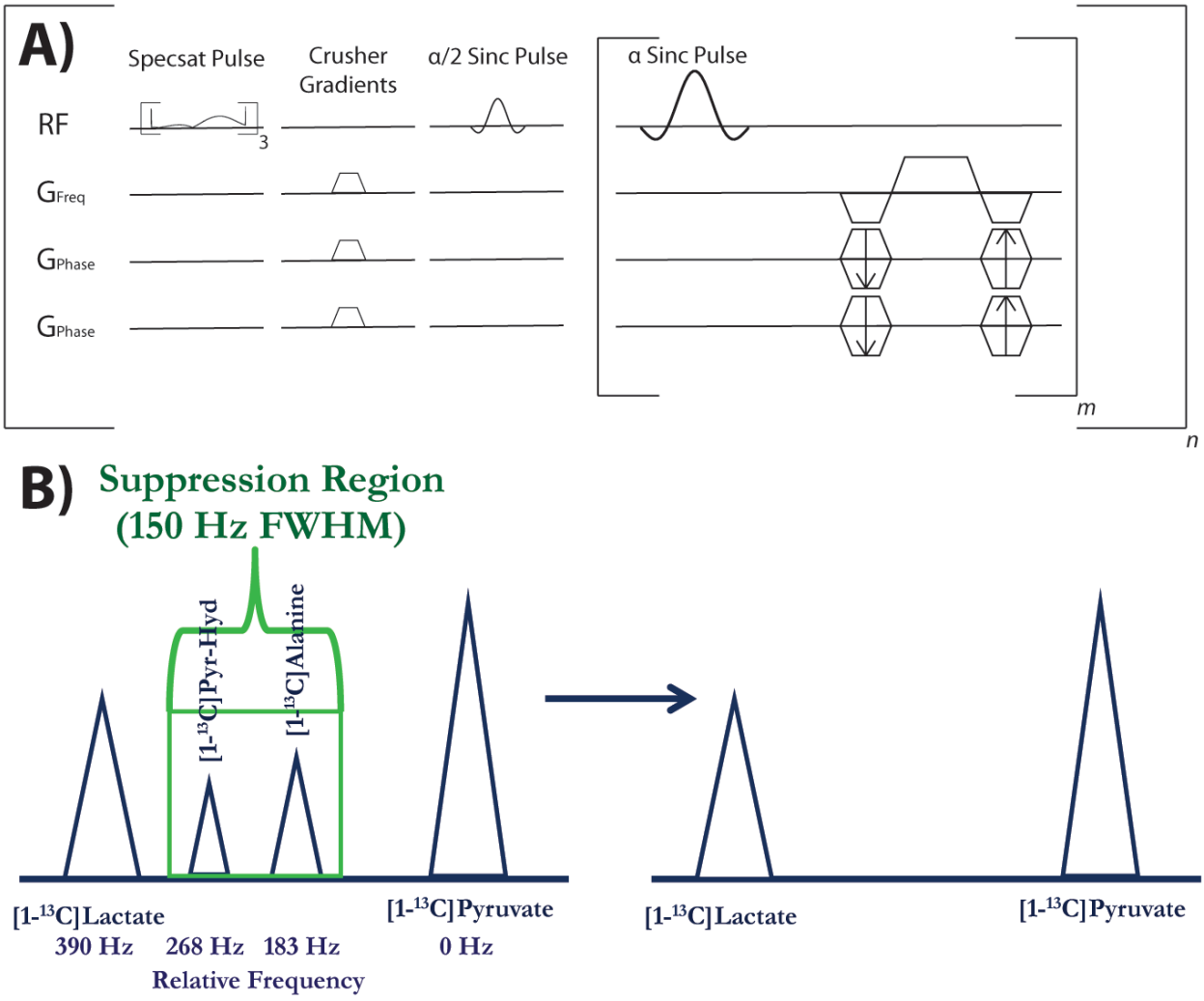

Figure 5.1: *Depiction of pulse sequence and spectral suppression region.* ***(A)*** *Pulse sequence diagram for the 3D bSSFP sequence used in these studies, with the spectral suppression (Specsat) pulses and crusher gradients being played out 3 times and one time, respectively, prior to imaging. The sequence consists of m phase encodes and n time-points, with the 2D version sequence featuring one fewer set of phase encode gradients for projection imaging.* ***(B)*** *The suppression region for the spectral suppression pulse is shown here in the context of suppressing the two main peaks between [1-^{13}C]pyruvate and [1-^{13}C]lactate, [1-^{13}C]alanine and [1-^{13}C]pyruvate-hydrate. The relative frequency separation in Hz for 3T is shown below the spectrum.*

Initial in vivo bSSFP images were acquired as coronal projections with slight variations in parameters for sequence optimization based on available SNR. These studies utilized the following general parameters: 12 x 6 cm^2 FOV, 60 x 30 matrix size for 2 x 2 mm^2 in-plane resolution (or 40 x 20 for 3 x 3 mm^2), progressive flip angle

scheme (increasing along time, constant within each time-point, similar to schemes described previously [143,144]), 6 time-points and 5 s temporal resolution for each metabolite, three suppression pulses played before each time-point as described above. An alternating center frequency scheme was utilized, with each metabolite acquired every 2.5 s. All scans started at 20 s after beginning of injection and 3 mL of 80mM [1-^{13}C]pyruvate was injected over 12 s via tail vein catheters in four different rats. A dynamic 2D CSI sequence was used for comparison in three rats of dynamic lactate-to-pyruvate ratios and had the following parameters: 8 cm coronal FOV, axial 8 cm slab, 8 x 8 matrix size leading to 10 x 10 mm^2 in-plane resolution, 5 kHz spectral width, 256 spectral points, TR of 76 ms, progressive flip angle scheme, 6 time-points.

Further optimized in vivo bSSFP images were also acquired as coronal projections and utilized the following general parameters: 12 x 6 cm^2 FOV, 40 x 20 for 3 x 3 mm^2 in-plane resolution, progressive flip angle scheme, 10-13 time-points and 3.6 s temporal resolution for each metabolite, three suppression pulses played before each time-point as described above. An alternating center frequency scheme was utilized, with each metabolite acquired every 1.8 s. All scans started at 5 s after beginning of injection and 3 mL of 80mM [1-^{13}C]pyruvate was injected over 12 s via tail vein catheters in three different rats.

3D rat studies utilized the following general parameters: 12 x 6 x 2 cm^3 FOV, 48 x 24 x 8 matrix size, progressive flip angle scheme, 10 time-points and 3.6 s temporal resolution for each metabolite, three suppression pulses played before each time-point as described above. 3D tumor-bearing mice studies utilized the following general parameters: 8 x 4 x 4 cm^3 FOV, 32 x 16 x 16 matrix size, 2.5 mm isotropic resolution,

progressive flip angle scheme, 10 time-points and 3.6 s temporal resolution for each metabolite, three suppression pulses played before each time-point as described above. An alternating center frequency scheme was utilized in both sets of studies, with each metabolite acquired every 1.8 s. Each 3D acquisition was undersampled along the time dimension by using a different undersampling pattern for each time-point, which resulted in 70% undersampling for rat studies and 75% undersampling for mouse studies. A local low rank plus sparse (LLR+S) algorithm was used for reconstruction, as described previously [145]. Briefly, the LLR+S algorithm enforces both low rank and sparse constraints via iterative soft thresholding on singular values and sparse coefficients to reconstruct undersampled dynamic MRI.

For anatomic reference, 3D bSSFP proton images (16 x 8 x 4.8 cm, 256 x 128 x 80, 5.1 ms TR, 50° flip angle) were acquired for rats and T_2-weighted fast spin echo proton (6 x 6 x 8 cm, 256 x 192 x 40, 7.6 s TR) images were obtained for mice.

5.3.4 Data and Statistical Analysis

All data was reconstructed and analyzed in Matlab (MathWorks, Natick, Massachusetts, USA), except the 2D CSI, which was analyzed in SIVIC [146], and carbon overlays onto proton data were done in Osirix [96]. Lactate-to-pyruvate ratios from the slab-selective MRS acquisitions were calculated from integration of summed (through time) magnitude spectra. Percentage suppression of alanine and pyruvate-hydrate was calculated based on percent change in alanine-to-pyruvate ratios and pyruvate-hydrate-to-pyruvate ratios, respectively. Statistical significance of the

comparison between acquisitions with and without spectral suppression were performed using a paired sample t-test in Matlab and a *P*-value < 0.05 was considered significant.

k_{PL} from the 2D bSSFP rat acquisitions was calculated using the model described in Maidens et al. [144], which assumes unidirectional conversion from pyruvate to lactate. Additionally, the T_1 of pyruvate was kept fixed during the fitting process, while allowing the T_1 of lactate and k_{PL} to vary. Since this model was designed based on acquisitions with single RF pulses, such as EPI, and to account for the use of variable flip angles during the bSSFP acquisition, a single effective flip angle was calculated for each time-point based on the depleted M_z magnetization during the imaging. This depletion was calculated by modeling the signal decay of the bSSFP sequence using the signal equation taken from Svensson et al. [23]:

$$M_{y,n} = M_{z,0} \sin\theta/2 \left((E_1 \cos\theta/2)^2 + (E_2 \sin\theta/2)^2\right)^{n/2}, \quad (5.1)$$

where E_1 = exp(-TR/T_1), E_2 = exp(-TR/T_2), n is the RF pulse number, and T_1 and T_2 assumed to be 25 s and 1.5 s, respectively. The $M_{z,0}$ was updated after every time-point to account for T_1 decay between successive time-points. The resulting effective flip angles for each time-point were calculated in the following manner:

$$\theta_{effective,i} = \arccos M_{z,post,i}/M_{z,pre,i}, \quad (5.2)$$

where i is the time-point, $M_{z,post}$ is the M_z immediately after completion of imaging and $M_{z,pre}$ is the M_z immediately before beginning of imaging. An initial SNR threshold based on pyruvate signal was used to filter out low SNR voxels.

5.4 Results

5.4.1 Spectral Suppression Pulse Phantom and in vivo Experiments

Figure 5.2 shows the effect of the spectral suppression pulse at different frequency offsets from the lactate resonance, with offsets ≥100 Hz showing no effect. The signal level at ≥100 Hz (Fig. 5.2A green line) equaled the signal level without any spectral saturation pulses played out (Fig. 5.2A dashed line). Therefore, with the offset set to 158 Hz in vivo, within the liver (Fig. 5.2B and 5.2C) and kidneys (Fig. 5.2D and 5.2E), the pulse was able to successfully suppress both alanine and pyruvate-hydrate without having an effect on the lactate or pyruvate resonances. Specifically, alanine and pyruvate-hydrate in the liver were suppressed by 89.0 ± 5.1% and 90.7 ± 4.1%, respectively, and by 84.1 ± 4.2% and 83.4 ± 5.3% in the kidneys, respectively. Calculations of lactate-to-pyruvate ratios showed no statistically significant difference between spectral suppression and no spectral suppression in either liver (P = 0.400) or kidney (P = 0.499), indicating no significant effect on quantitative analysis.

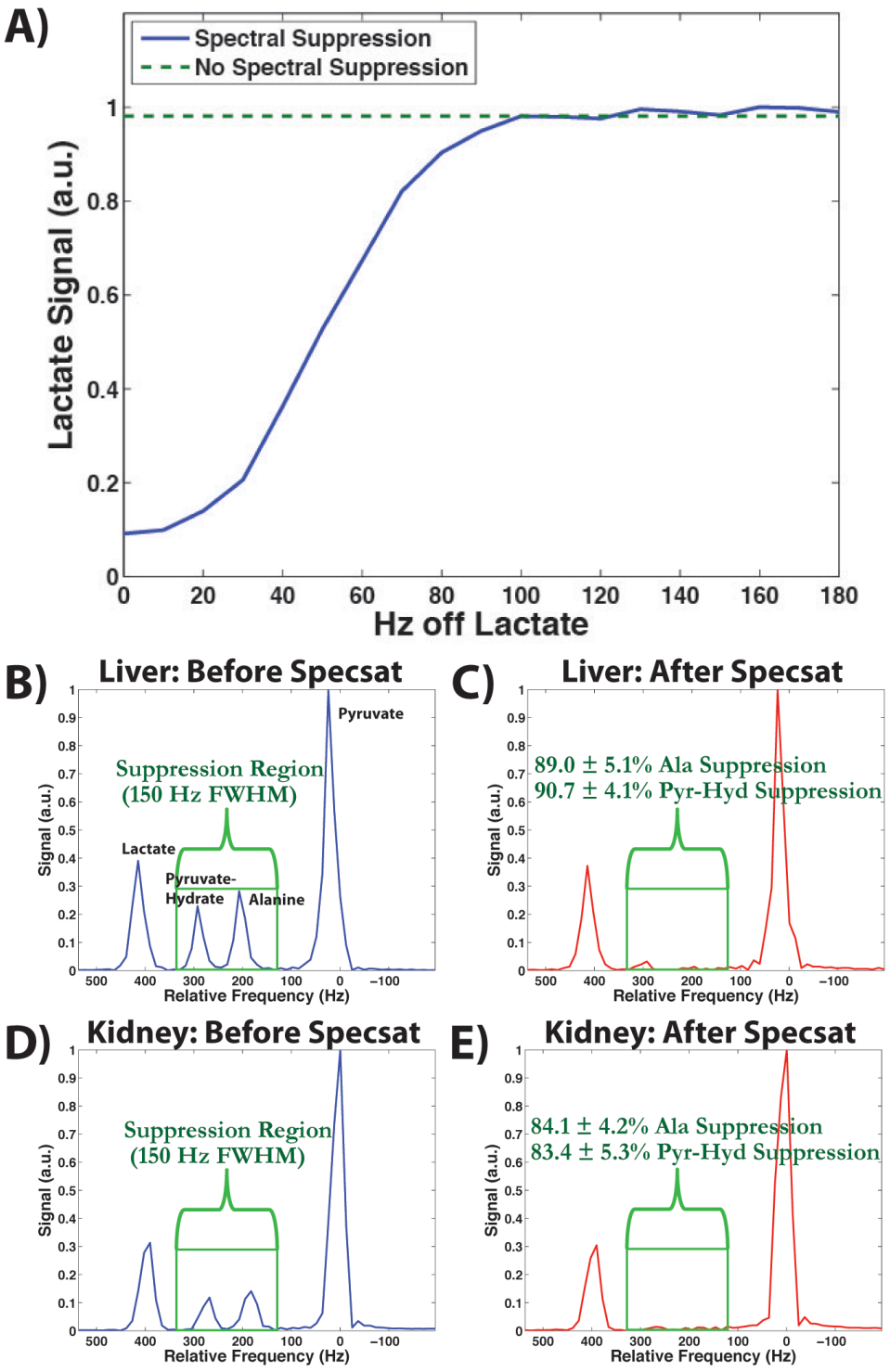

Figure 5.2: *Slab-selective MRS results of the spectral suppression pulse.* ***(A)*** *The effect of the spectral suppression pulse is shown as a function of the distance of the spectral suppression pulse center frequency to the lactate peak in a thermal phantom (blue line). At ≥100 Hz the pulse has no effect on the lactate peak, which is indicated by the green dashed line and is representative of the baseline lactate signal when no spectral*

suppression pulses are present. ***(B, C)*** *Parts B and C show the spectrum from a liver slab before and after the spectral suppression pulses, respectively. The pyruvate and lactate peaks remain unaffected, while the alanine and pyruvate-hydrate peaks are sufficiently suppressed by 89.0 ± 5.1% and 90.7 ± 4.1%, respectively.* ***(D, E)*** *Parts D and E show similar results from a kidney slab as parts B and C, with the alanine and pyruvate-hydrate peaks sufficiently suppressed by 84.1 ± 4.2% and 83.4 ± 5.3%, respectively.*

5.4.2 Excitation pulse train simulations

Figure 5.3 shows the simulations of the frequency response for a α = 60° 6.8 ms sinc pulse (TBW = 2) and 15.3 ms TR at ± 25 Hz around the on-resonance frequency (Fig. 5.3A) and 390 Hz off-resonance frequency (Fig. 5.3B). The simulations demonstrated successful individual selectivity of pyruvate and lactate with the bSSFP sequence as there was minimal excitation 390 ± 25 Hz off-resonance with this combination of pulse width, time-bandwidth, and TR. The [^{13}C]urea phantom results (Fig. 5.3C and 5.3D) matched the simulations, having ~100:1 selectivity. Additionally, based on the suppression percentages detailed previously, the simulations of the bSSFP signal response near alanine and pyruvate-hydrate, and the relative production of each compound based on the slab-selective MRS, the signal contribution of those resonances in the image amounted to <5%.

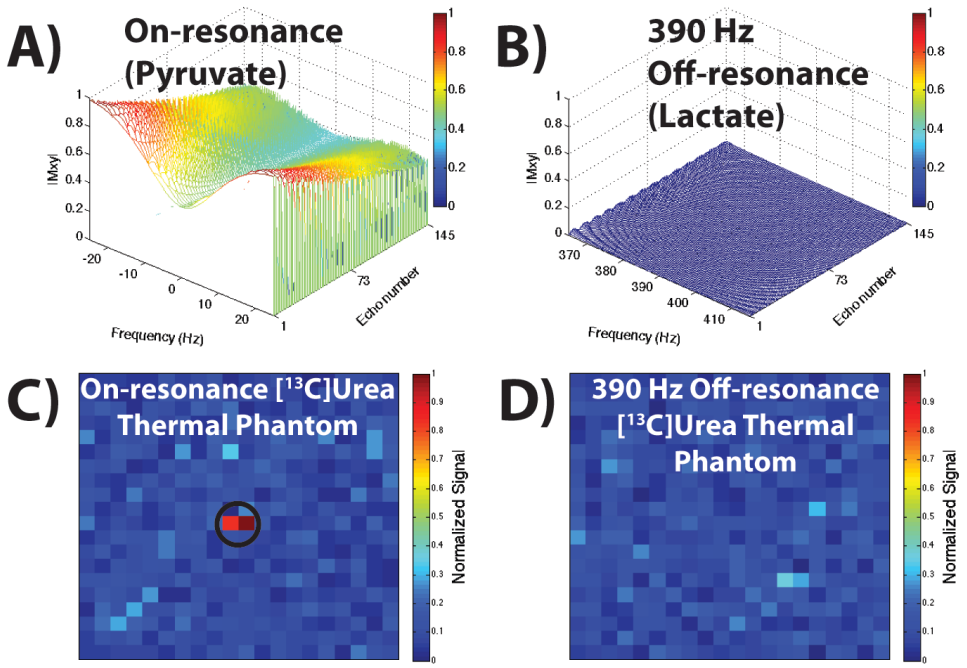

Figure 5.3: *Simulated and experimental bSSFP signal responses**. (A, B)** Simulations of a α = 60° 6.8 ms sinc pulse (TBW = 2) with a 15.3 ms TR. Part A shows the frequency response on-resonance, i.e. when the transmit frequency is set to pyruvate, and part B shows the frequency response 390 Hz off-resonance, i.e. at the lactate resonance. Part B shows negligible excitation 390 ± 25 Hz off-resonance for this pulse width, TBW, and TR, indicating no contamination of the pyruvate image with lactate signal (and vice-versa when the transmit frequency is set to lactate due to the symmetric frequency response). **(C, D)** Parts C and D show the thermal phantom acquisition with the aforementioned pulse and TR, with the on-resonance and off-resonance responses matching the simulations in parts A and B.*

5.4.3 2D bSSFP Imaging and Comparison to 2D CSI

Figure 5.4 shows successful acquisition of projection images of each metabolite from a 20 s scan start time at both 2 x 2 mm^2 (Fig. 5.4A-C) and 3 x 3 mm^2 (Fig. 5.4D-F) in-plane resolution, with clear visualization of biodistribution within the heart, vasculature, and kidneys at both resolutions. Comparison of the 2D CSI and bSSFP acquisitions revealed a similar increasing trend in normalized dynamic lactate-to-pyruvate ratios between the two acquisitions. This matching trend was seen for the first four time-points in each kidney (normalized to the highest lactate-to-pyruvate ratio for

each type of acquisition). The SNR was too low in the last two time-points of the bSSFP acquisition for accurate lactate-to-pyruvate calculation.

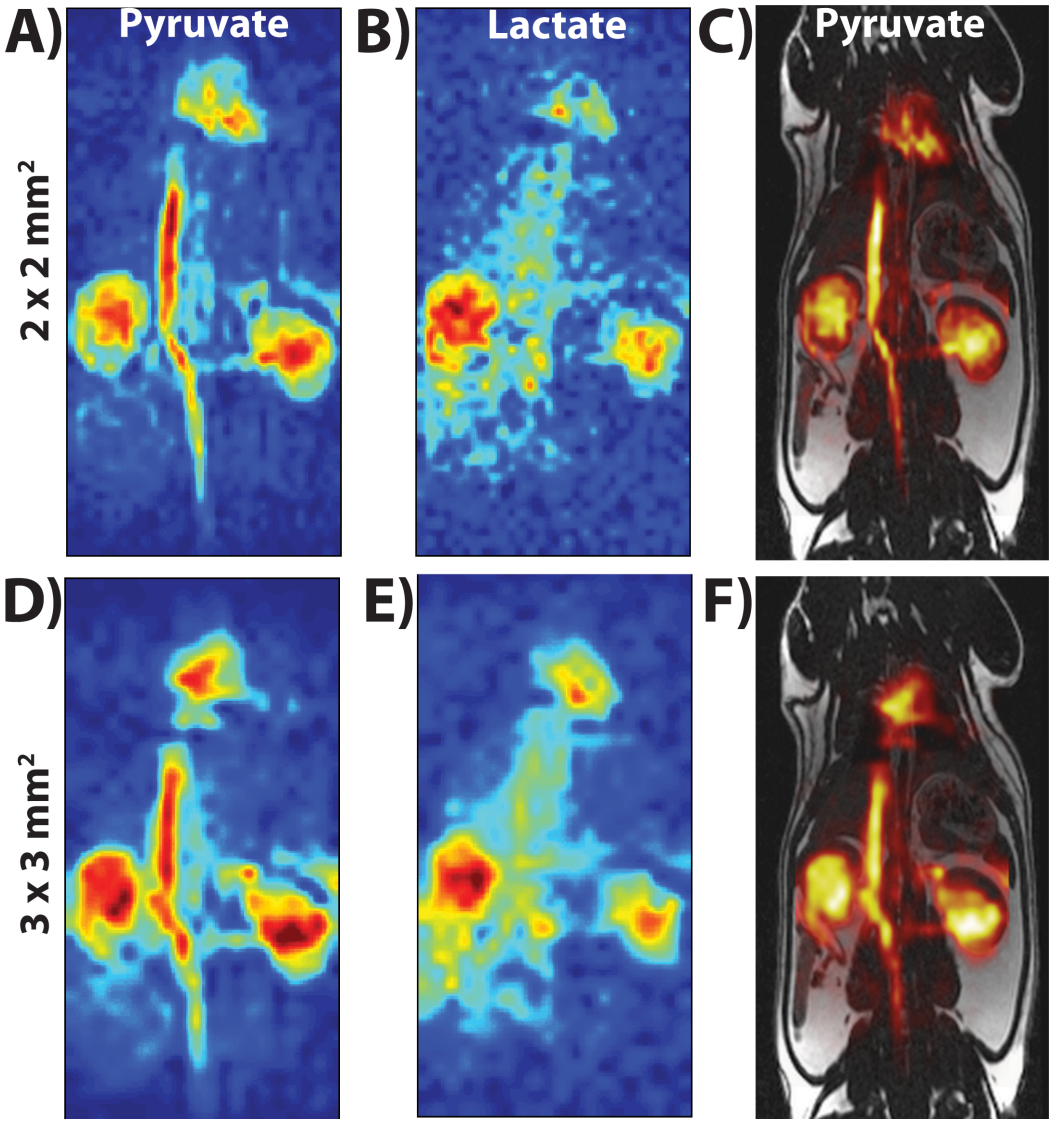

Figure 5.4: *Parts A (pyruvate) and B (lactate) show the first time-point (20 s after start of injection) of the 2 x 2 mm^2 in-plane resolution bSSFP acquisition, while parts D (pyruvate) and E (lactate) show the first time-point of the 3 x 3 mm^2 in-plane resolution bSSFP acquisition. Parts C and F show the carbon pyruvate image overlaid onto the ^{1}H anatomical image. The SNR (>40 for pyruvate and >15 for lactate) was high enough at both spatial resolutions to visualize pyruvate and lactate distribution in kidneys, heart, and vasculature. All images were zero-filled for display purposes.*

Figure 5.5A and Figure 5.5B show the time-points of pyruvate and lactate, respectively, from a 2D 3 x 3 mm^2 dynamic coronal projection (the scan started 5 s after

start of injection). The signal from pyruvate lasted throughout all the time-points, particularly in the kidneys, while lactate was present for approximately 22 s before the SNR became too low for visualization. Figure 5.5C shows the resulting k_{PL} map, with the resulting values matching up well with literature values for healthy rat kidneys ($k_{PL} \approx 0.013\ s^{-1}$) and vasculature ($k_{PL} \approx 0.004\ s^{-1}$) [147]. Figure 5.5D shows the AUC_{lac}/AUC_{pyr} map, with the trend of AUC ratio values agreeing well with the k_{PL} values based on qualitative analysis, such as the heart and vasculature having relatively lower AUC ratios and k_{PL}, with kidneys and liver being relatively higher [46,148].

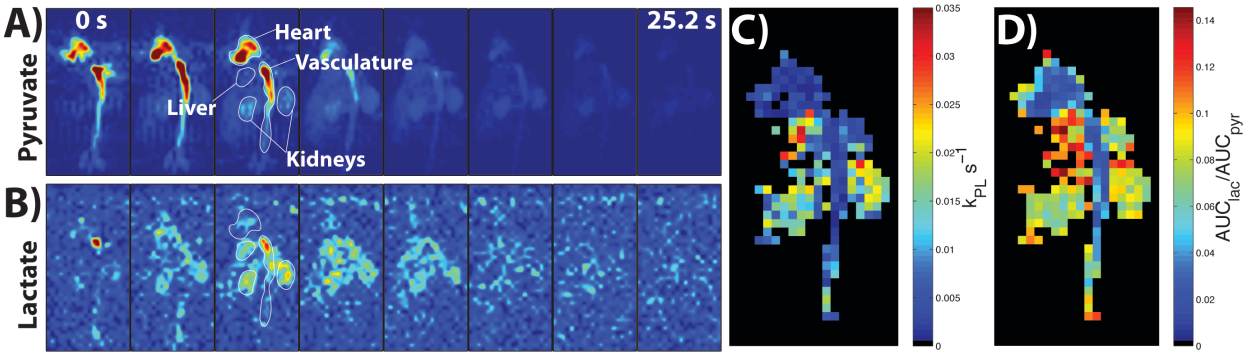

Figure 5.5: *Parts A and B show the resulting images of pyruvate and lactate, respectively, from all the time-points of the 2D dynamic coronal projection scan, which started at 5 s after the start of injection (represented by the 0 s in the first time-point). The SNR was high enough to visualize heart, vasculature, and kidneys for both metabolites, with the pyruvate signal lasting in the kidneys to the last time-point. Part C shows the resulting k_{PL} map with voxels in the vasculature and kidney featuring values that match up well with literature values ($k_{PL} \approx 0.013\ s^{-1}$ in kidneys and $k_{PL} \approx 0.004\ s^{-1}$ in vasculature* [147]*). Part D shows the AUC_{lac}/AUC_{pyr} map, with the AUC ratio values agreeing well with the k_{PL} values based on qualitative analysis, i.e. low heart and vasculature AUC ratio and k_{PL}, higher liver AUC ratio and k_{PL}, with kidneys being in between* [46]*. The images in parts A and B were zero-filled for display purposes, while k_{PL} and AUC ratio maps are at native resolution.*

5.4.4 3D bSSFP Imaging

Figure 5.6 shows all the slices from a representative time-point of each metabolite as well as the dynamics of the sum along the slice dimension from the 3D 2.5 mm isotropic dynamic acquisition for both rat kidney imaging (Fig. 5.6A for pyruvate

and 6B for lactate) and mouse tumor imaging (Fig. 5.6C for pyruvate and 6D for lactate). The SNR was high enough to again visualize the uptake, biodistribution and metabolism of both metabolites in both studies, although the signal appeared to last longer in the tumor-bearing mice, probably due to higher lactate production in the tumor region compared to a healthy rat.

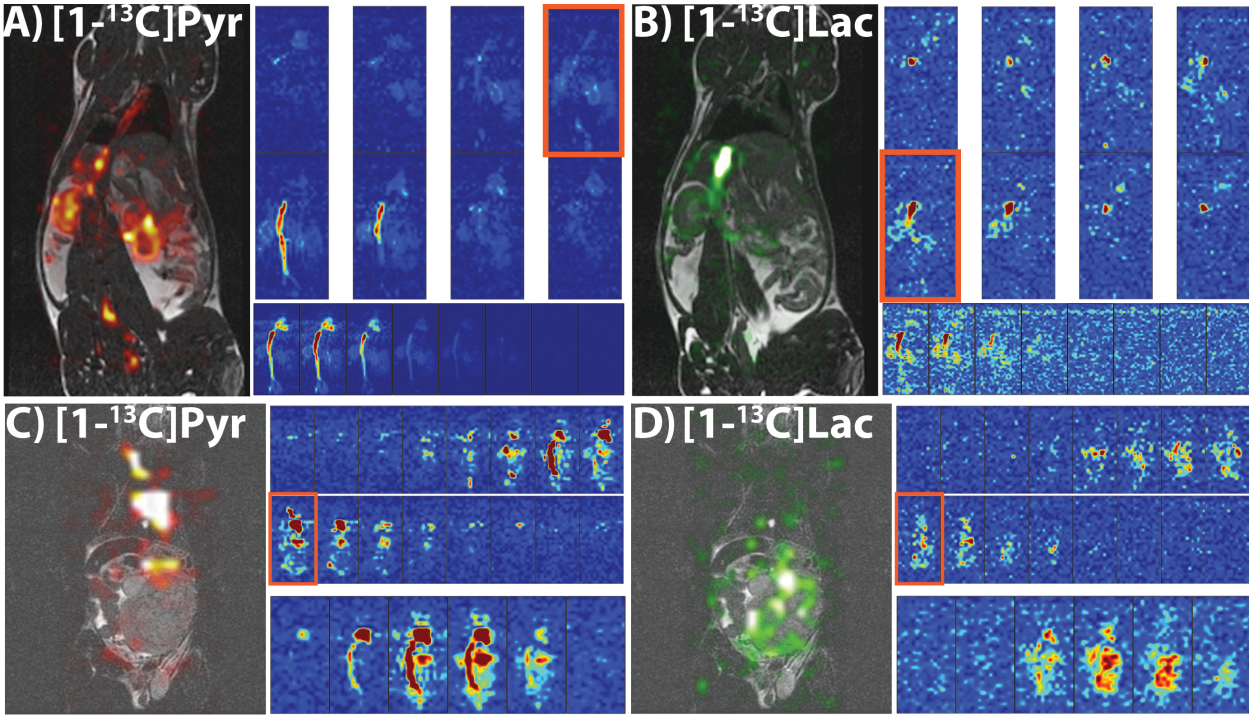

Figure 5.6: *In vivo 3D dynamic imaging results.* ***(A, B)*** *Results from a 3D dynamic 2.5 mm isotropic resolution acquisition in a healthy rat. Parts A and B are of pyruvate and lactate, respectively. Each part features a 3D view of a representative time-point (top two rows), all the time-points of the sum along the slice dimension (bottom row) showing how long the signal lasts for each metabolite, and a carbon overlay on a ^{1}H anatomical image of the slice outlined in orange. The SNR was also high enough in this acquisition to visualize each metabolite in heart, vasculature, and kidneys, although the signal doesn't last as long as the 2D coronal projections due to smaller voxel sizes, especially with lactate.* ***(C, D)*** *Results from a 3D dynamic 2.5 mm isotropic resolution acquisition in a tumor-bearing mouse. Parts C and D are of pyruvate and lactate, respectively, and the presented views are similar to parts A and B. The SNR was high enough to visualize the metabolites and heart and tumor, with the signal lasting longer than in the rats, potentially due to a larger production of lactate in the tumor. All images were zero-filled for display purposes.*

5.5 Discussion

We have developed an approach for high resolution dynamic [1-^{13}C]pyruvate and [1-^{13}C]lactate imaging with spectrally-suppressed bSSFP at a clinically relevant field strength of 3T and investigated its feasibility in preclinical studies. By combining spectral suppression pulses and an optimized pulse width and TBW, and TR, we were able to provide a framework for imaging [1-^{13}C]pyruvate and [1-^{13}C]lactate with the bSSFP sequence at higher spatiotemporal resolutions than previously done at 3T. Considering the challenge of controlling the bSSFP frequency response around the tight spectral spacing of resonances in the [1-^{13}C]pyruvate system, reducing the problem to a two-peak system with the spectral suppression pulses was very advantageous. While in this study we ignored the contribution of bicarbonate because of a low effective flip angle based on the bSSFP signal response (~3°) and low SNR at the achieved spatial resolutions, additional spectral suppression pulses can be added to suppress bicarbonate during the acquisition.

The optimization of flip angle scheme, spatial resolution, and temporal resolution is a constant challenge with HP ^{13}C imaging due to the nonrecoverable magnetization decay. The parameters chosen for the initial studies presented here were designed for high spatial and temporal resolution with sufficient SNR for calculation of lactate-to-pyruvate ratios and k_{PL}. Thermal phantom studies demonstrated no effect on the lactate or pyruvate resonances directly when applying the suppression pulse. Based on the comparison to the 2D CSI data, the trend of calculated lactate-to-pyruvate ratio was similar over a 20 s temporal window before the lactate SNR was too small for quantitative analysis. Similarly, the 3D rat data showed the capability of obtaining high

resolution 3D isotropic images of both pyruvate and lactate, but was again limited in lactate SNR over the course of the full temporal window. Acquisitions of high spatiotemporal resolution data can be limited by lactate production in the region of interest, in this case the kidneys. Conversely, the 3D TRAMP data provided higher lactate SNR in the tumor region, reflecting more lactate production. Imaging of produced lactate in healthy rat kidneys is most likely restricted to 2D projection or slice-selective imaging with a high in-plane resolution to acquire adequate lactate SNR over the temporal window necessary for accurate quantitation of pyruvate to lactate conversion. Starting the scans at 5 s was shown to be a good delay to visualize uptake, distribution, and metabolism of pyruvate, with 20 s being slightly too late as the build-up of lactate was already considerable and affected subsequent parameter fitting.

Calculation of k_{PL} with the bSSFP sequence presents additional challenges due to multiple RF pulses needed for phase encoding and relatively longer acquisition times. The signal decay is therefore a combination of not only k_{PL} and T_1, but also effects from flow, B_0/B_1 inhomogeneity in the coil, and other metabolism, which may result in faster than anticipated signal decay. While all sequences have to deal with these effects in some fashion, bSSFP specifically is very challenging due to the frequency response, where deviation from the on-resonant conditions can result in considerable deviations from the intended flip angle scheme. The model used for calculating k_{PL} fitted both k_{PL} and lactate $T_{1,}$ with the resulting T_1's being considerably shorter than expected in the kidneys, i.e. in the range of ~3-10 s versus expected ~15-25 s, which could be explained by the aforementioned effects and may represent an aggregate signal decay term. While k_{PL} values agreed with the literature as discussed in Figure 5.5, the

relatively low calculated lactate T_1 may indicate a modification to the model needs to be made to incorporate bSSFP signal decay for more accurate calculation of these parameters.

Recently acquired data in human cancer patients with a 5T GE SpinLab system offers promising results for high spatiotemporal imaging of pyruvate and lactate due to increased polarization, higher injection doses, larger organs, and, in some cases, higher lactate production [61–63]. Based on the banding artifacts seen in Figure 5.3A due to the 15.3 ms TR, future work will focus on incorporating an improved selective RF pulse design [149] for better off-resonance sensitivity and shorter pulse widths in the bSSFP readout. Initial simulations suggest the feasibility of an optimized ~2 ms pulse width and ~7 ms TR, which would cut the imaging time by half and improve SNR due to the shorter effective echo time. Utilizing a linear ramp preparation scheme [25,28] can also reduce off-resonance sensitivity, and allow imaging of other produced metabolites, such as bicarbonate.

Chapter 6: Simultaneous Imaging of Hyperpolarized [2-^{13}C]Pyruvate, [1-^{13}C]Lactate, and [^{13}C,$^{15}N_2$]Urea with the bSSFP Sequence at 3T

6.1 Abstract

The bSSFP sequence provides high spatiotemporal resolution for hyperpolarized ^{13}C imaging, but is limited in imaging multiple closely spaced resonances, such as metabolically-active compounds, due to banding artifacts. The goal of this study was to develop a framework for imaging [2-^{13}C]pyruvate, [1-^{13}C]lactate, and [^{13}C,$^{15}N_2$]urea simultaneously at 3T to visualize biodistribution, metabolism, and perfusion. Two different acquisition methods were tested, with the pulse width, time-bandwidth, and repetition time optimized for imaging either two or all three of the compounds. Sub-second 3D 2.5 mm isotropic images of each compound was acquired with 3.6 s temporal resolution in vivo, allowing calculations of blood flow, perfusion, and apparent metabolism. The framework presented here shows the capability for dynamic high resolution volumetric hyperpolarized bSSFP imaging of metabolically-active and perfusion based compounds simultaneously on a clinical MR scanner.

6.2 Introduction

Recent advances in hyperpolarized ^{13}C imaging via dissolution dynamic nuclear polarization (DNP) has enabled characterization of metabolism and perfusion simultaneously in various diseases [31,33,59]. Pyruvate and urea have been the most commonly used probes for reporting on metabolism and perfusion in preclinical models

[41,54], respectively, with successful translation of pyruvate into patients in recent clinical trials [60–64]. Because of the limited lifetime of the probes due to T_1 decay and metabolism, different rapid imaging and spectroscopic sequences have been developed, including MRSI with compressed sensing [5,41], spiral MRSI [43], and echo planar imaging [65,150]. Each of these sequences has excellent spectral resolution, but suffers from relatively low spatial resolution.

The balanced steady-state free precession (bSSFP) sequence has been shown to provide the highest SNR per unit time and has been applied to hyperpolarized ^{13}C to obtain high spatiotemporal resolution images [21,27,28,66]. However, due to potential banding artifacts, this sequence has an off-resonance profile that is difficult to manage [21,22,28]. This makes the spectral selectivity necessary for imaging [1-^{13}C]pyruvate and urea simultaneously very challenging to achieve at clinically relevant field strengths, since the resonances are located close to each other. Various approaches have been combined with the bSSFP sequence to image multiple resonances simultaneously, but each has their own drawbacks [28], with few being implemented at clinical field strengths, especially for high resolution 3D dynamic acquisitions. Ideally, for straightforward bSSFP acquisitions of multiple compounds simultaneously on clinical scanners, resonances should be spaced far enough apart to have a repetition time (TR) lower than ~12-15 ms, allowing better control over both the on- and off-resonance profiles within a large frequency range, such as 25 Hz.

Hyperpolarized [2-^{13}C]pyruvate and [1-^{13}C]lactate may provide indirect information on metabolism via biodistribution and uptake by analyzing the dynamics of both [2-^{13}C]pyruvate and [1-^{13}C]lactate in a fashion similar to PET imaging.

Furthermore, both compounds have been imaged at a high spatiotemporal resolution previously with the bSSFP sequence and can be treated as single resonances due to the negligible contribution of metabolized products to the signal of interest [66]. Due to the large frequency difference between [2-^{13}C]pyruvate and [1-^{13}C]lactate at 3T (~22.7 ppm or 729 Hz), both compounds can be simultaneously imaged with the bSSFP sequence for high resolution with the proper pulse width and repetition time. In addition, to obtain perfusion information, [^{13}C,$^{15}N_2$]urea can be added due to urea resonating far enough from both [1-^{13}C]lactate (~19.6 ppm or 630 Hz) and [2-^{13}C]pyruvate (~42.3 ppm or 1359 Hz) (Figure 6.1A) to still achieve a relatively short TR.

The goal of this project was to demonstrate the novel feasibility of imaging both [2-^{13}C]pyruvate/[^{13}C,$^{15}N_2$]urea simultaneously and [2-^{13}C]pyruvate/[1-^{13}C]lactate/[^{13}C,$^{15}N_2$]urea simultaneously at 2.5 mm isotropic resolution and <6 s temporal resolution with the bSSFP sequence at 3T. A RF pulse width and time-bandwidth and TR were carefully chosen for each set of co-polarized compounds to selectively excite one compound at a time while subsequently frequency switching to acquire all compounds in one acquisition. For comparison, co-polarized [2-^{13}C]pyruvate/[^{13}C,$^{15}N_2$]urea was also acquired with a “multi-band” encoding method [52,140] that features a long TR, but does not feature any temporal offset for acquisition of each compound (as is required for frequency switching). This study demonstrated the potential for imaging metabolically active and perfusion reporting compounds simultaneously with the bSSFP sequence at a high spatiotemporal resolution.

6.3 Methods

6.3.1.Hyperpolarization

Stock solutions of all compounds used in this study ([2-^{13}C]pyruvate, [1-^{13}C]lactate, [^{13}C,$^{15}N_2$]urea,) were prepared as described previously (cite my paper). The co-polarization procedure was done as follows: [^{13}C,$^{15}N_2$]urea was loaded into the sample cup and quickly frozen via immersion in liquid nitrogen. [2-^{13}C]Pyruvic acid was then loaded on top of the [^{13}C,$^{15}N_2$]urea layer and also frozen via liquid nitrogen. [1-^{13}C]Lactic acid was then loaded on top of the previous two layers and frozen prior to immediate loading into the HyperSense polarizer (Oxford Instruments, Abingdon, UK) operating at 3.35 T and 1.35 K for ~1 hour (no [1-^{13}C]lactic acid was added to pyruvic acid/urea co-polarizations). The compounds were then dissolved in appropriate media: 4.5 mL of 80 mM NaOH/40 mM Tris buffer for the pyruvic acid/urea co-polarization, resulting in 80 mM [2-^{13}C]pyruvate and 80 mM [^{13}C,$^{15}N_2$]urea; 4.5 mL of 160 mM NaOH/40 mM Tris buffer for the pyruvic acid/lactic acid/urea co-polarization, resulting in 80 mM [2-^{13}C]pyruvate (hereafter referred to as C_2-pyruvate), 80 mM [1-^{13}C]lactate (hereafter referred to as C_1-lactate), and 80 mM [^{13}C,$^{15}N_2$]urea (hereafter referred to as urea).

6.3.2 Animal Handling

All animal studies were done under protocols approved by the University of California San Francisco Institutional Animal Care and Use Committee (IACUC). Isoflurane (1.5%, 1 L/min O_2) was used to anesthetize all animals. Throughout the duration of the experiments, animals were placed in a supine position on a heated pad.

Normal Sprague-Dawley rats and transgenic adenocarcinoma of mouse prostate (TRAMP) mice were used in these studies. After polarization and dissolution, each of the compounds were injected into the animal via tail vein catheters: ~3 mL over 12 s for each rat and ~500 μL over 15 s for the mouse.

6.3.3 Pulse Sequence and Hardware

All experiments were performed on a 3T GE MR750 clinical scanner (GE Healthcare, Waukesha, WI) using dual-tuned $^{1}H/^{13}C$ transceiver birdcage radiofrequency coils that had either an inner diameter of 5 cm for mice or an inner diameter of 8 cm for rats. All acquisitions used a custom bSSFP sequence with two phase encoding dimensions for dynamic high resolution imaging. For each time-point, α/2-TR/2 preparation pulses were played for signal stabilization, and α-TR-α/2-TR/2 flip back pulses were played at the end of imaging to store the magnetization along the longitudinal axis.

6.3.4 Comparison of acquisition schemes

Two Sprague-Dawley rats were initially used for comparison of the frequency switching (hereafter referred to as method 1) and the multiband encoding (hereafter referred to as method 2) methods with co-polarized C_2-pyruvate+urea (Figure 6.1B). Both methods were acquired with a 50° flip angle, after a 25° preparatory pulse (no slice select gradients), 2.5 mm isotopic resolution, 6 s temporal resolution for each compound, 10 dynamic time-points for a total scan time of 60 s, with the scans started at 15 s after the beginning of injection. The different experimental parameters were as

follows: (1) 24 x 24 x 8 matrix size, 2 ms pulse with a TBW of 2, TR of 6.8 ms, and readout bandwidth (rBW) of 15.625 kHz; (2) 48 x 24 x 8 matrix size, 1.6 ms pulse with a TBW of 4, TR of 21.9 ms, and rBW of 2.824 kHz. Both phantom and *in vivo* experiments were acquired using partial Fourier acquisition, with only ¾ of the phase encodes acquired, and reconstructed as described previously. Simulations depicting the on-resonance and off-resonance profiles for each method were performed prior to imaging using the parameters just described to optimize the pulse width and TR.

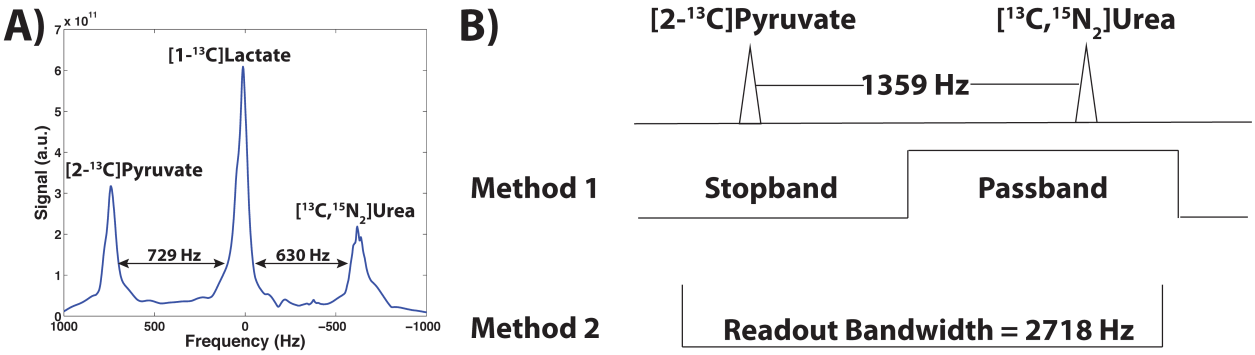

Figure 6.1: *(A) Spectrum showing relative resonance frequency of each compound at 3T in vivo. (B) Depiction of each method as related to the acquisition of [2-^{13}C]pyruvate and [^{13}C,^{15}N$_2$]urea and associated parameters for Sprague-Dawley rat imaging. Method 1 shows each compound placed into a passband or stopband based on the TR and center frequency chosen, with the center frequency alternating to acquire both compounds. Method 2 is multi-band encoding, whereby each compound is separated into different frequency bands for spatial encoding after the readout bandwidth is made larger than conventional imaging.*

6.3.5 Using frequency switching to image C_2-pyruvate+C_1-lactate+urea

To image C_2-pyruvate+C_1-lactate+urea simultaneously, method 1 was initially employed with the following parameters: variable flip angle (constant across a time-point, increasing across all time-points) after a α/2 preparatory pulse (no slice select gradients), 24 x 24 x 8 matrix size, 4 ms pulse with a TBW of 2, TR of 9.5 ms, and rBW of 15.625 kHz, 2.5 mm isotopic resolution, 4.5 s temporal resolution for each compound, 10 dynamic time-points for a total scan time of 45 s, undersampling along the time

dimension resulting in 70% undersampling for rat studies and 75% undersampling for mouse studies, with the scans starting at either 5 (five Sprague-Dawley rats and four TRAMP mice) or 15 s (two Sprague-Dawley rats) after the beginning of injection. Undersampled data was reconstructed using the LLR+S method as described in prior chapters. Simulations for this set of parameters were also performed prior to imaging as described above.

Anatomic references for all studies were acquired as follows: 3D bSSFP proton images (16 x 8 x 4.8 cm, 256 x 128 x 80, 5.1 ms TR, 50° flip angle) were acquired for rats and T_2-weighted fast spin echo proton (6 x 6 x 8 cm, 256 x 192 x 40, 7.6 s TR) images were obtained for mice. All data was reconstructed and analyzed in Matlab (MathWorks, Natick, Massachusetts, USA), and carbon overlays onto proton data were done in Osirix (Pixmeo, Bemex, Switzerland) [96].

6.3.6 Data Analysis

To calculate perfusion, F (mL/mL/s), for TRAMP tumor data, a simplified single-compartment model [151] was used, represented by the following differential equation:

$$\frac{dC_{tissue}(t)}{dt} = F * C_{plasma}(t) - R_1 * C_{tissue}(t) \qquad (6.1)$$

where C_{tissue} is the substrate concentration (MR signal/mL), C_{plasma} is the arterial input function (AIF) (MR signal/mL), and R_1 is equal to a combination of $1/T_{1,Substrate}$ and reverse perfusion (and includes contribution of metabolism for C_2-pyruvate and C_1-lactate [41]). The solution to the differential equation,

$$C_{tissue}(t) = (1 - v_b) * F * exp(-t * R_1) \otimes C_{plasma}(t) + v_b * C_{plasma}(t), \quad (6.2)$$

which includes a blood volume v_b term (mL/mL), was used to fit substrate dynamic curves via nonlinear least squares in Matlab. To calculate perfusion, F_T, for rat kidney data, a separable compartment model [152,153] was used, represented by the following sets of equations:

$$C_A(t)' = C_A(t-\tau) \quad (6.3)$$

$$C_{plasma}(t) = (1/T_P) * \exp(-t/T_P) \otimes C_A(t)' \quad (6.4)$$

$$C_{tissue}(t) = V_P * C_{plasma}(t) + F_T * \exp(-t/T_P) \otimes C_{plasma}(t), \quad (6.5)$$

where $C_A(t)'$ is the shifted AIF, $C_{plasma}(t)$ is the subsequently dispersed AIF, $C_{tissue}(t)$ is the substrate concentration, F_T is the tubular flow, V_P is the plasma volume, T_P is a combination of the mean transit time of the tracer in plasma and $T_{1,Substrate}$ (and includes contribution of metabolism for C_2-pyruvate and C_1-lactate), T_T is a combination of the mean transit time of the tracer in tubular compartments and $T_{1,Substrate}$ (and includes contribution of metabolism for C_2-pyruvate and C_1-lactate), and τ is the delay to account for shift and dispersion of AIF. To account for partial volume-effects, arterial input size was corrected as described previously [52]. Flip angle corrections for variable flip angle schemes were performed using the method described in Chapter 5 (section 5.3.4).

6.4 Results

6.4.1 Simulations/Phantoms

Figure 6.2 depicts the on-resonance (Fig. 6.2A) and off-resonance (Fig. 6.2B) frequency response of the excitation pulse train simulations for imaging co-polarized C_2-pyruvate+urea using method 1 with the parameters described above. The simulations demonstrated successful individual selectivity of C_2-pyruvate and urea with the bSSFP

sequence as there was minimal excitation 1359 ± 25 Hz off-resonance. The hyperpolarized urea phantom results (Fig. 6.2C and 6.2D) matched the simulations, having ~100:1 selectivity. Figure 6.3 depicts the on-resonance (Fig. 6.3A) and off-resonance (Fig. 6.3B) frequency response for imaging co-polarized C_2-pyruvate+urea using method 2 with the parameters described above. The frequency responses match up on-resonance and 1359 Hz off-resonance, indicating equivalent responses of both species during the multi-band readout.

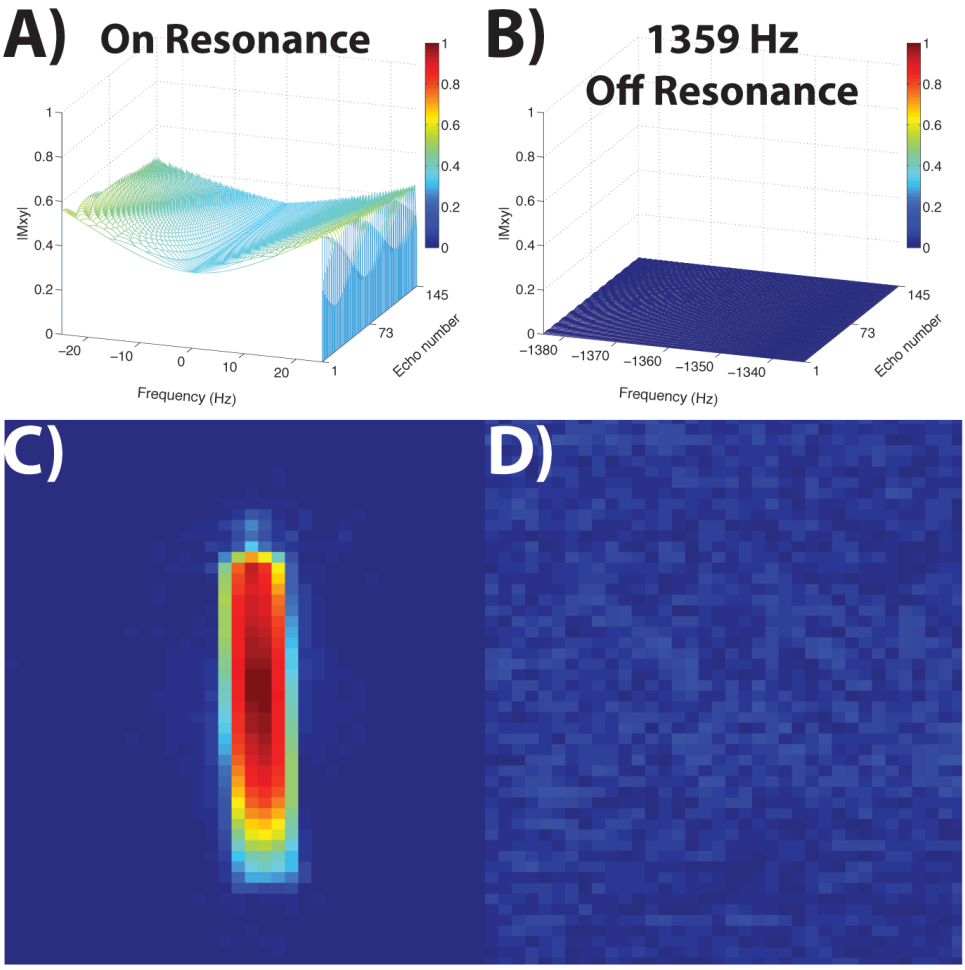

Figure 6.2: *Simulations of Method 1 showing on-resonance selective excitation (A) and 1359 Hz off-resonance negligible excitation (B) for an α=50° flip angle. The hyperpolarized phantom results in parts C and D match up with the simulations in part A and B, respectively.*

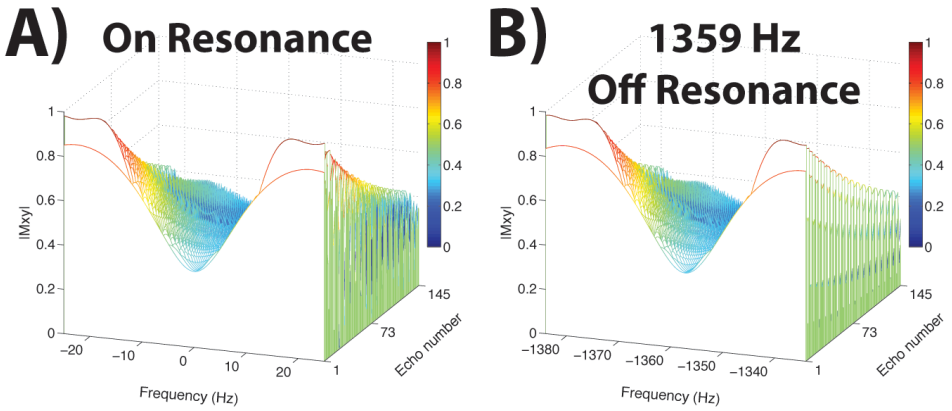

Figure 6.3: *Simulations of Method 2 showing equivalent responses for on-resonance (A) and 1359 Hz off-resonance (B) for an α=50° flip angle.*

Figure 6.4 depicts on-resonance (Fig. 6.4B) and off-resonance (Fig. 6.2A and 6.2C) frequency response for imaging of co-polarized C_2-pyruvate+C_1-lactate+urea using method 1 with the parameters described above. Similar to Figure 6.2, the simulations and associated hyperpolarized phantom results (Fig. 6D-F) demonstrated individual selectivity of all three species within ± 25 Hz.

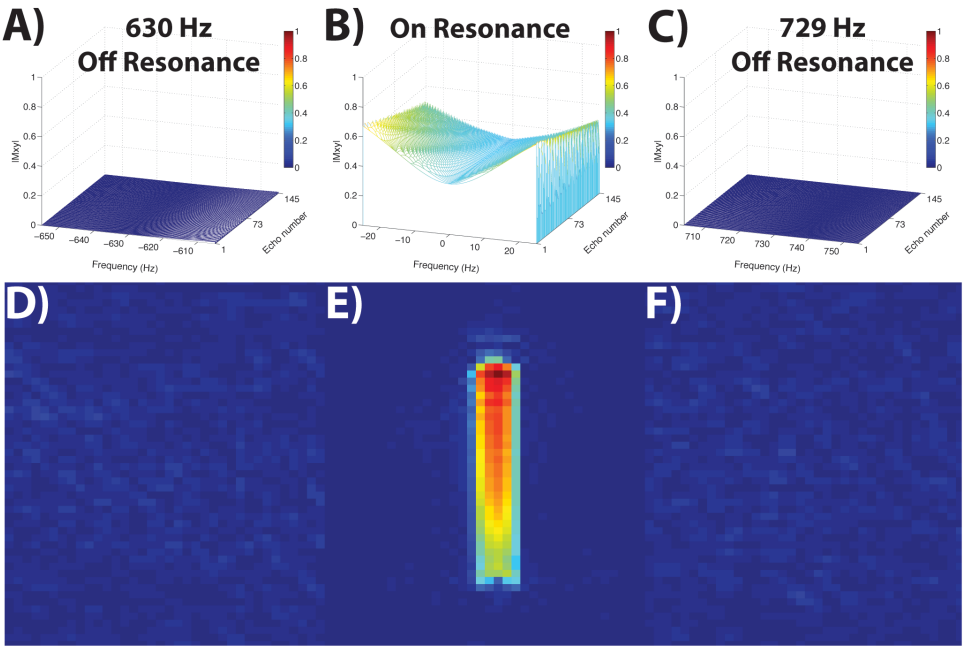

Figure 6.4: *Simulations of an extension of Method 1 for three resonances, showing on-resonance selective excitation (B), 630 Hz off-resonance negligible excitation (A), and*

729 Hz off-resonance negligible excitation (C) for an α=50° flip angle. The hyperpolarized phantom results in parts E, D and F match up with the simulations in part B, A, and C, respectively.

6.4.2 C_2-pyruvate+Urea Co-polarization

Figure 6.5 displays the 3D view of C_2-pyruvate and urea from the first time-point of successful acquisitions in a healthy rat using methods 1 and 2. Both methods had high enough SNR to visualize uptake and biodistribution of each probe within the kidneys. Both methods also displayed similar dynamics over the course of the ten time-points, although the SNR was low in the latter half of the acquisition due to use of a high constant flip angle. However, due to the long TR necessary for multi-band encoding, and the consequent banding artifacts seen in Figure 6.3, method 1 was determined to be advantageous for 3D imaging.

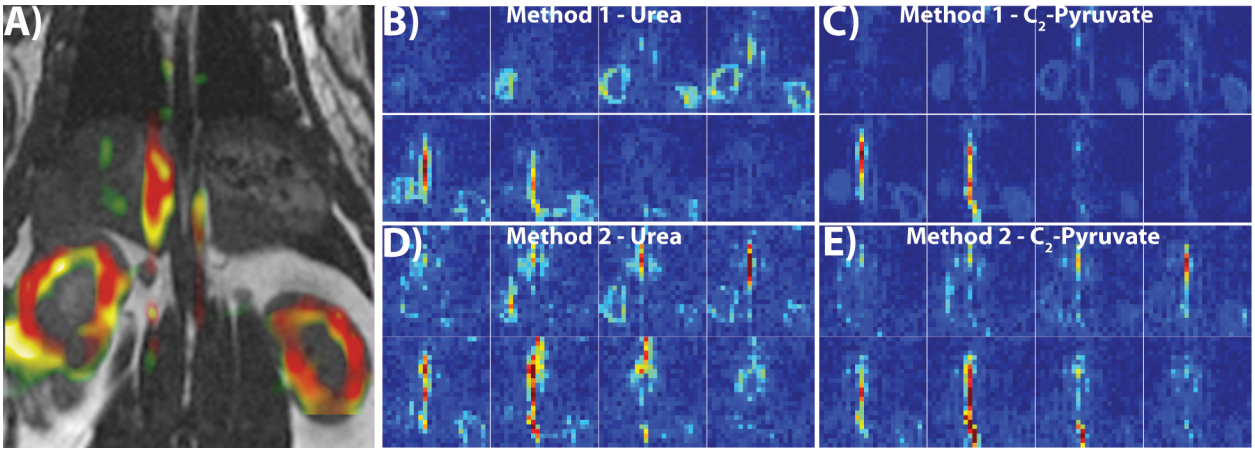

Figure 6.5: *The first time-point of each method for urea and pyruvate is presented here next to the proton image of slice 5 (outlined in orange on carbon images), with method 1 on top and method 2 on the bottom. The proton image also features the carbon overlay of method 2, with urea in green and pyruvate in red. Both methods successfully demonstrated dynamic uptake of each compound within kidneys and vasculature at 2.5 mm isotropic resolution for multiple time-points.*

6.4.3 C_2-pyruvate+C_1-lactate+Urea Co-polarization

Figures 6.6 and 6.7 show the dynamics of urea, C_1-lactate, and C_2-pyruvate in a representative slice (outlined in black in a 3D view) in a Sprague-Dawley rat and tumor-bearing mouse, respectively, along with a carbon overlay on a proton image of a urea time-point to the left. Uptake and biodistribution in kidneys, heart, and vasculature can be seen along multiple time-points for each compound in both animals, while uptake and biodistribution in the tumor can also be seen in the mouse along multiple time-points for all compounds. Figures 6.8 and 6.9 show perfusion and mean transit times/apparent T_1's in a Sprague-Dawley rat and tumor-bearing mouse, respectively. Urea showed the highest perfusion and mean transit times/apparent T_1's, while C_2-pyruvate showed the lowest, owing to metabolism to short T_1 compounds during perfusion and within the kidneys and tumor. C_1-lactate showed the values in between the other two compounds, owing to lower metabolism.

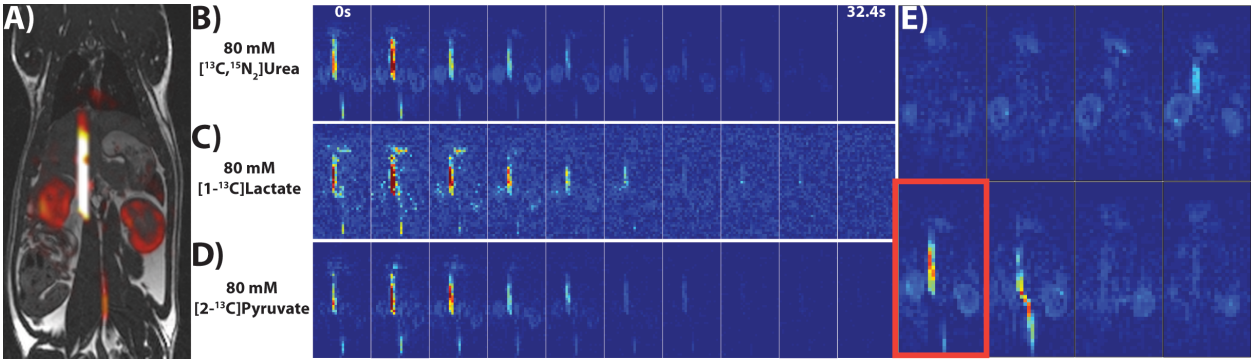

Figure 6.6: *Dynamics of urea (B), C_1-lactate (C), and C_2-pyruvate (D) in a representative slice (outlined in orange) in a Sprague-Dawley rat. Uptake and biodistribution in heart, vasculature, and kidneys can be seen along multiple time-points for all compounds. A carbon overlay on a proton image of a urea time-point can also be seen to the left (A). 3D view of the fourth time-point of urea, showing uptake and biodistribution in kidneys, heart, and vasculature can also be seen to the right (E).*

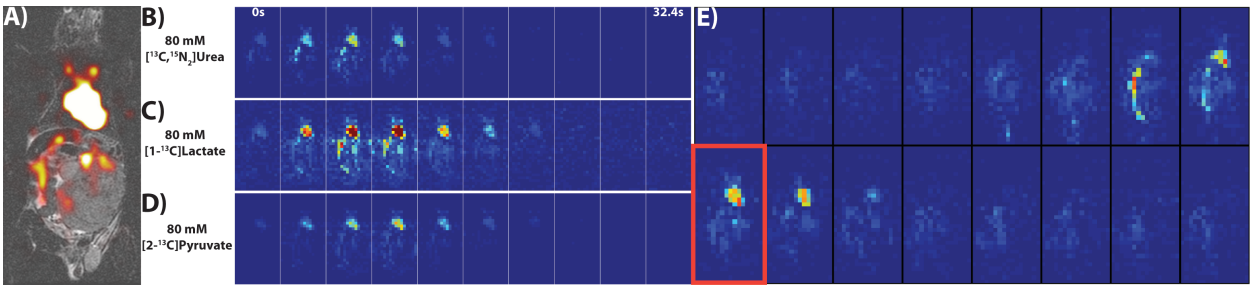

Figure 6.7: *Dynamics of urea (B), C_1-lactate (C), and C_2-pyruvate (D) in a representative slice (outlined in orange) in a tumor-bearing mouse. Uptake and biodistribution in heart, vasculature, and tumor can be seen along multiple time-points for all compounds. A carbon overlay on a proton image of a urea time-point can also be seen to the left (A). 3D view of the fourth time-point of urea, showing uptake and biodistribution in kidneys, tumor, heart, and vasculature can also be seen to the right (E).*

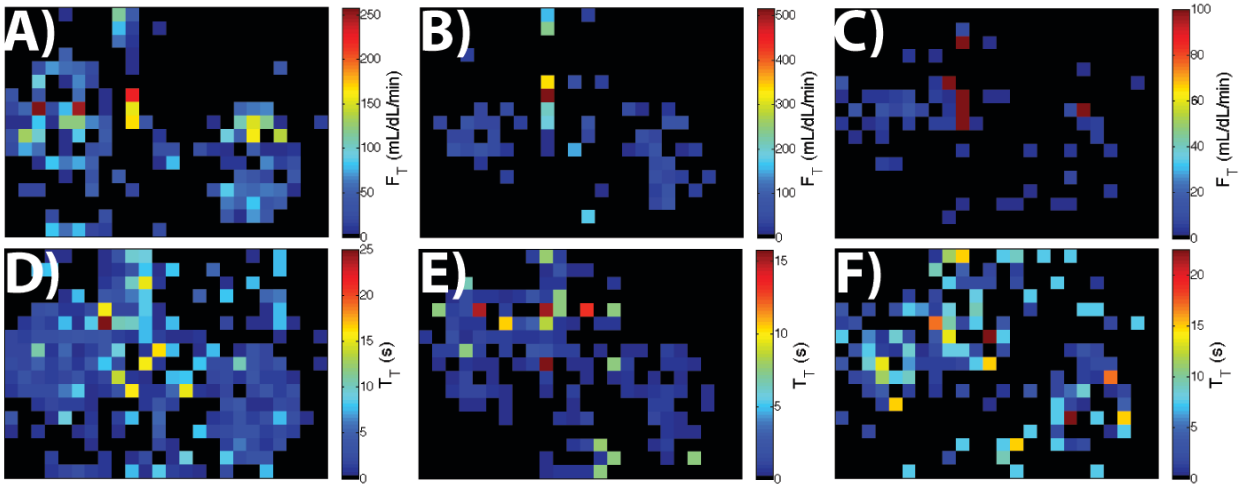

Figure 6.8: *Perfusion (F_T) and transit time of the tracer in tubular compartments (T_T) of urea (A,D), C_1-lactate (B,E), and C_2-pyruvate (C,F) in rat kidneys. The maps are shown as the average along the slice dimension. Urea showed the highest perfusion in the kidneys and relatively long transit times, while C_2-pyruvate showed the lowest values, owing to metabolism during the perfusion process, as well as metabolism in the kidneys. C_1-lactate demonstrated values in between C_2-pyruvate and urea, likely due to lower metabolism.*

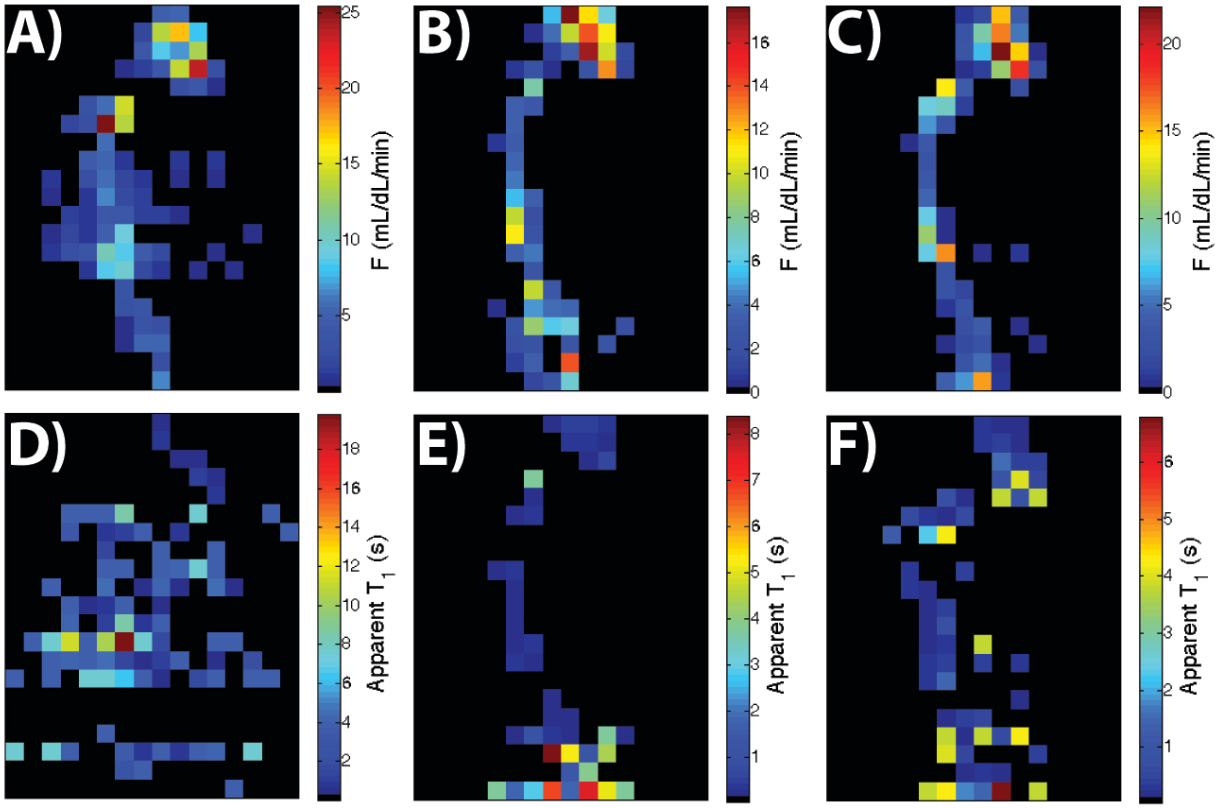

Figure 6.9: *Perfusion (F) and apparent T_1 or decay constant of urea (A,D), C_1-lactate (B,E), and C_2-pyruvate (C,F) in a tumor-bearing mouse. The maps are shown as the average along the slice dimension. Urea showed the highest perfusion in the tumor and short apparent T_1, while C_2-pyruvate showed the lowest values, owing to metabolism during the perfusion process, as well as metabolism in the tumor. C_1-lactate featured the values in between C_2-pyruvate and urea, likely due to lower metabolism.*

6.5 Discussion

We have developed an approach for simultaneously imaging metabolic changes (C_2-pyruvate and C_1-lactate) and perfusion (urea) at high spatiotemporal resolution at 3T using the bSSFP sequence. This approach was successfully investigated in preclinical models, with visualization of all three compounds in kidneys, heart, vasculature and tumor. Multiple methods were presented that each provided certain advantages towards dynamic selective imaging of multiple compounds.

The two methods evaluated here, frequency switching (method 1) and multi-band encoding (method 2), both successfully provided 2.5 mm isotropic dynamic imaging of C_2-pyruvate and urea. The main advantage of the multi-band encoding method is the ability to obtain all compounds at the exact same time, i.e. without any temporal shifts, which could help improve correlations between any quantification of each compound, such as correlation between metabolism and perfusion, or compounds that exist in equilibrium, such as bicarbonate and CO_2 for pH imaging [47]. However, as Figure 6.3 shows, the banding artifacts were severe for this method when acquiring 2.5 mm isotropic images due to the long TR required, which occurred due to the long low bandwidth readout (17.6 ms). This method works well for imaging multiple compounds with large chemical shift differences [52], although the chemical shift difference used here (1359 Hz) still required a >20 ms TR, which is undesirable for going to higher spatial resolutions, or imaging compounds that resonate close together. Therefore, the frequency switching method was utilized for imaging all three compounds simultaneously.

The advantages of the frequency switching method compared to the multi-band method include larger possible FOVs, higher achievable spatial resolutions, and less susceptibility to banding artifacts, as evidenced by Figures 6.2 and 6.4. With TRs of 6.8 ms (C_2-pyruvate+urea co-polarization) and 9.5 ms (C_2-pyruvate+C_1-lactate+urea co-polarization), the off-resonance response was relatively smoother. Furthermore, the scan time per volume per compound was also much shorter, leading to increased SNR due to the shorter effective echo time. While there exists a temporal offset between

compounds with this method, if the scan time is fast enough, then the offset can be neglected during data analysis.

The calculation of perfusion and associated parameters for each compound in vivo showed the prospective of quantitative assessment with C_2-pyruvate and C_1-lactate for apparent metabolism and urea for perfusion. Comparing the R_1 and T_T of urea versus C_2-pyruvate and C_1-lactate within the tumor-bearing mice and rats, respectively, combined with the perfusion information from each compound, may indicate areas of perfusion and metabolism correlations or mismatches. Relatively lower R_1's and T_T's for C_2-pyruvate and C_1-lactate would indicate metabolic conversion to shorter T_1 compounds, such as C_2-lactate/C_2-alanine, which would be reflected in lower apparent T_1's, and consequently higher R_1's and lower T_T's. These differences are more readily apparent with C_2-pyruvate in cancer due to the presumed higher rate of metabolism, although this can also be seen in the aorta and heart. Monitoring the decay of these metabolic probes in this fashion would be analogous to FDG PET, where the kinetic modeling accounts for FDG metabolism via phosphoprylation by hexokinase [154]. Starting the scans at 5 s was shown to be a good delay to visualize uptake and biodistribution of urea, as well as metabolism of C_2-pyruvate and C_1-lactate.

Future work will focus on incorporating more selective RF pulses [149] for better off-resonance sensitivity and shorter pulse widths in the bSSFP readout. This would shorten the imaging time, improve SNR due to the reduced effective echo time, allow for increased temporal resolution, and further improve modeling with more time-points. Additionally, incorporating a linear ramp preparation scheme [25,28] could further help reduce off-resonance sensitivity.

Chapter 7: Summary and Conclusions

7.1 Summary

Chapter 3 focused on the development of a high resolution bSSFP sequence for 2D T_2 mapping and 3D imaging of multiple HP ^{13}C compounds at 3T. High resolution (1 x 1 mm^2 to 2.5 x 2.5 mm^2) coronal T_2 maps of [1-^{13}C]lactate, [1-^{13}C]pyruvate, [2-^{13}C]pyruvate, and [^{13}C,$^{15}N_2$]urea were initially acquired in both healthy rats and tumor-bearing mice to examine the distribution of T_2 values within the anatomy and for optimization of the subsequent 3D acquisitions. The 3D 1.5-2 mm isotropic single time-point acquisitions revealed biodistribution and uptake of each compound within rat kidneys, vasculature, and heart, as well as within the tumor in tumor-bearing mice. Addition of compressed sensing allowed dynamic 3D 1.5 mm isotropic imaging of tumors at 2 s temporal resolution. These studies indicated the ability to achieve high spatiotemporal HP ^{13}C imaging on a clinical strength scanner in both 2D and 3D, as well as at a single time-point and multiple time-points.

Chapter 4 details an expansion of the work described in Chapter 3 by developing and incorporating a local low rank plus sparse (LLR+S) reconstruction for dynamic undersampled HP ^{13}C bSSFP acquisitions. Retrospective simulations indicated the combination of low rank and sparse reconstructions allowed for additional acceleration and better performance compared to low rank and sparse reconstructions individually. Prospective 3D acquisitions in healthy rats and a tumor-bearing mouse were undersampled by 60-75%, allowing for dynamic 3D 1.5-2 mm isotropic imaging at 2-5 s temporal resolutions. Accelerated T_2 mapping acquisitions were also reconstructed with the LLR+S reconstructions, with sub-millimeter (0.5 x 0.5 mm^2) in-plane resolution 2D

projections and 3D 1 mm isotropic resolutions achieved. These studies presented the LLR+S algorithm as a potential method to improve dynamic 3D bSSFP imaging and T_2 mapping, and can be readily combined with parallel imaging and translated into humans.

Chapter 5 focuses on adapting the bSSFP sequence for high spatiotemporal imaging of [1-^{13}C]pyruvate and produced [1-^{13}C]lactate at 3T. Spectral suppression pulses were utilized to suppress the alanine and pyruvate-hydrate resonances without affecting quantitation, thereby reducing the problem to a two-peak system. Optimized RF pulse width and TR were used to obtain both dynamic 2D projections and 3D volumes of both metabolites in healthy rat kidneys, heart, vasculature, and liver, as well as in a tumor of a tumor-bearing mouse. The results of this study demonstrated a developed framework for pyruvate metabolic imaging with the bSSFP sequence at a clinically relevant field strength.

Chapter 6 details an application of the bSSFP sequence to spectrally selective imaging of multiple HP ^{13}C compounds simultaneously at 3T. Two separate methods were investigated for imaging [2-^{13}C]pyruvate, [1-^{13}C]lactate, and [^{13}C,$^{15}N_2$]urea simultaneously. Successful 3D imaging of all three compounds in healthy rat kidneys, heart, and vasculature demonstrated a framework for high spatiotemporal acquisitions of both metabolic and perfusion probes simultaneously at a clinically relevant field strength with the bSSFP sequence.

Hyperpolarized ^{13}C imaging has grown immensely over the last decade, owing to its many advantages, including high SNR, rapid imaging, no background signal, lack of ionizing radiation, and metabolic and perfusion imaging capabilities for monitoring

disease progression. All the studies summarized here demonstrate the development and application of the bSSFP sequence to high spatiotemporal HP ^{13}C imaging of both metabolically active and inactive probes. With the clinical translation of this technology currently being investigated, the work presented here indicates the bSSFP sequence can be an integral part of the field going forward.

7.2 Translation of the bSSFP sequence into humans

As discussed previously in chapter 2, hyperpolarized ^{13}C imaging is currently being investigated for clinical value through Phase II trials. The main sequences currently are EPSI for spectroscopic imaging and EPI for metabolic-specific imaging since quantification of metabolism after injection of [1-^{13}C]pyruvate is one of the main goals for assessing disease with this technology. However, as illustrated in the preceding chapters, and particularly Chapter 5, the bSSFP sequence has the potential to provide relatively higher spatiotemporal resolution, both for metabolically active compounds and, and especially metabolically inactive compounds, such as urea, where spectral selectivity is not an issue and short TRs are possible. Adapting the sequence for patient-sized FOVs will be the next challenge and is briefly discussed here.

7.2.1 Spatiotemporal and flip angle considerations

Initial studies with the bSSFP sequence will focus on matching the current spatiotemporal resolution of the EPI sequence to gauge the current SNR feasible with the sequence and consequently the quantification that can be done with the resulting data. For example, in prostate cancer patients, the current multislice EPI parameters for [1-^{13}C]pyruvate and produced [1-^{13}C]lactate are as follows: 12.8 x 12.8 x 12.8 cm^3 FOV,

16 x 16 x 16 (i.e. 16 slices), 0.8 x 0.8 x 0.8 cm^3 (~0.5 cm^3) spatial resolution, 62.5 ms TR, 2 s temporal resolution, progressive flip angle scheme. Hypothetically, attempting to match those parameters for a fully sampled 3D bSSFP sequence would result in the following parameters: 12.8 x 12.8 x 12.8 cm^3 FOV, 16 x 16 x 16, 0.8 x 0.8 x 0.8 cm^3 (~0.5 cm^3) spatial resolution, ~2.2 ms optimized RF pulse width, ~7 ms TR, ~1.8 s total scan time per volume per metabolite, ~3.6 ms temporal resolution for each metabolite, progressive flip angle scheme.

The main immediate differences between the two sequences is the scan time for each metabolite, and consequently the temporal resolution, with the EPI being ~2-fold faster than the bSSFP. This may result in the ability to acquire more time-points based on the available magnetization. However, the bSSFP sequence is more SNR efficient, which may result in higher total SNR. The choice of flip angles is crucial here to maximize SNR efficiency and use the hyperpolarized magnetization efficiently. Initial simulations, coupled with results from a few initial studies, will aid in creating the optimal schemes that simultaneously use pyruvate and lactate magnetization effectively for SNR and quantification purposes. Additionally, the use of the optimized RF pulse design, as well as the addition of a linear ramp for the preparatory pulses, would improve off-resonance sensitivity and alleviate any banding artifacts that may arise when playing a progressive flip angle scheme.

In principle, bSSFP sequences should be able to achieve higher spatial resolution compared to other sequences, although dynamic HP ^{13}C studies make it more challenging because of the aforementioned need for efficient hyperpolarized magnetization usage. Using the prostate cancer setup from above as an example, going

to a 32 x 32 x 32 matrix size would directly result in 4x scan time, but 8x higher spatial resolution. However, while the SNR might be sufficient for the first few time-points, the signal would decay much faster, resulting in fewer time-points for quantification purposes. Due to the number of phase encodes needed for a 3D sequence, compressed sensing and parallel imaging would immensely benefit clinical HP ^{13}C studies.

7.2.2 Application of Compressed Sensing and Parallel Imaging

Image acceleration will be an important part of HP ^{13}C clinical studies going forward to improve the spatiotemporal resolution. Compressed sensing has already been applied as part of the Phase II trials for accelerating EPSI in prostate cancer, taking additional advantage of the sparsity of the HP ^{13}C spectrum. While the prostate cancer acquisitions employ a single channel coil, and thus are essentially restricted to compressed sensing for image acceleration, other Phase II trials are moving towards large multi-channel setups, such as a 16-channel phased-array for abdominal imaging, and a 32-channel coil for brain imaging. Therefore, acceleration via parallel imaging is a logical next step, with SAKE and ESPIRIT being two algorithms that would provide the best reconstructions. Furthermore, as described in chapter 2, combinations of compressed sensing and parallel imaging could provide further acceleration in these clinical setups.

Chapter 4 describes using a local low rank plus (LLR+S) algorithm for acceleration of bSSFP acquisitions, and can be directly integrated into a potential clinical setup. For example, if 4x acceleration were to be employed in the prostate

cancer setup with a hypothetical 32 x 32 x 32 matrix size (for ~0.06 cm^3 voxel sizes), then the scan time would equal the current fully sampled setup, while gaining 8x spatial resolution. Alternatively, merely accelerating the 16 x 16 x 16 setup would also prove beneficial since the scan time per volume would be lowered, as well as the effective echo time, which would provide increased SNR. Similarly, parallel imaging can be readily combined with the bSSFP sequence in a similar fashion as EPI, with some initial preclinical studies indicating the effectiveness of the SAKE algorithm for reconstruction. In general, the larger FOVs for clinical studies necessitate larger matrix sizes, which could allow for higher acceleration factors, akin to ^1H imaging.

References

[1] C.L. Swisher, Hyperpolarized ^{13}C Magnetic Resonance Spectroscopy: Probing Enzymatic Activity, Cellular Transport, and Oncogene Activation, 2014.

[2] D.W. McRobbie, E.A. Moore, M.J. Graves, M.R. Prince, MRI From Picture to Proton, 2nd ed., Cambridge University Press, New York, 2007.

[3] M. Lustig, D. Donoho, J.M. Pauly, Sparse MRI: The application of compressed sensing for rapid MR imaging, Magn. Reson. Med. 58 (2007) 1182–1195. doi:10.1002/mrm.21391.

[4] M. Lustig, D.L. Donoho, J.M. Santos, J.M. Pauly, Compressed sensing MRI: A look at how CS can improve on current imaging techniques, IEEE Signal Process. Mag. 25 (2008) 72–82. doi:10.1109/MSP.2007.914728.

[5] P.E.Z. Larson, S. Hu, M. Lustig, A.B. Kerr, S.J. Nelson, J. Kurhanewicz, J.M. Pauly, D.B. Vigneron, Fast Dynamic 3D MRSI with Compressed Sensing and Multiband Excitation Pulses for Hyperpolarized ^{13}C Studies, Magn. Reson. Med. 65 (2011) 610–619. doi:10.1016/j.biotechadv.2011.08.021.Secreted.

[6] M. Lustig, J.M. Santos, D. Donoho, J.M. Pauly, k-t SPARSE: high frame rate dynamic MRI exploiting spatio-temporal sparsity, Proc. Intl. Soc. Mag. Reson. Med. 14 2420. (n.d.).

[7] R. Otazo, D. Kim, L. Axel, D.K. Sodickson, Combination of compressed sensing and parallel imaging for highly accelerated first-pass cardiac perfusion MRI, Magn. Reson. Med. 64 (2010) 767–776. doi:10.1002/mrm.22463.

[8] M.T. Chu, R.E. Funderlic, R.J. Plemmons, Structured low rank approximation, Linear Algebra Appl. 366 (2003) 157–172. doi:10.1016/S0024-3795(02)00505-0.

[9] I. Markovsky, Structured low-rank approximation and its applications, Automatica. 44 (2008) 891–909. doi:10.1016/j.automatica.2007.09.011.

[10] T. Zhang, J.Y. Cheng, A.G. Potnick, R.A. Barth, M.T. Alley, M. Uecker, M. Lustig, J.M. Pauly, S.S. Vasanawala, Fast pediatric 3D free-breathing abdominal dynamic contrast enhanced MRI with high spatiotemporal resolution, J. Magn. Reson. Imaging. 41 (2015) 460–473. doi:10.1002/jmri.24551.

[11] T. Zhang, J.M. Pauly, I.R. Levesque, Accelerating parameter mapping with a locally low rank constraint, Magn. Reson. Med. 73 (2015) 655–661. doi:10.1002/mrm.25161.

[12] J. Trzasko, A. Manduca, Local versus Global Low-Rank Promotion in Dynamic MRI Series Reconstruction, in: Proc. Intl. Soc. Mag. Reson. Med. 19 4371., n.d.

[13] M. Dankova, P. Rajmic, R. Jirik, Acceleration of Perfusion MRI Using Locally Low-Rank Plus Sparse Model, in: Latent Var. Anal. Signal Sep., 2015: pp. 514–521. doi:10.1007/978-3-319-22482-4.

[14] P.J. Shin, P.E.Z. Larson, M. a. Ohliger, M. Elad, J.M. Pauly, D.B. Vigneron, M. Lustig, Calibrationless parallel imaging reconstruction based on structured low-rank matrix completion, Magn. Reson. Med. 970 (2013) 959–970. doi:10.1002/mrm.24997.

[15] Y. Feng, J.W. Gordon, P.J. Shin, C. von Morze, M. Lustig, P.E.Z. Larson, M.A. Ohliger, L. Carvajal, J. Tropp, J.M. Pauly, D.B. Vigneron, Development and testing of hyperpolarized ^{13}C MR calibrationless parallel imaging, J. Magn. Reson. 262 (2016) 1–7. doi:10.1016/j.jmr.2015.10.018.

[16] A. Deshmane, V. Gulani, M. a. Griswold, N. Seiberlich, Parallel MR imaging, J.

Magn. Reson. Imaging. 36 (2012) 55–72. doi:10.1002/jmri.23639.

[17] K.P. Pruessmann, M. Weiger, M.B. Scheidegger, P. Boesiger, SENSE: Sensitivity encoding for fast MRI, Magn. Reson. Med. 42 (1999) 952–962. doi:10.1002/(SICI)1522-2594(199911)42:5<952::AID-MRM16>3.0.CO;2-S.

[18] M.A. Griswold, P.M. Jakob, R.M. Heidemann, M. Nittka, V. Jellus, J. Wang, B. Kiefer, A. Haase, Generalized Autocalibrating Partially Parallel Acquisitions (GRAPPA), Magn. Reson. Med. 47 (2002) 1202–1210. doi:10.1002/mrm.10171.

[19] R. Otazo, E. Candès, D.K. Sodickson, Low-rank plus sparse matrix decomposition for accelerated dynamic MRI with separation of background and dynamic components, Magn. Reson. Med. 73 (2015) 1125–1136. doi:10.1002/mrm.25240.

[20] M. Uecker, P. Lai, M.J. Murphy, P. Virtue, M. Elad, J.M. Pauly, S.S. Vasanawala, M. Lustig, ESPIRiT - An eigenvalue approach to autocalibrating parallel MRI: Where SENSE meets GRAPPA, Magn. Reson. Med. 71 (2014) 990–1001. doi:10.1002/mrm.24751.

[21] K. Scheffler, S. Lehnhardt, Principles and applications of balanced SSFP techniques, Eur. Radiol. 13 (2003) 2409–2418. doi:10.1007/s00330-003-1957-x.

[22] O. Bieri, K. Scheffler, Fundamentals of balanced steady state free precession MRI, J. Magn. Reson. Imaging. 38 (2013) 2–11. doi:10.1002/jmri.24163.

[23] J. Svensson, S. Månsson, E. Johansson, J.S. Petersson, L.E. Olsson, Hyperpolarized ^{13}C MR angiography using trueFISP, Magn. Reson. Med. 50 (2003) 256–262. doi:10.1002/mrm.10530.

[24] P.W. Worters, B.A. Hargreaves, Balanced SSFP transient imaging using variable

flip angles for a predefined signal profile, Magn. Reson. Med. 64 (2010) 1405–1413. doi:10.1002/mrm.22541.

[25] P. Le Roux, Simplified model and stabilization of SSFP sequences, J. Magn. Reson. 163 (2003) 23–37. doi:10.1016/S1090-7807(03)00115-0.

[26] G.D. Reed, Novel Imaging Contrast Methods for Hyperpolarized ^{13}C Magnetic Resonance Imaging, 2014.

[27] G.D. Reed, C. von Morze, A.S. Verkman, B.L. Koelsch, M.M. Chaumeil, M. Lustig, S.M. Ronen, R.A. Bok, J.M. Sands, P.E.Z. Larson, Z.J. Wang, J.H.A. Larsen, J. Kurhanewicz, D.B. Vigneron, Imaging Renal Urea Handling in Rats at Millimeter Resolution using Hyperpolarized Magnetic Resonance Relaxometry, Tomography. 2 (2016) 125–137. doi:10.18383/j.tom2016.00127.

[28] H. Shang, S. Sukumar, C. Von Morze, R.A. Bok, I. Marco-Rius, A. Kerr, G.D. Reed, E. Milshteyn, M.A. Ohliger, J. Kurhanewicz, P.E.Z. Larson, J.M. Pauly, D.B. Vigneron, Spectrally Selective Three-Dimensional Dynamic Balanced Steady-State Free Precession for Hyperpolarized C-13 Metabolic Imaging With Spectrally Selective Radiofrequency Pulses, Magn. Reson. Med. (2016). doi:10.1002/mrm.26480.

[29] K. Scheffler, On the transient phase of balanced SSFP sequences, Magn. Reson. Med. 49 (2003) 781–783. doi:10.1002/mrm.10421.

[30] A. Oppelt, R. Graumann, H. Barfuss, H. Fischer, W. Hartl, W. Schajor, FISP — a new fast MRI sequence, Electromedica. 54 (1986) 15–18. http://mri-q.com/uploads/3/2/7/4/3274160/oppelt_fisp_1986.pdf.

[31] J. Kurhanewicz, D.B. Vigneron, K. Brindle, E.Y. Chekmenev, A. Comment, C.H.

Cunningham, R.J. Deberardinis, G.G. Green, M.O. Leach, S.S. Rajan, R.R. Rizi, B.D. Ross, W.S. Warren, C.R. Malloy, Analysis of cancer metabolism by imaging hyperpolarized nuclei: prospects for translation to clinical research., Neoplasia. 13 (2011) 81–97. doi:10.1593/neo.101102.

[32] A. Comment, M.E. Merritt, Hyperpolarized Magnetic Resonance as a Sensitive Detector of Metabolic Function, Biochemistry. 53 (2014) 7333–7357. doi:10.1021/bi501225t.

[33] J.H. Ardenkjaer-Larsen, B. Fridlund, A. Gram, G. Hansson, L. Hansson, M.H. Lerche, R. Servin, M. Thaning, K. Golman, Increase in signal-to-noise ratio of > 10,000 times in liquid-state NMR., Proc. Natl. Acad. Sci. U. S. A. 100 (2003) 10158–10163. doi:10.1073/pnas.1733835100.

[34] S. Hu, P.E.Z. Larson, M. VanCriekinge, A.M. Leach, I. Park, C. Leon, J. Zhou, P.J. Shin, G. Reed, P. Keselman, C. Von Morze, H. Yoshihara, R. a. Bok, S.J. Nelson, J. Kurhanewicz, D.B. Vigneron, Rapid sequential injections of hyperpolarized [1-^{13}C]pyruvate in vivo using a sub-kelvin, multi-sample DNP polarizer, Magn. Reson. Imaging. 31 (2013) 490–496. doi:10.1016/j.mri.2012.09.002.

[35] H.-Y. Chen, Development and Translation of 3D Dynamic Hyperpolarized ^{13}C-MR Metabolic and Perfusion Imaging - From Mice to Patients, 2017.

[36] M.G. Vander Heiden, L.C. Cantley, C.B. Thompson, P. Mammalian, C. Exhibit, A. Metabolism, Understanding the Warburg Effect : Cell Proliferation, Science (80-.). 324 (2009) 1029. doi:10.1126/science.1160809.

[37] S.J. Kohler, Y. Yen, J. Wolber, a. P. Chen, M.J. Albers, R. Bok, V. Zhang, J.

Tropp, S. Nelson, D.B. Vigneron, J. Kurhanewicz, R.E. Hurd, In vivo ^{13}carbon metabolic imaging at 3T with hyperpolarized ^{13}C-1-pyruvate, Magn. Reson. Med. 58 (2007) 65–69. doi:10.1002/mrm.21253.

[38] M.L. Zierhut, Y.F. Yen, A.P. Chen, R. Bok, M.J. Albers, V. Zhang, J. Tropp, I. Park, D.B. Vigneron, J. Kurhanewicz, R.E. Hurd, S.J. Nelson, Kinetic modeling of hyperpolarized $^{13}C_1$-pyruvate metabolism in normal rats and TRAMP mice, J. Magn. Reson. 202 (2010) 85–92. doi:10.1016/j.jmr.2009.10.003.

[39] M.J. Albers, R. Bok, A.P. Chen, C.H. Cunningham, M.L. Zierhut, V.Y. Zhang, S.J. Kohler, J. Tropp, R.E. Hurd, Y.F. Yen, S.J. Nelson, D.B. Vigneron, J. Kurhanewicz, Hyperpolarized ^{13}C lactate, pyruvate, and alanine: Noninvasive biomarkers for prostate cancer detection and grading, Cancer Res. 68 (2008) 8607–8615. doi:10.1158/0008-5472.CAN-08-0749.

[40] A.P. Chen, W. Chu, Y.-P. Gu, C.H. Cunnhingham, Probing early tumor response to radiation therapy using hyperpolarized [1-^{13}C]pyruvate in MDA-MB-231 xenografts., PLoS One. 8 (2013) e56551. doi:10.1371/journal.pone.0056551.

[41] H.Y. Chen, P.E.Z. Larson, R.A. Bok, C. Von Morze, R. Sriram, R.D. Santos, J.D. Santos, J.W. Gordon, N. Bahrami, M. Ferrone, J. Kurhanewicz, D.B. Vigneron, Assessing prostate cancer aggressiveness with hyperpolarized dual-agent 3D dynamic imaging of metabolism and perfusion, Cancer Res. 77 (2017) 3207–3216. doi:10.1158/0008-5472.CAN-16-2083.

[42] A.A. Hurwitz, B.A. Foster, J.P. Allison, N.M. Greenberg, E.D. Kwon, The TRAMP mouse as a model for prostate cancer., Curr. Protoc. Immunol. Chapter 20 (2001) Unit 20.5. doi:10.1002/0471142735.im2005s45.

[43] J.M. Park, S. Josan, T. Jang, M. Merchant, R. Watkins, R.E. Hurd, L.D. Recht, D. Mayer, D.M. Spielman, Volumetric spiral chemical shift imaging of hyperpolarized [2-^{13}C]pyruvate in a rat c6 glioma model, Magn. Reson. Med. (2015). doi:10.1002/mrm.25766.

[44] Y.F. Yen, P. Le Roux, D. Mayer, R. King, D. Spielman, J. Tropp, K.B. Pauly, A. Pfefferbaum, S. Vasanawala, R. Hurd, T_2 relaxation times of ^{13}C metabolites in a rat hepatocellular carcinoma model measured in vivo using ^{13}C-MRS of hyperpolarized [1-^{13}C]pyruvate, NMR Biomed. 23 (2010) 414–423. doi:10.1002/nbm.1481.

[45] P.J. Shin, Z. Zhu, R. Camarda, R.A. Bok, A.Y. Zhou, J. Kurhanewicz, A. Goga, D.B. Vigneron, Cancer recurrence monitoring using hyperpolarized [1-^{13}C]pyruvate metabolic imaging in murine breast cancer model, Magn. Reson. Imaging. 43 (2017) 105–109. doi:10.1016/j.mri.2017.07.014.

[46] D.K. Hill, M.R. Orton, E. Mariotti, J.K.R. Boult, R. Panek, M. Jafar, H.G. Parkes, Y. Jamin, M.F. Miniotis, N.M.S. Al-Saffar, M. Beloueche-Babari, S.P. Robinson, M.O. Leach, Y.-L. Chung, T.R. Eykyn, Model Free Approach to Kinetic Analysis of Real-Time Hyperpolarized 13C Magnetic Resonance Spectroscopy Data, PLoS One. 8 (2013) e71996. doi:10.1371/journal.pone.0071996.

[47] F.A. Gallagher, M.I. Kettunen, S.E. Day, D.-E. Hu, J.H. Ardenkjær-Larsen, R. in ‘t Zandt, P.R. Jensen, M. Karlsson, K. Golman, M.H. Lerche, K.M. Brindle, Magnetic resonance imaging of pH in vivo using hyperpolarized 13C-labelled bicarbonate, Nature. 453 (2008) 940–943. doi:10.1038/nature07017.

[48] F.A. Gallagher, M.I. Kettunen, D.-E. Hu, P.R. Jensen, R. In ’t Zandt, M. Karlsson,

A. Gisselsson, S.K. Nelson, T.H. Witney, S.E. Bohndiek, G. Hansson, T. Peitersen, M.H. Lerche, K.M. Brindle, Production of hyperpolarized [1,4-$^{13}C_2$]malate from [1,4-$^{13}C_2$]fumarate is a marker of cell necrosis and treatment response in tumors., Proc. Natl. Acad. Sci. U. S. A. 106 (2009) 19801–19806. doi:10.1073/pnas.0911447106.

[49] M.M. Chaumeil, C. Najac, S.M. Ronen, Studies of Metabolism Using ^{13}C MRS of Hyperpolarized Probes, in: Methods Enzymol., 2015. doi:10.1016/bs.mie.2015.04.001.

[50] K.M. Brindle, S.E. Bohndiek, F.A. Gallagher, M.I. Kettunen, Tumor Imaging Using Hyperpolarized Resonance Spectroscopy ^{13}C Magnetic, Magn. Reson. Med. 66 (2011) 505–519. doi:10.1002/mrm.22999.

[51] C. Von Morze, P.E.Z. Larson, S. Hu, K. Keshari, D.M. Wilson, J.H. Ardenkjaer-Larsen, A. Goga, R. Bok, J. Kurhanewicz, D.B. Vigneron, Imaging of blood flow using hyperpolarized [^{13}C]urea in preclinical cancer models, J. Magn. Reson. Imaging. 33 (2011) 692–697. doi:10.1002/jmri.22484.

[52] C. Von Morze, R.A. Bok, G.D. Reed, J.H. Ardenkjaer-Larsen, J. Kurhanewicz, D.B. Vigneron, Simultaneous Multiagent Hyperpolarized ^{13}C Perfusion Imaging, Magn. Reson. Med. 72 (2014) 1599–1606. doi:10.1002/mrm.25071.

[53] G.D. Reed, C. Von Morze, R. Bok, B.L. Koelsch, M. Van Criekinge, K.J. Smith, H. Shang, P.E.Z. Larson, J. Kurhanewicz, D.B. Vigneron, High Resolution ^{13}C MRI With Hyperpolarized Urea: In Vivo T_2 Mapping and ^{15}N Labeling Effects, IEEE Trans. Med. Imaging. 33 (2014) 362–371.

[54] C. Von Morze, P.E.Z. Larson, S. Hu, H.A. Yoshihara, R.A. Bok, A. Goga, J.H.

Ardenkjaer-Larsen, D.B. Vigneron, Investigating tumor perfusion and metabolism using multiple hyperpolarized ^{13}C compounds: HP001, pyruvate and urea, Magn. Reson. Imaging. 30 (2012) 305–311. doi:10.1016/j.mri.2011.09.026.

[55] R.K. Jain, Normalizing tumor vasculature with anti-angiogenic therapy: a new paradigm for combination therapy., Nat. Med. 7 (2001) 987–989. doi:10.1038/nm0901-987.

[56] D.W. Siemann, The Unique Characteristics of Tumor Vasculature and Preclinical Evidence for its Selective Disruption by Tumor-Vascular Disrupting Agents, Cancer Treat. Rev. 37 (2012) 63–74. doi:10.1016/j.ctrv.2010.05.001.The.

[57] P.M. Nielsen, E.S.S. Hansen, T.S. Nørlinger, R. Nørregaard, L.B. Bertelsen, H.S. Jørgensen, C. Laustsen, Renal Ischemia and Reperfusion Assessment With Three-Dimensional Hyperpolarized ^{13}C,$^{15}N2$-Urea, Magn. Reson. Med. 76 (2016) 1524–1530. doi:10.1002/mrm.26377.

[58] E.S.S. Hansen, N.J. Stewart, J.M. Wild, H. Stødkilde-jørgensen, C. Laustsen, Hyperpolarized ^{13}C,$^{15}N_2$-Urea MRI for Assessment of the Urea Gradient in the Porcine Kidney, Magn. Reson. Med. 76 (2016) 1895–1899. doi:10.1002/mrm.26483.

[59] S.J. Nelson, J. Kurhanewicz, D.B. Vigneron, P.E.Z. Larson, A.L. Harzstark, M. Ferrone, M. van Criekinge, J.W. Chang, R. Bok, I. Park, G. Reed, L. Carvajal, E.J. Small, P. Munster, V.K. Weinberg, J.H. Ardenkjaer-Larsen, A.P. Chen, R.E. Hurd, L.-I. Odegardstuen, F.J. Robb, J. Tropp, J. a Murray, Metabolic imaging of patients with prostate cancer using hyperpolarized [1-^{13}C]pyruvate., Sci. Transl. Med. 5 (2013) 198ra108. doi:10.1126/scitranslmed.3006070.

[60] Z. Zhu, I. Marco-rius, M.A. Ohliger, L. Carvajal, J.W. Gordon, H. Chen, I. Park, P. Cao, P.J. Shin, E. Milshteyn, C. Von Morze, M. Ferrone, J.B. Slater, Z. Wang, P.E.Z. Larson, R. Aggarwal, R. Bok, J. Kurhanewicz, P. Munster, D.B. Vigneron, Hyperpolarized ^{13}C Dynamic Breath-held Molecular Imaging to Detect Targeted Therapy Response in Patients with Liver Metastases, in: Proc. Intl. Soc. Mag. Reson. Med. 25 1115., n.d.

[61] J.W. Gordon, H. Chen, P.E.Z. Larson, I. Park, M. Van Criekinge, E. Milshteyn, R. Bok, M. Ferrone, J.B. Slater, J. Kurhanewicz, D.B. Vigneron, Human Hyperpolarized C-13 MRI Using a Novel Echo-Planar Imaging (EPI) Approach, in: Proc. Intl. Soc. Mag. Reson. Med. 25 0728., n.d. doi:10.1002/MRM26123.4.

[62] H. Chen, P.E.Z. Larson, J.W. Gordon, R.A. Bok, M. Ferrone, M. Van Criekinge, L. Carvajal, R. Aggarwal, J.B. Slater, I. Park, E. Milshteyn, S.J. Nelson, J. Kurhanewicz, B. Daniel, Phase II Clinical Hyperpolarized 13C 3D-Dynamic Metabolic Imaging of Prostate Cancer using a B1-insensitive Variable Flip Angle Design, in: Proc. Intl. Soc. Mag. Reson. Med. 25 0725., n.d.

[63] K.L. Granlund, H.A. Vargas, S.K. Lyashchenko, P.J. Denoble, V. Laudone, J.A. Eastham, A. Ramon, M. Kennedy, D. Nicholson, Y.W. Guo, A. Chen, J. Tropp, H. Hricak, R. Kayvan, Utilizing hyperpolarized MRI in prostate cancer to assess metabolic dynamics and histopathologic grade, in: Proc. Intl. Soc. Mag. Reson. Med. 25 0727., n.d.

[64] D. Tyler, O. Rider, M. Dodd, A. Lau, A. Lewis, J. Miller, M. Peterzan, C. Trumper, S. Neubauer, Demonstrating the Randle Cycle In Vivo: Assessment of Physiological Alterations in Human Cardiac Metabolism Using Hyperpolarised ^{13}C

MR Spectroscopy, in: Proc. Intl. Soc. Mag. Reson. Med. 25 0726., n.d.

[65] J.W. Gordon, D.B. Vigneron, P.E.Z. Larson, Development of a Symmetric Echo Planar Imaging Framework for Clinical Translation of Rapid Dynamic Hyperpolarized ^{13}C Imaging, Magn. Reson. Med. (2016) 1–7. doi:10.1002/mrm.26123.

[66] E. Milshteyn, C. Von Morze, G.D. Reed, H. Shang, P.J. Shin, Z. Zhu, H. Chen, R. Bok, A. Goga, J. Kurhanewicz, P.E.Z. Larson, D.B. Vigneron, Development of high resolution 3D hyperpolarized carbon-13 MR molecular imaging techniques, Magn. Reson. Imaging. 38 (2017) 152–162. doi:10.1016/j.mri.2017.01.003.

[67] D.M. Wilson, J. Kurhanewicz, Hyperpolarized ^{13}C MR for Molecular Imaging of Prostate Cancer, J. Nucl. Med. 55 (2014) 1567–1572. doi:10.2967/jnumed.114.141705.

[68] P.E.Z. Larson, R. Bok, A.B. Kerr, M. Lustig, S. Hu, A.P. Chen, S.J. Nelson, J.M. Pauly, J. Kurhanewicz, D.B. Vigneron, Investigation of tumor hyperpolarized [1-^{13}C]-pyruvate dynamics using time-resolved multiband RF excitation echo-planar MRSI, Magn. Reson. Med. 63 (2010) 582–591. doi:10.1002/mrm.22264.

[69] A.Z. Lau, A.P. Chen, N.R. Ghugre, V. Ramanan, W.W. Lam, K.A. Connelly, G.A. Wright, C.H. Cunningham, Rapid multislice imaging of hyperpolarized ^{13}C pyruvate and bicarbonate in the heart, Magn. Reson. Med. 64 (2010) 1323–1331. doi:10.1002/mrm.22525.

[70] C.H. Cunningham, A.P. Chen, M. Lustig, B.A. Hargreaves, J. Lupo, D. Xu, J. Kurhanewicz, R.E. Hurd, J.M. Pauly, S.J. Nelson, D.B. Vigneron, Pulse sequence for dynamic volumetric imaging of hyperpolarized metabolic products, J. Magn.

Reson. 193 (2008) 139–146. doi:10.1016/j.jmr.2008.03.012.

[71] G.D. Reed, P.E.Z. Larson, C. Von Morze, R. Bok, M. Lustig, A.B. Kerr, J.M. Pauly, J. Kurhanewicz, D.B. Vigneron, A method for simultaneous echo planar imaging of hyperpolarized ^{13}C pyruvate and ^{13}C lactate., J. Magn. Reson. 217 (2012) 41–7. doi:10.1016/j.jmr.2012.02.008.

[72] J.J. Miller, A.Z. Lau, I. Teh, J.E. Schneider, P. Kinchesh, S. Smart, V. Ball, N.R. Sibson, D.J. Tyler, Robust and high resolution hyperpolarized metabolic imaging of the rat heart at 7 T with 3D spectral-spatial EPI, Magn. Reson. Med. (2015). doi:10.1002/mrm.25730.

[73] W. Jiang, M. Lustig, P.E.Z. Larson, Concentric rings K-space trajectory for hyperpolarized ^{13}C MR spectroscopic imaging, Magn. Reson. Med. 75 (2016) 19–31. doi:10.1002/mrm.25577.

[74] T. Çukur, Spectrally selective imaging with wideband balanced steady-state free precession MRI, Magn. Reson. Med. (2015). doi:10.1002/mrm.25700.

[75] R. Krishnamurthy, A. Pednekar, L.A. Atweh, E. Vogelius, Z.D. Chu, W. Zhang, S. Maskatia, P. Masand, S.A. Morris, R. Krishnamurthy, R. Muthupillai, Clinical validation of free breathing respiratory triggered retrospectively cardiac gated cine balanced steady-state free precession cardiovascular magnetic resonance in sedated children, J. Cardiovasc. Magn. Reson. 17 (2015) 1. doi:10.1186/s12968-014-0101-1.

[76] B. Quist, B.A. Hargreaves, B.L. Daniel, M. Saranathan, Balanced SSFP Dixon imaging with banding-artifact reduction at 3 Tesla, Magn. Reson. Med. 74 (2015) 706–715. doi:10.1002/mrm.25449.

[77] S. Månsson, J.S. Petersson, K. Scheffler, Fast metabolite mapping in the pig heart after injection of hyperpolarized ^{13}C-pyruvate with low-flip angle balanced steady-state free precession imaging, Magn. Reson. Med. 68 (2012) 1894–1899. doi:10.1002/mrm.24183.

[78] C. Von Morze, S. Sukumar, G.D. Reed, P.E.Z. Larson, R.A. Bok, J. Kurhanewicz, D.B. Vigneron, Frequency-specific SSFP for hyperpolarized ^{13}C metabolic imaging at 14.1 T, Magn. Reson. Imaging. 31 (2013) 163–170. doi:10.1016/j.mri.2012.06.037.

[79] J. Leupold, S. Månsson, J. Stefan Petersson, J. Hennig, O. Wieben, Fast multiecho balanced SSFP metabolite mapping of ^{1}H and hyperpolarized ^{13}C compounds, Magn. Reson. Mater. Physics, Biol. Med. 22 (2009) 251–256. doi:10.1007/s10334-009-0169-z.

[80] P. Bhattacharya, K. Harris, A. Lin, M. Mansson, V. Norton, W. Perman, D. Weitekamp, B. Ross, Ultra-fast three dimensional imaging of hyperpolarized ^{13}C in vivo, MAGMA. 18 (2005) 245–256.

[81] C. Laustsen, J.A. Ostergaard, M.H. Lauritzen, R. Norregaard, S. Bowen, L.V. Sogaard, A. Flyvbjerg, M. Pedersen, J.H. Ardenkjaer-Larsen, Assessment of early diabetic renal changes with hyperpolarized [1-^{13}C]pyruvate, Diabetes. Metab. Res. Rev. 29 (2013) 125–129. doi:10.1002/dmrr.

[82] O.J. Rider, D.J. Tyler, Clinical implications of cardiac hyperpolarized magnetic resonance imaging., J. Cardiovasc. Magn. Reson. 15 (2013) 93. doi:10.1186/1532-429X-15-93.

[83] H.A. Coller, Is cancer a metabolic disease?, Am. J. Pathol. 184 (2014) 4–17.

doi:10.1016/j.ajpath.2013.07.035.

[84] K.R. Keshari, R. Sriram, M. Van Criekinge, D.M. Wilson, Z.J. Wang, D.B. Vigneron, D.M. Peehl, J. Kurhanewicz, Metabolic reprogramming and validation of hyperpolarized ^{13}C lactate as a prostate cancer biomarker using a human prostate tissue slice culture bioreactor, Prostate. 73 (2013) 1171–1181. doi:10.1002/pros.22665.

[85] C.L. Swisher, P.E.Z. Larson, K. Kruttwig, A.B. Kerr, S. Hu, R.A. Bok, A. Goga, J.M. Pauly, S.J. Nelson, J. Kurhanewicz, D.B. Vigneron, Quantitative measurement of cancer metabolism using stimulated echo hyperpolarized carbon-13 MRS, Magn. Reson. Med. 71 (2014) 1–11. doi:10.1002/mrm.24634.

[86] C.S. Ward, H.S. Venkatesh, M.M. Chaumeil, A.H. Brandes, M. VanCriekinge, H. Dafni, S. Sukumar, S.J. Nelson, D.B. Vigneron, J. Kurhanewicz, C.D. James, D. a. Haas-Kogan, S.M. Ronen, Noninvasive detection of target modulation following phosphatidylinositol 3-kinase inhibition using hyperpolarized ^{13}C magnetic resonance spectroscopy, Cancer Res. 70 (2010) 1296–1305. doi:10.1158/0008-5472.CAN-09-2251.

[87] S.E. Day, M.I. Kettunen, F.A. Gallagher, D.-E. Hu, M. Lerche, J. Wolber, K. Golman, J.H. Ardenkjaer-Larsen, K.M. Brindle, Detecting tumor response to treatment using hyperpolarized ^{13}C magnetic resonance imaging and spectroscopy., Nat Med. 13 (2007) 1382–1387. doi:10.1038/nm1650.

[88] A.Z. Lau, J.J. Miller, M.D. Robson, D.J. Tyler, Cardiac perfusion imaging using hyperpolarized ^{13}C urea using flow sensitizing gradients, Magn. Reson. Med. (2015). doi:10.1002/mrm.25713.

[89] C.J. Rose, S.J. Mills, J.P.B. O'Connor, G.A. Buonaccorsi, C. Roberts, Y. Watson, S. Cheung, S. Zhao, B. Whitcher, A. Jackson, G.J.M. Parker, Quantifying spatial heterogeneity in dynamic contrast-enhanced MRI parameter maps, Magn. Reson. Med. 62 (2009) 488–499. doi:10.1002/mrm.22003.

[90] P. Sanità, M. Capulli, A. Teti, G.P. Galatioto, C. Vicentini, P. Chiarugi, M. Bologna, A. Angelucci, Tumor-stroma metabolic relationship based on lactate shuttle can sustain prostate cancer progression., BMC Cancer. 14 (2014) 154. doi:10.1186/1471-2407-14-154.

[91] A. Chen, J. Kurhanewicz, R. Bok, D. Xu, D. Joun, V. Zhang, S.J. Nelson, R.E. Hurd, D.B. Vigneron, Feasibility of Using Hyperpolarized [1-^{13}C]Lactate as a Substrate for In Vivo Metabolic ^{13}C MRSI Studies, Magn. Reson. Imaging. 26 (2009) 721–726. doi:10.1016/j.mri.2008.01.002.Feasibility.

[92] T. Vargo-Gogola, J.M. Rosen, Modelling breast cancer: one size does not fit all, Nat. Rev. Cancer. 7 (2007) 659–672. doi:10.1038/nrc2193.

[93] M.A. Schroeder, H.J. Atherton, D.R. Ball, M. a Cole, L.C. Heather, J.L. Griffin, K. Clarke, G.K. Radda, D.J. Tyler, Real-time assessment of Krebs cycle metabolism using hyperpolarized ^{13}C magnetic resonance spectroscopy., FASEB J. 23 (2009) 2529–2538. doi:10.1096/fj.09-129171.

[94] G. McGibney, M. Smith, S. Nichols, A. Crawley, Quantitative evaluation of several partial Fourier reconstruction algorithms used in MRI., Magn. Reson. Med. 30 (1993) 51–59. doi:10.1002/mrm.1910300109.

[95] M. Volker, MRI Partial Fourier reconstruction with POCS, (2012). http://www.mathworks.com/matlabcentral/fileexchange/39350-mri-partial-fourier-

reconstruction-with-pocs.

[96] A. Rosset, L. Spadola, O. Ratib, OsiriX: An open-source software for navigating in multidimensional DICOM images, J. Digit. Imaging. 17 (2004) 205–216. doi:10.1007/s10278-004-1014-6.

[97] Y. Yen, P. Le Roux, R. Bok, J. Tropp, A. Chen, V. Zhang, M. Zierhut, M. Albers, I. Park, S. Nelson, D. Vigneron, J. Kurhanewicz, Apparent T_2 of ^{13}C-labeled Metabolites In Vivo, in: Proc. 16th Annu. Meet. ISMRM, Toronto, Canada, 2008: p. 1747.

[98] E. Chiavazza, E. Kubala, C. V. Gringeri, S. Düwel, M. Durst, R.F. Schulte, M.I. Menzel, Earth's magnetic field enabled scalar coupling relaxation of ^{13}C nuclei bound to fast-relaxing quadrupolar ^{14}N in amide groups, J. Magn. Reson. 227 (2013) 35–38. doi:10.1016/j.jmr.2012.11.016.

[99] A.G. Palmer III, Relaxation and dynamic processes, in: Protein NMR Spectrosc. Princ. Pract., Academic Press, 1996.

[100] A.P. Halestrap, M.C. Wilson, The monocarboxylate transporter family-Role and regulation, IUBMB Life. 64 (2012) 109–119. doi:10.1002/iub.572.

[101] C. Juel, A.P. Halestrap, Lactate transport in skeletal muscle - role and regulation of the monocarboxylate transporter, J. Physiol. 517 (Pt 3 (1999) 633–642. doi:10.1177/088307389901400801.

[102] A.P. Halestrap, Monocarboxylic Acid Transport, Compr. Physiol. 3 (2013) 1611–1643. doi:10.1002/cphy.c130008.

[103] S. Klahr, L.J. Mandel, N. Carolina, Renal metabolism : integrated responses, in: Handb. Physiol. Ren. Physiol., Oxford University Press, 1992: pp. 2263–2333.

[104] U. Malmqvist, A. Arner, B. Uvelius, Lactate dehydrogenase activity and isoform distribution in normal and hypertrophic smooth muscle tissue from the rat, Pflugers Arch. Eur. J. Physiol. 419 (1991) 230–234. doi:10.1007/BF00371100.

[105] K.R. Keshari, D.M. Wilson, Chemistry and biochemistry of ^{13}C hyperpolarized magnetic resonance using dynamic nuclear polarization, Chem Soc. Rev. 43 (2014) 1627–1659. doi:10.1039/c3cs60124b.

[106] R.R. Rizi, A new direction for polarized carbon-13 MRI, Proc. Natl. Acad. Sci. U. S. A. 106 (2009) 5453–5454.

[107] M.N. Levy, Uptake of lactate and pyruvate by intact kidney of the dog., Am. J. Physiol. 202 (1962) 302–308.

[108] L.K. Boyd, X. Mao, Y.-J. Lu, The complexity of prostate cancer: genomic alterations and heterogeneity., Nat. Rev. Urol. 9 (2012) 652–64. doi:10.1038/nrurol.2012.185.

[109] M.I. Kettunen, D. Hu, T.H. Witney, R. Mclaughlin, F.A. Gallagher, S.E. Bohndiek, S.E. Day, K.M. Brindle, Magnetization Transfer Measurements of Exchange Between Hyperpolarized [1-^{13}C]Pyruvate and [1-^{13}C]Lactate in a Murine Lymphoma, Magn. Reson. Med. 63 (2010) 872–880. doi:10.1002/mrm.22276.

[110] Y.-F. Yen, S. Josan, L. Senadheera, J.M. Park, A. Takahashi, T. Jang, M. Merchant, P. Balchandani, J. Tropp, D. Mayer, L. Recht, L. Xing, D. Spielman, R. Hurd, P. Le Roux, Non-CPMG Echo-Train Sequence for T_2 Mapping and Large SNR Gain in Hyperpolarized ^{13}C Imaging, in: Proc. 20th Annu. Meet. ISMRM, Melbourne, Aust., 2012: p. 4295.

[111] P.J. Hoskin, D.M. Carnell, N.J. Taylor, R.E. Smith, J.J. Stirling, F.M. Daley, M.I.

Saunders, S.M. Bentzen, D.J. Collins, J. a. d'Arcy, A.P. Padhani, Hypoxia in Prostate Cancer: Correlation of BOLD-MRI With Pimonidazole Immunohistochemistry-Initial Observations, Int. J. Radiat. Oncol. Biol. Phys. 68 (2007) 1065–1071. doi:10.1016/j.ijrobp.2007.01.018.

[112] U.E. Martinez-Outschoorn, R.G. Pestell, A. Howell, M.L. Tykocinski, F. Nagajyothi, F.S. Machado, H.B. Tanowitz, F. Sotgia, M.P. Lisanti, Energy transfer in "parasitic" cancer metabolism: Mitochondria are the powerhouse and Achilles' heel of tumor cells, Cell Cycle. 10 (2011) 4208–4216. doi:10.4161/cc.10.24.18487.

[113] S. Josan, J.M. Park, R. Hurd, Y.F. Yen, A. Pfefferbaum, D. Spielman, D. Mayer, In vivo investigation of cardiac metabolism in the rat using MRS of hyperpolarized [1-^{13}C] and [2-^{13}C]pyruvate, NMR Biomed. 26 (2013) 1680–1687. doi:10.1002/nbm.3003.

[114] S. Josan, R. Hurd, J.M. Park, Y.F. Yen, R. Watkins, A. Pfefferbaum, D. Spielman, D. Mayer, Dynamic metabolic imaging of hyperpolarized [2-^{13}C]pyruvate using spiral chemical shift imaging with alternating spectral band excitation, Magn. Reson. Med. 71 (2014) 2051–2058. doi:10.1002/mrm.24871.

[115] S. Hu, H.A.I. Yoshihara, R. Bok, J. Zhou, M. Zhu, J. Kurhanewicz, D.B. Vigneron, Use of hyperpolarized [1-^{13}C]pyruvate and [2-^{13}C]pyruvate to probe the effects of the anticancer agent dichloroacetate on mitochondrial metabolism in vivo in the normal rat, Magn. Reson. Imaging. 30 (2012) 1367–1372. doi:10.1016/j.mri.2012.05.012.

[116] A.K. Grant, E. Vinogradov, X. Wang, R.E. Lenkinski, D.C. Alsop, Perfusion

imaging with a freely diffusible hyperpolarized contrast agent, Magn. Reson. Med. 66 (2011) 746–755. doi:10.1002/mrm.22860.

[117] J. Weinreb, J. Barentsz, P. Choyke, F. Cornud, M. Haider, K. Macura, D. Margolis, M. Schnall, F. Shtern, C. Tempany, H. Thoeny, S. Verma, PI-RADS v2 Prostate Imaging and Reporting and Data System: Version 2, Eur. Urol. 69 (2015) 16–40. doi:10.1016/j.eururo.2015.08.052.

[118] J.J. Fütterer, J.O. Barentsz, 3T MRI of prostate cancer, Appl. Radiol. (2009) 25–32.

[119] L. Li, L. Wang, Z. Feng, Z. Hu, G. Wang, X. Yuan, H. Wang, D. Hu, Prostate cancer magnetic resonance imaging (MRI): multidisciplinary standpoint., Quant. Imaging Med. Surg. 3 (2013) 100–12. doi:10.3978/j.issn.2223-4292.2013.03.03.

[120] A.B. Rosenkrantz, J. Neil, X. Kong, J. Melamed, J.S. Babb, S.S. Taneja, B. Taouli, Prostate Cancer: Comparison of 3D T_2-Weighted With Conventional 2D T_2-Weighted Imaging for Image Quality and Tumor Detection, Am. J. Roentgenol. 194 (2010) 446–452. doi:10.2214/AJR.09.3217.

[121] L.B. Bertelsen, P.M. Nielsen, H. Qi, T.S. Nørlinger, X. Zhang, H. Stødkilde-jørgensen, C. Laustsen, Diabetes Induced Renal Urea Transport Alterations Assessed with 3D hyperpolarized ^{13}C,^{15}N-Urea, Magn. Reson. Med. (2016). doi:10.1002/mrm.26256.

[122] H. Shang, P.E.Z. Larson, G. Reed, E. Milshteyn, C. Von Morze, F. Ong, J.W. Gordon, J.I. Tamir, B. Daniel, Variable Flip Angle Design for Balanced SSFP Transient State Imaging to Improve HP ^{13}C MRI, in: Proc. Intl. Soc. Mag. Reson. Med. 23 3768., n.d.

[123] K. Golman, J.S. Petersson, Metabolic Imaging and Other Applications of Hyperpolarized $^{13}C^{1}$, Acad. Radiol. 13 (2006) 932–942. doi:10.1016/j.acra.2006.06.001.

[124] L. Feng, R. Otazo, H. Jung, J.H. Jensen, J.C. Ye, D.K. Sodickson, D. Kim, Accelerated Cardiac T_2 Mapping using Breath-hold Multiecho Fast Spin-Echo Pulse Sequence with k-t FOCUSS, Magn. Reson. Med. 65 (2011) 1661–1669. doi:10.1002/mrm.22756.

[125] H. Jung, J.C. Ye, E.Y. Kim, Improved k–t BLAST and k– t SENSE using FOCUSS, Phys. Med. Biol. 52 (2007) 3201–3226. doi:10.1088/0031-9155/52/11/018.

[126] M. Sarma, P. Hu, S. Rapacchi, D. Ennis, A. Thomas, P. Lee, P. Kupelian, K. Sheng, Accelerating dynamic magnetic resonance imaging (MRI) for lung tumor tracking based on low-rank decomposition in the spatial-temporal domain: A feasibility study based on simulation and preliminary prospective undersampled MRI, Int. J. Radiat. Oncol. Biol. Phys. 88 (2014) 723–731. doi:10.1016/j.ijrobp.2013.11.217.

[127] S. Hu, M. Lustig, A. Balakrishnan, P.E.Z. Larson, R. Bok, S.J. Nelson, A. Goga, J.M. Pauly, B. Daniel, 3D Compressed Sensing for Highly Accelerated Hyperpolarized ^{13}C MRSI with In Vivo Applications to Transgenic Mouse Models of Cancer, Magn. Reson. Med. 63 (2010) 312–321. doi:10.1002/mrm.22233.3D.

[128] J.W. Gordon, S.B. Fain, D.J. Niles, K.M. Johnson, Robust Single-Shot Hyperpolarized ^{13}C Spectroscopic Imaging Utilizing Incoherent k-t spiral Sampling and Low-Rank Matrix Completion, in: Proc. Intl. Soc. Mag. Reson. Med. 22 3796.,

n.d.

[129] S.J. DeVience, D. Mayer, Speeding up dynamic spiral chemical shift imaging with incoherent sampling and low-rank matrix completion, Magn. Reson. Med. 77 (2017) 951–960. doi:10.1002/mrm.26170.

[130] S.G. Lingala, Y. Hu, E. Dibella, M. Jacob, Accelerated dynamic MRI exploiting sparsity and low-rank structure: K-t SLR, IEEE Trans. Med. Imaging. 30 (2011) 1042–1054. doi:10.1109/TMI.2010.2100850.

[131] Z. Wang, A.C. Bovik, H.R. Sheikh, E.P. Simoncelli, Image quality assessment: From error visibility to structural similarity, IEEE Trans. Image Process. 13 (2004) 600–612. doi:10.1109/TIP.2003.819861.

[132] F. Ong, M. Lustig, Beyond Low Rank + Sparse: Multiscale Low Rank Matrix Decomposition, {IEEE} J. Sel. Top. Signal Process. 10 (2016) 672–687. doi:10.1109/JSTSP.2016.2545518.

[133] M. Doneva, P. Börnert, H. Eggers, C. Stehning, J. Sénégas, A. Mertins, Compressed sensing reconstruction for magnetic resonance parameter mapping, Magn. Reson. Med. 64 (2010) 1114–1120. doi:10.1002/mrm.22483.

[134] J.W. Gordon, D.J. Niles, S.B. Fain, K.M. Johnson, Joint spatial-spectral reconstruction and k-t spirals for accelerated 2D spatial/1D spectral imaging of ^{13}C dynamics, Magn. Reson. Med. 71 (2014) 1435–1445. doi:10.1002/mrm.24796.

[135] G.D. Reed, C. Von Morze, A.S. Verkman, B.L. Koelsch, M.M. Chaumeil, M. Lustig, S.M. Ronen, R.A. Bok, J.M. Sands, P.E.Z. Larson, Z.J. Wang, J. Henrik, A. Larsen, J. Kurhanewicz, D.B. Vigneron, G. Reed, Imaging Renal Urea

Handling in Rats at Millimeter Resolution Using Hyperpolarized Magnetic Resonance Relaxometry, 2 (2016) 125–137.

[136] B.J. Geraghty, J.Y.C. Lau, A.P. Chen, C.H. Cunningham, Accelerated 3D echo-planar imaging with compressed sensing for time-resolved hyperpolarized 13C studies, Magn. Reson. Med. 77 (2017) 538–546. doi:10.1002/mrm.26125.

[137] I. Park, J. Gordon, S. Nelson, J. Talbott, Developing In Vivo Perfusion Imaging Methods for Spinal Cord Using Hyperpolarized [13C]t-Butanol and [13C, 15N2]Urea, in: Proc. Intl. Soc. Mag. Reson. Med. 24 1137., n.d. doi:10.1016/j.rcl.2010.07.019.2.

[138] J.M. Park, D.M. Spielman, S. Josan, T. Jang, M. Merchant, R.E. Hurd, D. Mayer, L.D. Recht, Hyperpolarized ^{13}C-lactate to ^{13}C-bicarbonate ratio as a biomarker for monitoring the acute response of anti-vascular endothelial growth factor (anti-VEGF) treatment, NMR Biomed. 29 (2016) 650–659. doi:10.1002/nbm.3509.

[139] J.X. Wang, M.E. Merritt, D. Sherry, C.R. Malloy, A general chemical shift decomposition method for hyperpolarized ^{13}C metabolite magnetic resonance imaging, Magn. Reson. Chem. (2016) 665–673. doi:10.1002/mrc.4435.

[140] C. Von Morze, G. Reed, P. Shin, P.E.Z. Larson, S. Hu, R. Bok, D.B. Vigneron, Multi-band frequency encoding method for metabolic imaging with hyperpolarized [1-^{13}C]pyruvate., J. Magn. Reson. 211 (2011) 109–13. doi:10.1016/j.jmr.2011.04.007.

[141] P.E.Z. Larson, A.B. Kerr, C. Leon, J.M. Pauly, D.B. Vigneron, A rapid method for direct detection of metabolic conversion and magnetization exchange with application to hyperpolarized substrates, J. Magn. Reson. 225 (2012) 71–80.

doi:10.1016/j.jmr.2012.09.014.

[142] C.H. Cunningham, A.P. Chen, M.J. Albers, J. Kurhanewicz, R.E. Hurd, Y.F. Yen, J.M. Pauly, S.J. Nelson, D.B. Vigneron, Double spin-echo sequence for rapid spectroscopic imaging of hyperpolarized ^{13}C, J. Magn. Reson. 187 (2007) 357–362. doi:10.1016/j.jmr.2007.05.014.

[143] Y. Xing, G.D. Reed, J.M. Pauly, A.B. Kerr, P.E.Z. Larson, Optimal variable flip angle schemes for dynamic acquisition of exchanging hyperpolarized substrates, J. Magn. Reson. 234 (2013) 75–81. doi:10.1016/j.jmr.2013.06.003.

[144] J. Maidens, S. Member, J.W. Gordon, M. Arcak, P.E.Z. Larson, Optimizing flip angles for metabolic rate estimation in hyperpolarized carbon-13 MRI, IEEE Trans. Med. Imaging. 62 (2016) 1–10. doi:10.1109/TMI.2016.2574240.

[145] E. Milshteyn, C. Von Morze, D. Galen, H. Shang, P.J. Shin, P.E.Z. Larson, D.B. Vigneron, Using a Low Rank plus Sparse Reconstruction Approach to Accelerate 3D Dynamic bSSFP Hyperpolarized Carbon-13 MR Imaging, in: Proc. Intl. Soc. Mag. Reson. Med. 24 2329., n.d.

[146] J.C. Crane, M.P. Olson, S.J. Nelson, SIVIC : Open-Source , Standards-Based Software for DICOM MR Spectroscopy Workflows, Int. J. Biomed. Imaging. 2013 (2013).

[147] R.E. Hurd, D. Spielman, S. Josan, Y. Yen, A. Pfefferbaum, D. Mayer, Exchange-Linked Dissolution Agents in Dissolution-DNP ^{13}C Metabolic Imaging, Magn. Reson. Med. 70 (2013) 936–942. doi:10.1002/mrm.24544.

[148] N. Bahrami, C.L. Swisher, C. Von Morze, D.B. Vigneron, P.E.Z. Larson, Kinetic and perfusion modeling of hyperpolarized ^{13}C pyruvate and urea in cancer with

arbitrary RF flip angles., Quant. Imaging Med. Surg. 4 (2014) 24–32. doi:10.3978/j.issn.2223-4292.2014.02.02.

[149] H. Shang, P.E.Z. Larson, A. Kerr, G. Reed, S. Sukumar, A. Elkhaled, J.W. Gordon, M.A. Ohliger, J.M. Pauly, M. Lustig, D.B. Vigneron, Multiband RF pulses with improved performance via convex optimization, J. Magn. Reson. 262 (2016) 81–90. doi:10.1016/j.jmr.2015.11.010.

[150] B.J. Geraghty, J.Y.C. Lau, A.P. Chen, C.H. Cunningham, Accelerated 3D echo-planar imaging with compressed sensing for time-resolved hyperpolarized ^{13}C studies, Magn. Reson. Med. 77 (2017) 538–546. doi:10.1002/mrm.26125.

[151] A.J. De Langen, V.E.M. Van Den Boogaart, J.T. Marcus, M. Lubberink, Use of $H_2{}^{15}O$-PET and DCE-MRI to Measure Tumor Blood Flow, Oncologist. 13 (2008) 631–644. doi:10.1634/theoncologist.2007-0235.

[152] S.P. Sourbron, H.J. Michaely, M.F. Reiser, MRI-Measurement of Perfusion and Glomerular Filtration in the Human Kidney With a Separable Compartment Model, 43 (2008) 40–48.

[153] L. Annet, L. Hermoye, F. Peeters, Glomerular Filtration Rate : Assessment With Dynamic Contrast-Enhanced MRI and a Cortical- Compartment Model in the Rabbit Kidney, J. Magn. Reson. Imaging. 20 (2004) 843–849. doi:10.1002/jmri.20173.

[154] E.D. Morris, C.J. Endres, K.C. Schmidt, B.T. Christian, R.F. Muzic Jr., R.E. Fisher, Kinetic Modeling in Positron Emission Tomography, in: M.N. Wernick, J.N. Aarsvold (Eds.), Emiss. Tomogr. Fundam. PET SPECT, 1st ed., Academic Press, 2004: pp. 499–540. doi:10.1016/B978-012744482-6.50026-0.

Publishing Agreement

It is the policy of the University to encourage the distribution of all theses, dissertations, and manuscripts. Copies of all UCSF theses, dissertations, and manuscripts will be routed to the library via the Graduate Division. The library will make all theses, dissertations, and manuscripts accessible to the public and will preserve these to the best of their abilities, in perpetuity.

Please sign the following statement:

I hereby grant permission to the Graduate Division of the University of California, San Francisco to release copies of my thesis, dissertation, or manuscript to the Campus Library to provide access and preservation, in whole or in part, in perpetuity.

Eugene Milshteyn
Author Signature

11/20/2017
Date